

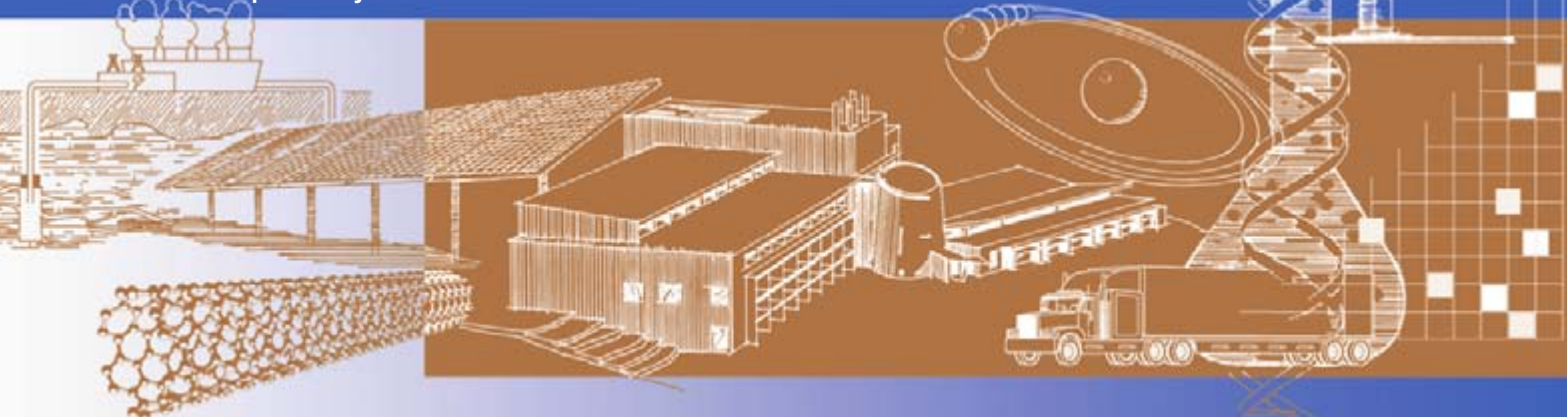
High-Efficiency Amorphous Silicon and Nanocrystalline Silicon-Based Solar Cells and Modules

**Final Technical Progress Report
30 January 2006 – 29 January 2008**

S. Guha and J. Yang
*United Solar Ovonic LLC
Troy, Michigan*

**Subcontract Report
NREL/SR-520-43191
May 2008**

NREL is operated by Midwest Research Institute • Battelle Contract No. DE-AC36-99-GO10337



High-Efficiency Amorphous Silicon and Nanocrystalline Silicon-Based Solar Cells and Modules

Final Technical Progress Report 30 January 2006 – 29 January 2008

S. Guha and J. Yang
United Solar Ovonic LLC
Troy, Michigan

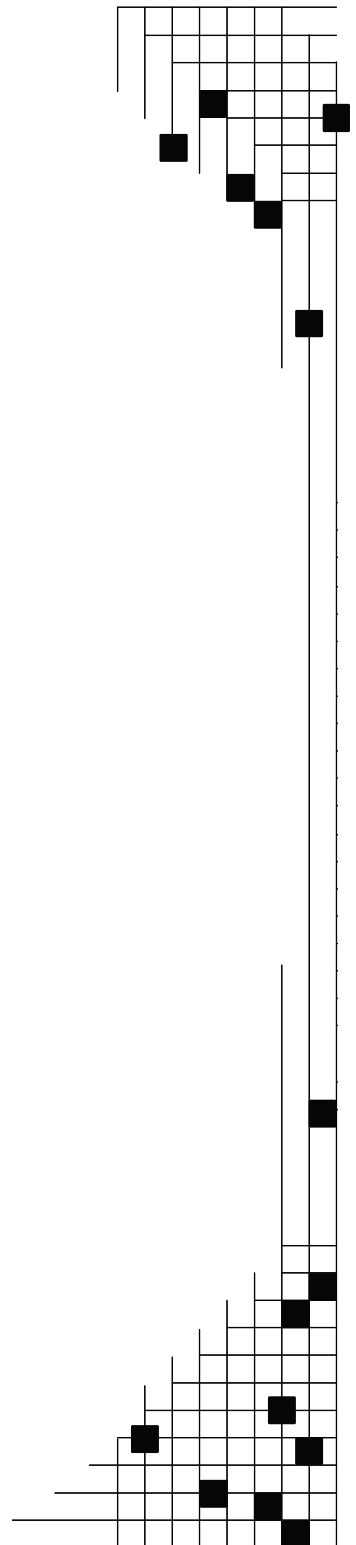
NREL Technical Monitor: Bolko von Roedern
Prepared under Subcontract No. ZXL-6-44205-14

National Renewable Energy Laboratory
1617 Cole Boulevard, Golden, Colorado 80401-3393
303-275-3000 • www.nrel.gov

Operated for the U.S. Department of Energy
Office of Energy Efficiency and Renewable Energy
by Midwest Research Institute • Battelle

Contract No. DE-AC36-99-GO10337

Subcontract Report
NREL/SR-520-43191
May 2008



**This publication was reproduced from the best available copy
Submitted by the subcontractor and received no editorial review at NREL**

NOTICE

This report was prepared as an account of work sponsored by an agency of the United States government. Neither the United States government nor any agency thereof, nor any of their employees, makes any warranty, express or implied, or assumes any legal liability or responsibility for the accuracy, completeness, or usefulness of any information, apparatus, product, or process disclosed, or represents that its use would not infringe privately owned rights. Reference herein to any specific commercial product, process, or service by trade name, trademark, manufacturer, or otherwise does not necessarily constitute or imply its endorsement, recommendation, or favoring by the United States government or any agency thereof. The views and opinions of authors expressed herein do not necessarily state or reflect those of the United States government or any agency thereof.

Available electronically at <http://www.osti.gov/bridge>

Available for a processing fee to U.S. Department of Energy
and its contractors, in paper, from:

U.S. Department of Energy
Office of Scientific and Technical Information
P.O. Box 62
Oak Ridge, TN 37831-0062
phone: 865.576.8401
fax: 865.576.5728
email: <mailto:reports@adonis.osti.gov>

Available for sale to the public, in paper, from:

U.S. Department of Commerce
National Technical Information Service
5285 Port Royal Road
Springfield, VA 22161
phone: 800.553.6847
fax: 703.605.6900
email: orders@ntis.fedworld.gov
online ordering: <http://www.ntis.gov/ordering.htm>



Printed on paper containing at least 50% wastepaper, including 20% postconsumer waste

Table of Contents

Preface	v
Executive Summary	vi
Objectives	vi
Approaches	vi
Status/Accomplishments	vii
Publications	x
1. Fundamental research on mixed-phase silicon solar cells and nc-Si:H solar cells	1
1.1. Introduction	1
1.2. Experimental details	2
1.3. Results and discussion	2
1.3.1. Microscopic local current flow in mixed-phase Si:H solar cells	2
1.3.2. Light-induced change of local current flow in mixed-phase Si:H solar cells	8
1.3.3. Doping effect on the material structure in mixed-phase Si:H solar cells	9
2. Correlation of hydrogen dilution profiling with material structure and solar cell performance	16
2. 1. Introduction	16
2. 2. Experimental details	17
2. 3. Results and discussion	17
2.3.1. Material structures	17
2.3.2. Solar cell performance	20
2. 4. Summary	21
3. Optimization of Ag/ZnO back reflector	26
3. 1. Introduction	26
3. 2. Experimental details	27
3. 3. Results and discussion	27
3.3.1. Structural analysis	27
3.3.2. a-SiGe:H solar cells on improved Ag/ZnO back reflectors	32
3.3.3. Calculation of optical enhancement in a-SiGe:H cells on Ag/ZnO back reflector	37
3. 4. Summary	39
4. High efficiency a-Si:H/a-SiGe:H/nc-Si:H and a-Si:H/nc-Si:H/nc-Si:H triple-junction solar cells	42
4. 1. Introduction	42
4. 2. Experimental details	42
4. 3. Results and discussion	42
4.3.1. a-Si:H top cell	42
4.3.2. a-SiGe:H middle cell	44
4.3.3. nc-Si:H bottom cell	45
4.3.4. Optimization of a-Si:H/a-SiGe:H/nc-Si:H Triple-junction design	56
4.3.5. High efficiency triple-junction cells	58
4. 4. Summary	59
5. High rate deposition of a-Si:H and a-SiGe:H solar cells using modified very high frequency glow discharge	62

5. 1.	Introduction	62
5. 2.	a-Si:H and a-SiGe:H single-junction solar cells made with MVHF at high deposition rates	62
5. 3.	a-Si:H/a-SiGe:H double-junction solar cells made with MVHF at high rates	69
5. 4.	Summary	69
6.	Large-area a-Si:H/a-SiGe:H/a-SiGe:H triple-junction and a-Si:H/nc-Si:H double-junction solar cells	71
6. 1.	Introduction	71
6. 2.	Experimental details	71
6. 3.	a-Si:H/a-SiGe:H/a-SiGe:H triple-junction cells under manufacturing constraints	72
6. 4.	Large-area a-Si:H/nc-Si:H double-junction modules	75
6. 5.	Summary	77
References:	77

Preface

This final report covers the work performed by United Solar Ovonic LLC for the period from January 30, 2006 to January 29, 2008, under the support of the National Renewable Energy Laboratory Thin Film Partnership Program Subcontract No. ZXL-6-44205-14. The original subcontract was for a three year period starting from January 30, 2006 to January 29, 2009. Due to realignment with the Solar America Initiative Program, the Thin Film Partnership Program was terminated on January 29, 2008. Therefore, this final report summarizes the work performed in the first two phases.

The following personnel participated in this research program:

A. Banerjee, E. Chen, S. Guha (Principal Investigator), B. Hang, M. Hopson, A. Mohsin, J. Noch, J. M. Owens, T. Palmer, L. Sivec, D. Wolf, X. Xu, B. Yan, J. Yang (Co-Principal Investigator), K. Younan, and G. Yue.

Collaboration with the Colorado School of Mines, University of Oregon, Syracuse University, and the National Renewable Energy Laboratory is acknowledged.

Executive Summary

Objectives

United Solar Ovonic LLC (United Solar) has successfully used its spectrum splitting a-Si:H/a-SiGe:H/a-SiGe:H triple-junction structure in their manufacturing plants. A manufacturing capacity of 118 MW was achieved in 2007 with plants in Auburn Hills and Greenville, Michigan. The global photovoltaic market has expanded dramatically over the last few years. United Solar has set up a very aggressive expansion plan to achieve grid parity. In order to achieve this challenging goal, we need to improve our solar panel efficiency, improve the manufacturing throughput, and reduce the manufacturing cost. In the Thin Film Partnership Program (TFPP), we have identified three areas of research:

- i) Optimize the a-Si:H and a-SiGe:H deposition parameters under the current manufacturing constraints for improving the solar module efficiency and manufacturing throughput, and reducing the manufacturing cost.
- ii) Explore new deposition methods for a-Si:H and a-SiGe:H materials to improve the a-Si:H/a-SiGe:H/a-SiGe:H triple-junction cell efficiency at high deposition rates.
- iii) Explore new materials and new cell structures for higher efficiency at high deposition rates.

The first area represents a short-term goal with the objective of improving the current manufacturing module efficiency and throughput without modification of the production machines. Therefore, certain constraints have to be considered. For example, the deposition rate of each layer has to be adjusted according to the web speed and chamber length. Under this premise, any improvement in the cell efficiency will improve the current manufacturing module efficiency and throughput. The second area represents an intermediate-term goal with the objective of considerably improving cell and module efficiency with a higher throughput but with only limited modifications of the manufacturing machines. The third area represents a long-term goal with the objective of significantly improving the module efficiency with high throughput by using new designs for the manufacturing machines in order to deposit the new materials.

In order to achieve the goals in each area, the research in material properties and device designs are very important, especially on the material structure and defect characterization. Under the TFPP team, we have made a significant amount of fundamental studies and gained remarkable knowledge in material deposition, material characterization, and device optimization. Although the TFPP was terminated due to the realignment with the Solar America Initiative (SAI) Project, the achievements in this project have built a solid foundation, which will help achieving the goals and milestones in the SAI project.

Approaches

For the first area, we carried out the research using a two-step approach. We first optimized the a-Si:H and a-SiGe:H component cells as well as the a-Si:H/a-SiGe:H/a-SiGe:H triple-junction cells using one of our large-area batch RF glow discharge machines. The a-

Si:H/a-SiGe:H/a-SiGe:H triple-junction cells were deposited on Al/ZnO back reflectors made in the manufacturing machines. When experimental deposition parameters are improved, the new recipe would be transferred to the production line.

For the second area, we studied high rate a-Si:H and a-SiGe:H solar cells made with MVHF. Although the MVHF a-Si:H top cell has shown a significant advantage over the RF deposited a-Si:H cells at high rates, many challenges still remain, especially in the quality of high rate deposited a-SiGe:H middle and bottom cells. Under this program, we explored more deposition parameters and researched new deposition regimes.

For the third area, we continued investigating issues related to nc-Si:H material properties, cell efficiency, and deposition rate. The major target is to demonstrate the feasibility of using nc-Si:H in multi-junction structures and to achieve higher cell and module efficiencies than those obtained using the conventional a-Si:H/a-SiGe:H/a-SiGe:H triple-junction structure. We have identified that the nanocrystalline evolution along the growth direction is one of the major challenges for high efficiency nc-Si:H solar cells. Therefore, we developed a hydrogen dilution profiling technique for controlling the nanocrystalline evolution during nc-Si:H deposition. We have further optimized hydrogen dilution for high rate nc-Si:H deposition. At the same time, we modified the MVHF deposition chamber and made it suitable for high-pressure deposition. In addition, we optimized the a-Si:H top cell and a-SiGe:H middle cell for high efficiency a-Si:H/a-SiGe:H/nc-Si:H triple-junction structures.

Another major issue for using nc-Si:H solar cells in a production line is the thickness of the absorber layer and its uniformity. Due to the decrease of electromagnetic wavelength with the increase of VHF frequency, the electric field distribution over a large-area cathode becomes non-uniform. A special design for the large-area VHF cathodes is required to achieve uniform deposition. We have worked on the large-area VHF cathode design for the nc-Si:H deposition.

Parallel to optimizing the solar cell efficiency, we have carried out significant fundamental studies on material structures and device designs. Fundamental research was done through collaboration with NREL, University of Oregon, Colorado School of Mines, and Syracuse University. We investigated a-Si:H, a-SiGe:H, and nc-Si:H material properties and the mechanism of light-induced degradation in these materials and solar cells. Most results have been reported by our collaborators. In addition, we have worked on the improvement of the light trapping scheme in a-SiGe:H and nc-Si:H solar cells by optimizing the texture of Ag/ZnO back reflectors. The correlation of Ag and ZnO structure with solar cell performance has been studied and provides a guideline for making good back reflectors.

Status/Accomplishments

Fundamental research in mixed-phase silicon solar cells and nc-Si:H solar cells

1. We have studied the material structures of mixed-phase silicon materials with TEM, AFM, and C-AFM. We correlated the materials structure with the light induced degradation of solar cells. The aggregation of nanograins forms micrometer sized clusters observed from the top view by AFM, and cone structures from the side view by X-TEM. The nanocrystalline aggregation supports the previously proposed two-diode

model for the light induced degradation in mixed-phase solar cells. In addition, the reduction of current density in the crystalline phase during light soaking provided a direct support of the explanation.

2. We studied the doping effect on the structure changes in the mixed-phase materials. We found that first the incorporation of P in mixed-phase silicon materials resulted in a higher hydrogen dilution ratio to reach the amorphous/nanocrystalline transition and second the nanocrystalline aggregation disappeared when P was incorporated into the mixed-phase materials.
3. For the collaboration with NREL, we have studied material structures of nc-Si:H solar cells with various hydrogen dilution profiles. The TEM and AFM analyses showed that with an optimized hydrogen profiling, we can control the growth of nc-Si:H with no incubation layer, and uniform distribution of crystallinity along the growth direction. We correlated the material structure properties to the nc-Si:H solar cell performance.

Optimization of solar cell performance at the amorphous/nanocrystalline transition regime

1. We have optimized a-Si:H solar cells at the amorphous/nanocrystalline transition regime. We found that when a-Si:H solar cells were made under a hydrogen dilution condition close to the transition regime, the cell performance was improved. In order to keep the material structure close to the transition regime throughout the intrinsic layer, hydrogen dilution profiling was proven to be a useful method.
2. The same approach was also used to optimize the a-SiGe:H component cells for high efficiency triple-junction solar cells.

Optimization of optical enhancement by back reflectors

1. We have developed an analysis method of optical enhancement in a-SiGe:H and nc-Si:H solar cells. We found that the optical enhancement with optimized Ag/ZnO back reflectors was as high as 20-30 folds at long wavelength. Although optical enhancement is already very large, it is still not as large as the theoretical value of $4n^2$ (n is the optical index of the semiconductor layers) and more improvement is expected by optimizing the Ag and ZnO layers.
2. We have studied the correlation of Ag/ZnO structures and solar cell performance. We found that a flat Ag layer reduced the plasmon absorption but it also reduced the scattering at the Ag/ZnO interface. For back reflectors with thinner ZnO, a textured Ag is better than flat Ag layer. However, when the ZnO layer is thick enough, a flat Ag layer is better than a textured Ag layer.

High efficiency a-Si:H, a-SiGe:H, and nc-Si:H multi-junction solar cells

1. We studied the optimization of multi-junction solar cell designs. The current mismatch for high efficiency multi-junction solar cells was systematically studied. We found that a current mismatch with nc-Si:H bottom cell limited current yields improved initial and stable efficiencies for a-Si:H/a-SiGe:H/nc-Si:H triple-junction solar cells.

2. We have achieved active-area (0.25 cm^2) initial and stable efficiencies of 15.4% and 13.0%, respectively, for an a-Si:H/a-SiGe:H/nc-Si:H triple-junction cell, where the top and middle cells were made using RF at a low rate $\sim 1 \text{ Å/s}$, and the nc-Si:H bottom cell using MVHF at a high rate $\sim 5\text{-}8 \text{ Å/s}$.
3. We have achieved active-area (0.25 cm^2) initial and stable efficiencies of 14.1% and 13.3%, respectively, for an a-Si:H/nc-Si:H/nc-Si:H triple-junction cell, where the top cell was made using RF at a low rate $\sim 1 \text{ Å/s}$, and the nc-Si:H middle and bottom cells using MVHF at a high rate $\sim 5\text{-}8 \text{ Å/s}$.

High rate deposition of a-Si:H, a-SiGe:H, and a-Si:H/a-SiGe:H double-junction solar cells

1. We have investigated deposition parameters for a-Si:H and a-SiGe:H deposition with MVHF at high rates. We found that the performance and stability of a-Si:H single-junction cells deposited with MVHF do not depend on the deposition rate in the range of $1\text{-}15 \text{ Å/s}$.
2. We have achieved active-area (0.25 cm^2) initial and stable efficiencies of 9.2% and 8.5%, respectively, for nc-Si:H single-junction cells made with MVHF at a high rate $\sim 5\text{-}8 \text{ Å/s}$.
3. We have made a-Si:H/a-SiGe:H double-junction solar cells on Ag/ZnO back reflectors using MVHF. The a-Si:H and a-SiGe:H intrinsic layers were deposited in 4 minutes and 4 minutes, respectively. An initial active-area efficiency of 11.7% has been achieved.

Large area a-Si:H/a-SiGe:H/a-SiGe:H triple-junction and a-Si:H/nc-Si:H double-junction solar cells

1. We have achieved an aperture-area (416 cm^2) stable efficiency of 8.6% on an a-Si:H/a-SiGe:H/a-SiGe:H triple-junction solar cell deposited under the manufacturing constraints on an Al/ZnO back reflector made in the manufacturing line. The cell was encapsulated using a procedure similar to the manufacturing process.
2. We have achieved an aperture-area (460 cm^2) initial efficiency of 11.7% on an a-Si:H/nc-Si:H double-junction solar cell deposited on Ag/ZnO back reflectors with RF glow discharge at a high rate. The nc-Si:H intrinsic layer in the bottom cell was deposited within 50 minutes.

Publications

1. G. Yue, B. Yan, G. Ganguly, J. Yang, S. Guha, and C. Teplin, "Material Structure and Metastability of Hydrogenated Nanocrystalline Silicon Solar Cells," *Appl. Phys. Lett.* **88**, 263507 (2006).
2. G. Yue, B. Yan, G. Ganguly, J. Yang, and S. Guha, "Metastability of Hydrogenated Nanocrystalline Silicon Solar Cells," *Mater. Res. Soc. Symp. Proc.* **910**, 29 (2006). (Invited).
3. B. Yan, J. Yang, and S. Guha, "Temperature Dependence of Dark Current-Voltage Characteristics of Hydrogenated Amorphous and Nanocrystalline Silicon Based Solar Cells," *Mater. Res. Soc. Symp. Proc.* **910**, 713 (2006).
4. B. Yan, C.-S. Jiang, H. R. Moutinho, M. M. Al-Jassim, J. Yang, and S. Guha, "Local Current Flow in Mixed-Phase Silicon Solar Cells and Correlation to Light-Induced Open-Circuit Voltage Enhancement," *Mater. Res. Soc. Symp. Proc.* **910**, 647 (2006).
5. P. G. Hugger, S. Datta, P.T. Erslev, G. Yue, G. Ganguly, B. Yan, J. Yang, S. Guha, and J.D. Cohen, "Electronic Characterization and Light-Induced Degradation in nc-Si:H Solar Cells," *Mater. Res. Soc. Symp. Proc.* **910**, 21 (2006).
6. D. C. Bobela, T. Su, P. C. Taylor, A. Madan, and G. Ganguly, "The Concentration of $(\text{SiH}_2)_n$ Sites in Low and High Defect Density a-Si:H," *Mater. Res. Soc. Symp. Proc.* **910**, 251 (2006).
7. N. H. Nickel, M. Weizman, I. Sieber, and B. Yan, "Influence of Compositional and Structural Changes on Hydrogen Bonding in Silicon and Silicon-Germanium Alloys," *J. Non-Cryst. Solids* **352**, 1037 (2006).
8. D. C. Bobela, T. Su, P. C. Taylor, and G. Ganguly, "Microscopic Properties of Silicon Dihydride Bonding in a-Si:H," *J. Non-Cryst. Solids* **352**, 1041 (2006).
9. M. Weizman, N. H. Nickel, I. Sieber, and B. Yan, "Successive Segregation in Laser-Crystallized Poly-SiGe Thin Films," *J. Non-Cryst. Solids* **352**, 1259 (2006).
10. S. Guha and J. Yang, "Progress in Amorphous and Nanocrystalline Silicon Solar Cells," *J. of Non-Crystalline Solids* **352**, 1917 (2006).
11. B. Yan, G. Yue, J.M. Owens, J. Yang, and S. Guha, "Over 15% Efficient Hydrogenated Amorphous Silicon Based Triple-Junction Solar Cells Incorporating Nanocrystalline Silicon", *Conf. Record of the 2006 IEEE 4th World Conf. on Photovoltaic Energy Conversion*, (Hawaii, USA, May 7-12, 2006), p. 1477.
12. C.-S. Jiang, H. R. Moutinho, M. M. Al-Jassim, L. L. Kazmerski, B. Yan, J. M. Owens, J. Yang, and S. Guha, "Distribution of Local Open-Circuit Voltage on Amorphous and Nanocrystalline Mixed-Phase Si:H and SiGe:H Solar Cells," *Conf. Record of the 2006 IEEE 4th World Conf. on Photovoltaic Energy Conversion*, (Hawaii, USA, May 7-12, 2006), p. 1552.
13. G. Yue, B. Yan, G. Ganguly, J. Yang, S. Guha, C. Teplin, and D. L. Williamson, "Performance Improvement of Hydrogenated Nanocrystalline Silicon Solar Cells by

- Hydrogen Dilution Profiling,” Conf. Record of the 2006 IEEE 4th World Conf. on Photovoltaic Energy Conversion, (Hawaii, USA, May 7-12, 2006), p. 1588.
14. G. Ganguly, G. Yue, B. Yan, J. Yang, and S. Guha, “Fabrication of Large Area Amorphous Silicon/Nanocrystalline Silicon Double Junction Solar Cells,” Conf. Record of the 2006 IEEE 4th World Conf. on Photovoltaic Energy Conversion, (Hawaii, USA, May 7-12, 2006), p. 1712.
 15. G. Yue, B. Yan, G. Ganguly, J. Yang, and S. Guha, “Metastability in Hydrogenated Nanocrystalline Silicon Solar Cells,” J. Mater. Soc. **22**, 1128 (2007).
 16. B. Yan, C.-S. Jiang, C. W. Teplin, H. R. Moutinho, M. M. Al-Jassim, J. Yang, and S. Guha “Local Current Flow in Amorphous and Nanocrystalline Mixed-Phase Silicon Solar Cells”, J. Appl. Phys. **101**, 033711 (2007).
 17. C.-S. Jiang, B. Yan, H. R. Moutinho, M. M. Al-Jassim¹, J. Yang, and S. Guha, “Light Soaking and Thermal Annealing Effects on the Micro-Electrical Properties of Amorphous and Nanocrystalline Mixed-Phase Silicon Solar Cells,” Mater. Res. Soc. Symp. Proc. **989**, 15 (2007).
 18. B. Yan, G. Yue, and S. Guha, “Status of nc-Si:H Solar Cells at United Solar and Roadmap for Manufacturing a-Si:H and nc-Si:H Based Solar Panels,” Mater. Res. Soc. Symp. Proc. **989**, 335 (2007). (Invited).
 19. G. Yue, B. Yan, J. Yang, and S. Guha, “High Rate Deposition of Amorphous Silicon Based Solar Cells using Modified Very High Frequency Glow Discharge” Mater. Res. Soc. Symp. Proc. **989**, 359 (2007).
 20. G. Yue, B. Yan, C. W. Teplin, J. Yang, and S. Guha, “Optimization and Characterization of *i/p* Buffer Layer in Hydrogenated Nanocrystalline Silicon Solar Cells”, J. Non-Crystal Solids, (2008), in press.
 21. C.-S. Jiang, B. Yan, Y. Yan, C.W. Teplin, R. Reedy, H.R. Moutinho, M.M. Al-Jassim, J. Yang, and S. Guha “Effect of P Incorporation on Aggregation of Nanocrystallites in Amorphous and Nanocrystalline Mixed-Phase Silicon Thin Films”, J. Non-Crystal Solids, (2008), in press.
 22. A.H. Mahan, Y. Xu, H.M. Branz, and B. Yan, “Amorphous Silicon Germanium n-i-p Solar Cells Deposited by HWCVD Using a Tantalum Filament Operated at 1800°C”, J. Non-Crystal Solids, (2008), in press.
 23. P. G. Hugger, D. Cohen, G. Yue, B. Yan, J. Yang, and S. Guha, “Effects of Light-Induced Degradation and Hydrogen Profiling on the Electronic Properties of Nanocrystalline Silicon and Their Influence on Solar Cell Performance”, J. Non-Crystal Solids, (2008), in press.
 24. C.-S. Jiang, B. Yan, Y. Yan, C.W. Teplin, R. Reedy, H.R. Moutinho, M.M. Al-Jassim, and J. Yang, “P-Induced nanocrystallite dispersion in amorphous-nanocrystalline mixed-phase Si:H thin films”, J. Appl. Phys. (2008), in press.

1. Fundamental research on mixed-phase silicon solar cells and nc-Si:H solar cells

1.1. Introduction

Hydrogenated amorphous silicon (a-Si:H) and nanocrystalline silicon (nc-Si:H) thin films have attracted a great deal of interest in photovoltaic devices and large-area thin-film electronics. One of the main fabrication techniques is radio frequency (RF) or very high frequency (VHF) glow discharge, which decomposes SiH_4 or Si_2H_6 molecules in the plasma. Hydrogen dilution is a critical parameter for controlling the material structure. By varying the hydrogen dilution in the process gases, one can obtain conventional a-Si:H, a-Si:H with intermediate orders (or so-called protocrystalline Si:H), mixed-phase Si:H, and nc-Si:H with high crystallinity [1]. Three models have been proposed to explain the role of hydrogen during the film growth: etching amorphous phase by atomic hydrogen, H-mediated chemical annealing, and enhanced surface diffusion of Si radicals [2]. Many recent studies have analyzed nanocrystalline formation using *in-situ* characterizations, such as real time spectroscopic ellipsometry [3,4] and infrared attenuated total reflection [5]. Most results support the surface diffusion model, which suggests that the diffusion of Si radicals is increased on the growth surface with the presence of additional hydrogen on the growth surface [2]. The material structural properties and their correlations to the deposition conditions have also been widely studied using many *ex-situ* characterization techniques such as cross-sectional transmission electron microscopy (X-TEM) [6,7] atomic force microscopy (AFM) and conductive AFM (C-AFM) [8,9], and scanning Kelvin probe microscopy (SKPM) [10]. The general picture revealed from these characterizations is that under a constant hydrogen dilution over a given threshold, nanocrystalline nucleation appears after an amorphous incubation layer. We also found that cone-shaped Si nanocrystallites grow with the film thickness. When the hydrogen dilution is just above the threshold, individual and isolated nanocrystalline cones form in a large fraction of amorphous matrix. This kind of material is normally called mixed-phase material. When the hydrogen dilution is high enough, the nanocrystalline cones coalesce and fully nc-Si:H materials are obtained. Raman, X-TEM, and X-Ray diffraction measurements show that the grain size is in a few nm to tens of nm range, while the sizes of nanocrystalline cones can be as large as micrometer range. Therefore, a structural model consisting of nanometer-size grains in micrometer-size cones separated by amorphous tissue has been proposed [11]. This model explains most of the materials properties including the increase of crystalline volume fraction with film thickness.

Among the three types of material structures, the mixed-phase material contains very rich physics for fundamental study and device optimization. Although the mixed-phase material is very difficult to use in real solar cell application, the optimized a-Si:H and nc-Si:H solar cells are made close to the mixed-phase regime [12,13]. In general, the mixed-phase solar cells show an open-circuit voltage (V_{oc}) ranging from 0.5 to 1.0 V, which is between the V_{oc} values of typical a-Si:H and nc-Si:H cells. One interesting phenomenon for the mixed-phase solar cells is that the V_{oc} increases after light soaking [14,15], opposite to commonly observed for a-Si:H and nc-Si:H solar cells where the V_{oc} decreases after light soaking due to the Staebler-Wronski effect [16]. The original explanation for the light-induced V_{oc} increase in the mixed-phase solar cell was based on light-induced structural changes from the crystalline phase to amorphous phase [14, 15]. Subsequently, a complementary model of two parallel-connected diodes (two-diode model) was proposed [17]. There are two key points made in the two-diode model. First, the

amorphous phase and nanocrystalline phase can be considered as two separate diodes with significantly different characteristics. Second, the current versus voltage (I-V) characteristics of nc-Si:H diode in the mixed-phase cells degrade by light soaking. The degradation of nc-Si:H causes a decrease in the electric current, when a forward voltage larger than the V_{oc} of the nc-Si:H cell is applied, resulting in an increase in the V_{oc} of the mixed-phase solar cells [17]. However, the size of the nanocrystallites observed by X-ray diffraction and Raman spectroscopy is very small, ranging from a few nm to 30 nm. It is difficult to believe that such small grains can form complete diodes through the entire thickness of the intrinsic layer.

Under this program, we used atomic force microscopy (AFM), conductive atomic force microscopy (C-AFM), Kelvin probe microscopy (SKPM) to measure the surface structure, the local current flow [8], and local V_{oc} distribution [9] in mixed-phase Si solar cells, respectively. We also studied the structural properties along the growth direction and explored the possible growth mechanisms using X-TEM.

1.2. Experimental details

The mixed-phase Si:H materials and solar cells were made on a $4 \times 4 \text{ cm}^2$ stainless steel substrate using a multi-chamber PECVD system used for high efficiency solar cell fabrication. We controlled the deposition parameters in the regime of amorphous to nanocrystalline transition to obtain various material structures on one substrate, such as the center of the deposition showing an amorphous structure, edges with a mixed-phase signature, and the corners with a substantially nanocrystalline volume fraction as previously reported [14,15].

Secondary-ion mass spectrometry (SIMS) was used to measure the chemical composition in the films. Raman spectroscopy was used to measure the crystallinity of the films. A laser spot with a diameter of 1-2 μm and a wavelength of 532 nm was irradiated on the samples, and Raman scattering from the sample was measured by a monochromator. AFM, C-AFM and SKPM were used to measure the morphology, microscopic current distribution, and local work function distributions, respectively. X-TEM was used to investigate the structures inside the films. The X-TEM samples were prepared by the focused ion beam (FIB) technique. A 50-nm-thick Pt layer was deposited on the sample surface and an 80-nm-thick slice of the sample was cut off using the FIB. All of these characterizations were carried out at NREL.

1.3. Results and discussion

1.3.1. Microscopic local current flow in mixed-phase Si:H solar cells

In the mixed-phase regime, the cell performance is very sensitive to the deposition condition. A very small change in the plasma condition can change the cell performance dramatically. Even on a $4 \text{ cm} \times 4 \text{ cm}$ substrate, the distribution of cell performance varying from a-Si:H like to nc-Si:H like can be obtained. Therefore, by carefully selecting the deposition parameters, we can obtain solar cells on one substrate having different characteristics at different locations. Figure 1 shows the cell locations on a $4 \text{ cm} \times 4 \text{ cm}$ substrate. Figure 2 gives an example of V_{oc} distribution of the sixteen 0.25-cm^2 cells on the substrate. It is clear that the cells at the center show amorphous-like characteristics with V_{oc} around 1.0 V, mixed-phase-like

characteristic with V_{oc} between 0.7 V and 0.8 V on the edges, and nanocrystalline-like characteristic at the corners with V_{oc} between 0.5 V and 0.6 V.

To further confirm the differences in material structures, Raman spectra were acquired at the areas marked A, B, and C in Fig. 1, where the amorphous region (area A) is between cells 22 and 23, mixed-phase (area B) between cells 11 and 12, and substantially nanocrystalline (area C) between cells 51 and 11. The Raman spectra clearly show that in area A, the material has a complete amorphous structure without detectable crystalline peak; in area B, a small peak at $\sim 520\text{ cm}^{-1}$ indicates a mixed-phase nature with the crystalline peak fraction of $\sim 10\%$; and in area C, a large peak at $\sim 520\text{ cm}^{-1}$ indicates a substantially crystalline volume fraction of over 50%.

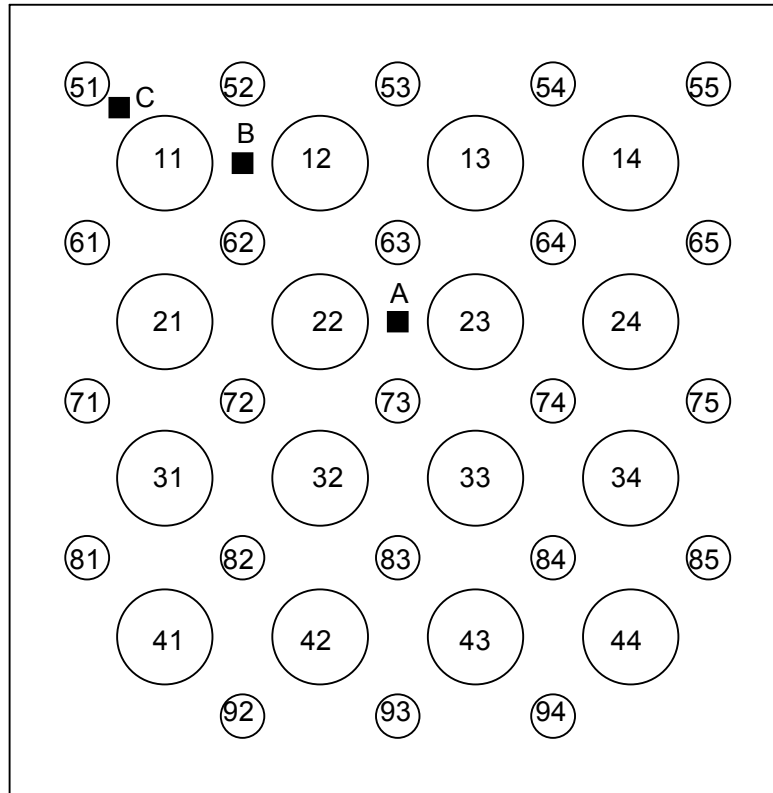


Figure 1. The solar cell distribution on a 4 cm \times 4 cm substrate, where the small circles are ITO dots with an area of 0.05 cm^2 and the large ones of 0.25 cm^2 . The squares, labeled A, B, and C, are the three areas where the Raman spectra, C-AFM image, and AFM morphology image were taken.

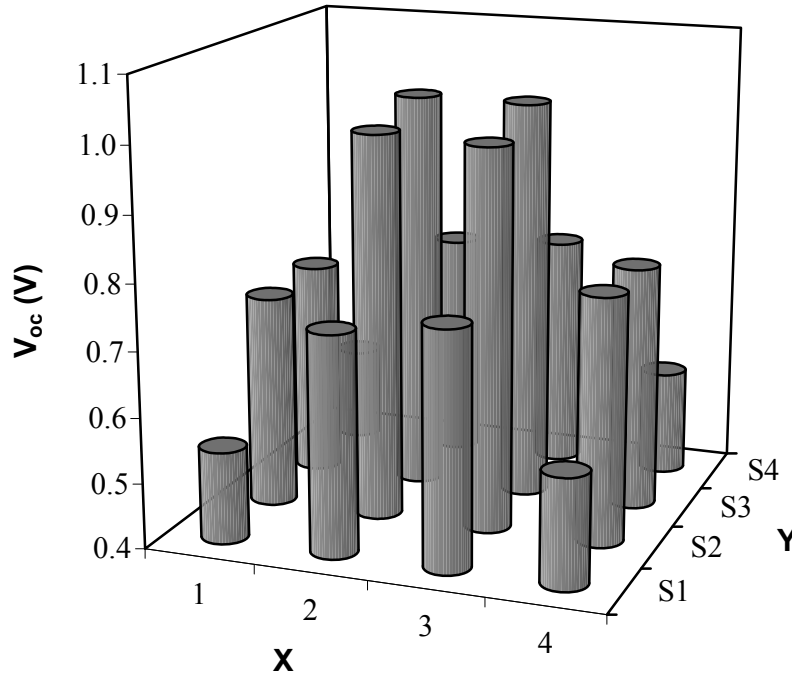


Figure 2. The V_{oc} distribution of the sixteen 0.25-cm^2 cells on the $4\text{ cm} \times 4\text{ cm}$ substrate.

C-AFM images along with AFM morphology images were also taken in areas A, B, and C on each sample. Figure 3 shows (a) the C-AFM image under a forward 1 V bias at the amorphous area (area A) of a mixed-phase silicon sample with 500-nm thick intrinsic layer and 10-nm thick fully amorphous buffer layer, and (b) the corresponding AFM morphology image. Although there are some current fluctuations, the local current does not change from location to location. However, in Fig. 4 (a), the C-AFM image at the mixed-phase area (area B) on the same sample shows two locations having very high current. Note that in Fig. 4 (a), the current scale is 1.0 nA/unit (compared to 30 pA/unit in Fig 3 (a)), which results in a flat current profile for the rest of area. The same data are shown in Fig. 4 (b) with a current scale of 30 pA/unit as used in Fig. 3 (a), where the background current mapping is similar to that in Fig. 3 (a). However, the two high-current spikes extend beyond the range of the graph. The most important observation is that the high current and low current regions are clearly distinguished and the transition edge is very sharp. Figure 4 (c) shows the AFM morphology of the same area as in Fig. 4 (a) and (b), where three large hill-like structures (marked with arrows) correspond to the two locations with high current spikes. Figure 5 (a) shows a C-AFM image for the substantially nanocrystalline region (area C) in the same sample. Numerous high-current spikes appear everywhere. Although the current-axis is 2.0 nA/unit (a factor of two larger than in image Fig. 4 (a)), the top parts of many spikes are still cut away. As shown in Fig. 5 (b), the morphology at the nanocrystalline area has many large hill-like structures. The size of these hill-like structures is around 500 nm in diameter.

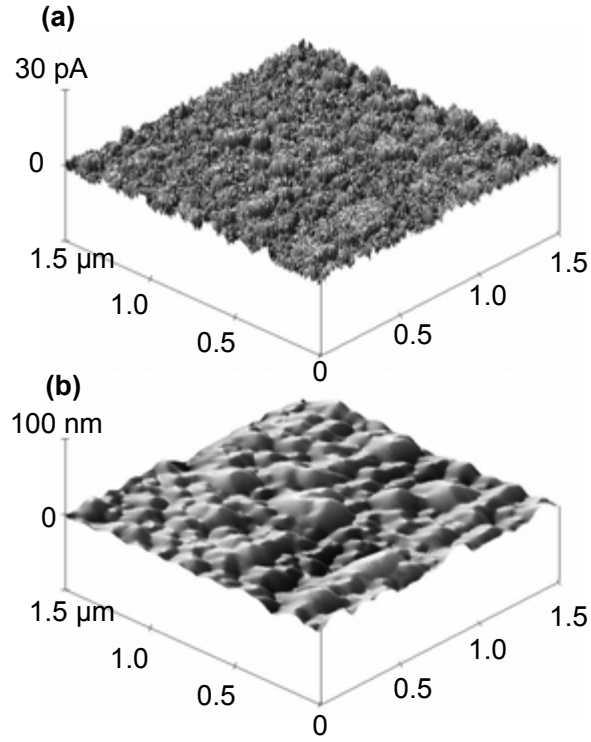


Figure 3. (a) The C-AFM image under 1.0 V forward bias in area A on an $n-i-p$ sample with a 500-nm thick intrinsic layer and a 10-nm thick fully a-Si:H i/p buffer layer and (b) the surface morphology image of the same area as the upper picture.

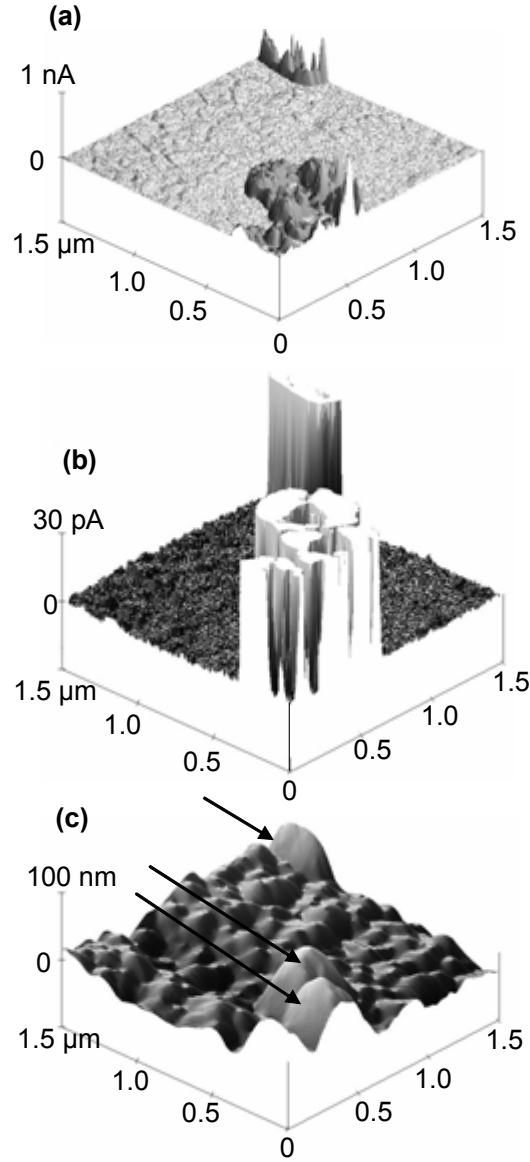


Figure 4. The upper (a) and middle (b) pictures are the C-AFM images under 1.0 V of forward bias in area B on the same sample as in Fig. 3, where current in the upper picture is in 1.0 nA/unit, while the middle one is in 30 pA/unit. The lower picture (c) is the morphology image in area B, where the three large hill-like structures as indicated by the arrows are clusters of nanocrystallites.

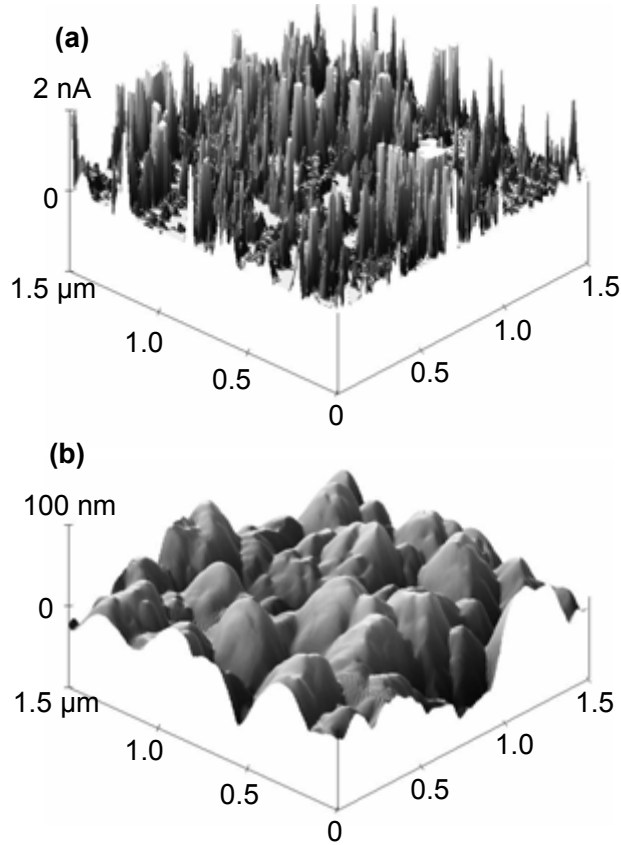


Figure 5. (a) the C-AFM image under 1.0 V of forward bias in area C on the same sample as in Fig. 5-6, where the current is in 2.0 nA/unit. (b) the morphology image in area C, where many large hill-like structures appear.

The mixed-phase material can be considered as nanocrystallites embedded in an amorphous matrix. The sizes of the nanocrystallites vary from a few nm up to 30 nm as measured by XRD and TEM. It could be even smaller for the mixed-phase materials with low volume fraction of nanocrystallites. Two difficulties arise in explaining some of the experimental results with such small crystallites. First, it is hard to imagine a two-phase model with the nanocrystalline phase forming a diode with such small nanocrystallites [17]. Second, the V_{oc} of mixed-phase cells drops dramatically for crystalline volume fractions much smaller than the percolation threshold. In fact, the V_{oc} starts to drop with increasing hydrogen dilution at a level that the material does not even show any nanocrystalline signature by XRD or Raman measurements. The C-AFM results allow us to address these two issues. By comparing the C-AFM and AFM morphology images, we find that the small nanocrystallites aggregate to form clusters with a size of ~ 500 nm in diameter. The significant difference of the forward current in the amorphous regions and the areas of nanocrystallite aggregations provides the evidence that nanocrystalline regions (aggregation or cluster of nanocrystallites) can be considered as diodes having nc-Si:H diode characteristics, while the surrounding amorphous regions act as an a-Si:H diode. The bandgap of the nanocrystalline areas should be around 1.1 eV (close to the crystalline silicon value); while in the amorphous areas, it is around 1.7-1.8 eV (similar to the a-Si:H value). With these bandgaps, the nc-Si:H diode should have a much higher forward current density than the a-Si:H diode under 1.0 V of forward bias. In addition, the aggregation of the nanocrystallites

results in a very non-uniform nanocrystallite distribution in a micro-scale. In the area of nanocrystallite aggregations, the high forward dark current leads to a dramatic drop in V_{oc} , even though the average nanocrystalline volume is much lower than the percolation threshold.

1.3.2. Light-induced change of local current flow in mixed-phase Si:H solar cells

In order to investigate the light-soaking and thermal annealing effects on the current flow through the nanocrystalline phase, we applied a fixed bias voltage of 0.75 V to the sample during the C-AFM measurements. The value was chosen to be between the V_{oc} of a-Si:H and nc-Si:H solar cells. As shown above, the nanocrystalline phase is not uniformly distributed in the amorphous matrix, but aggregates to form clusters. Each aggregate is substantially nanocrystalline and contains many small grains in the nanometer scale. The local current on the nanocrystalline aggregates is much larger than on the surrounding amorphous phase as shown in Figs. 6(a)-(f), where the high current regions are nanocrystalline aggregates. It should be pointed out that for multiple scans over the same area, the current image changes, as illustrated in Figs. 6(a)-(f). This probably results from the surface modification by the AFM tip. In the first scan, the current flow is very non-uniform in each individual aggregate. The non-uniformity was reduced in the second scan. We suspect that the improvement in the current uniformity could be caused by a mechanical modification of the p layer when the AFM tip contacted the sample surface, because the current image does not significantly depend on the bias voltage

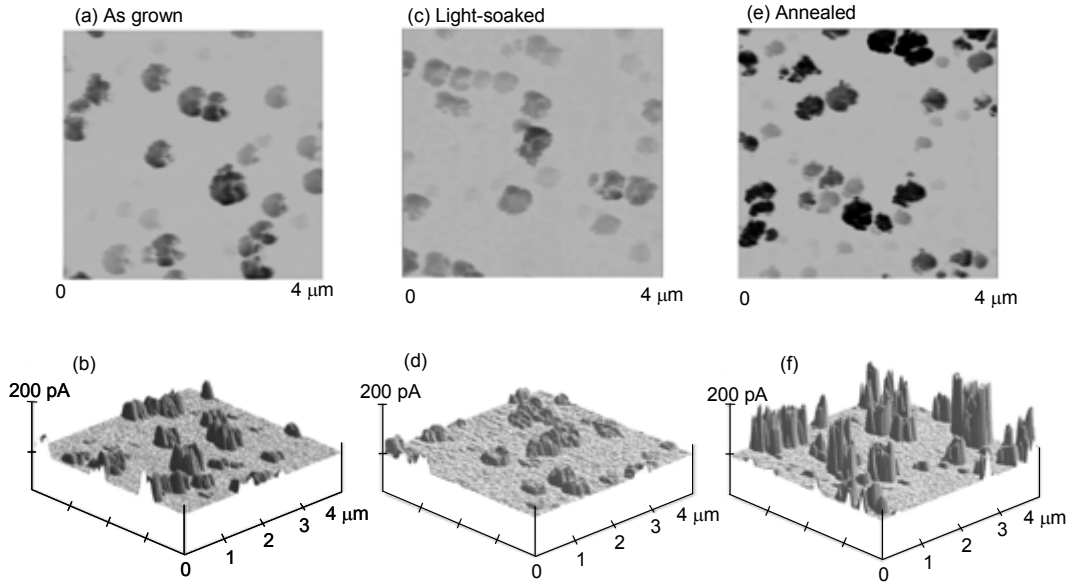


Figure 6. Examples of 2-D and 3-D C-AFM current images measured on an a-Si:H and nc-Si:H mixed-phase solar cell in the initial state (a) and (b), light-soaked-state (c) and (d), and thermal annealed state (e) and (f).

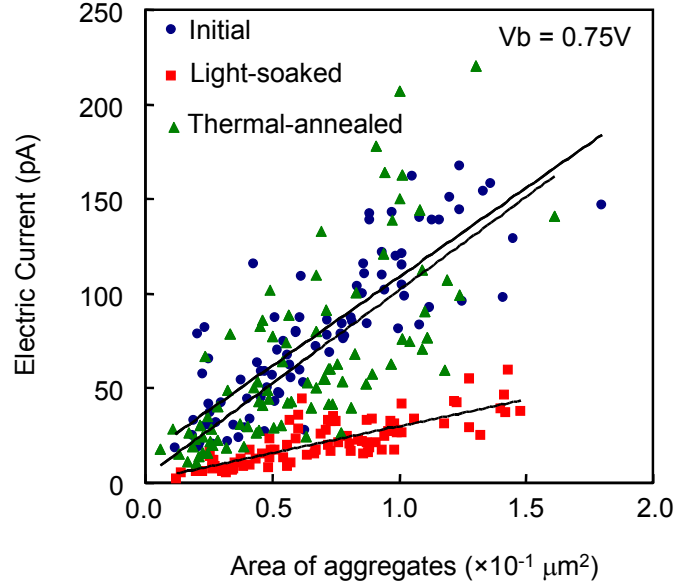


Figure 7. Electric current as a function of the aggregation area in the initial, light-soaked, and annealed states. Straight lines are linear fitting of the data and represent the current densities.

We took a large number of C-AFM images at different areas of the samples in the different states for statistical comparisons. Although the current values showed a large scattering, we found that a larger aggregate exhibits a higher average current value over the aggregate area. Figure 7 plots the average current value versus aggregate area. Although the data are very scattered, the average current values with the same size of aggregates at the initial and annealed states are similar and significantly larger than that at the light-soaked state. We further linearly fitted the current data versus aggregate area, and got the current densities of $(9.4 \pm 0.7) \times 10^{-1}$, $(2.8 \pm 0.3) \times 10^{-1}$, and $(10 \pm 1) \times 10^{-1}$ ($\text{nA}/\mu\text{m}^2$) for the initial, light-soaked, and annealed states, respectively. The similar current density on aggregates with different sizes reveals that the current flow in individual aggregates is limited by the size of the aggregates, but not by the tip-sample contact. This means that the current route spreads out in the nanocrystalline aggregates, and is not confined in small areas under the tip. The large scattering in the current data reflects structure fluctuations in the aggregates. Each aggregate contains a large number of small grains. The grain boundaries and amorphous component between the nanometer-size grains significantly affected the electron transport and resulted in the current density fluctuations.

The current density measurements by C-AFM above and other micro-electrical measurements reveal that the amorphous and nanocrystalline phases in the mixed-phase solar cells can be distinguished, and thus support the model that the V_{oc} of the mixed-phase solar cells can be considered from the two parallel-connected diodes. The light-induced decrease in average current density in the nanocrystalline aggregates further supports this model.

1.3.3. Doping effect on the material structure in mixed-phase Si:H solar cells

As presented above, we have measured the current flow on completed *n-i-p* solar cells using conductive atomic force microscopy (C-AFM) and observed high conduction paths through the nanocrystalline aggregations. We further investigated light-soaking and thermal-

annealing effects on the current flow through the nanocrystalline aggregations and found that the average forward current density over the nanocrystalline areas was reduced by light soaking and recovered to the initial values after thermal annealing.

In this section, we report our recent studies of phosphorus (P) doping effects on the microstructures and micro-electrical properties of the mixed-phase Si:H material. We found that adding PH_3 into the process gas moved the amorphous-to-nanocrystalline transition to a higher hydrogen dilution ratio required for achieving the similar Raman crystallinity. The nanocrystalline aggregation observed in the intrinsic Si:H materials disappeared in the mixed-phase films with high P doping, where isolated grains of nanometer sizes were distributed throughout the amorphous matrix. In addition, we found a dramatic increase in film conductivity in the heavily doped mixed-phase material having a small crystal volume fraction of 5%–10% estimated from Raman measurements.

Si:H films were deposited onto $4 \times 4 \text{ cm}^2$ stainless-steel substrates using a multiple-chamber plasma-enhanced chemical vapor deposition (PECVD) system. The intrinsic and P-doped films were deposited in the *i* and *n* chambers, respectively, for *n-i-p* solar cells. We adjusted the hydrogen-dilution ratio to obtain different structural properties and adjusted P-doping concentrations to vary film conductivities. We controlled the hydrogen dilution ratio so that the films were deposited in the amorphous/nanocrystalline transition regime. We were able to obtain various material structures from a single deposition on the same substrate: amorphous (from the center of the substrate), mixed-phase (along the edges of the substrate), and a high nanocrystalline volume fraction (near the four corners), as previously reported [8,9,14,15]. We deposited many samples with different hydrogen-dilution ratios and different P-doping levels and found that adding PH_3 in the gas phase significantly increased the hydrogen-dilution threshold required for reaching the amorphous/nanocrystalline transition. Here, we present three typical samples: one mixed-phase Si:H intrinsic film, one weakly P-doped mixed-phase Si:H film deposited in the *n*-chamber without intentional PH_3 flows, and one heavily P-doped film with a PH_3 -to- Si_2H_6 ratio of 3.3% and an increased hydrogen dilution by a factor of 2.3.

We used the AFM and C-AFM measurements to measure the surface morphology and local current flow. We also used cross-sectional transmission electron microscopy (X-TEM) to characterize the material structure long the growth direction. Raman measurements were carried out in the mixed-phase regions of the sample to identify regions of similar crystallinity for each sample. Secondary-ion mass spectrometry (SIMS) measurements were made to obtain P concentrations.

Although many samples have been characterized, the results from the three different types of samples of intrinsic, weakly P-doped, and heavily P-doped layers are presented in this report. Raman measurements showed that the crystallinity is similar for the three samples. An estimation from de-convolution of the Raman spectra showed that the crystal volume fraction was ~5%–10%. The SIMS analyses showed that the P contents are $3 \times 10^{18} \text{ at/cm}^3$ in the weakly doped sample, and $2 \times 10^{21} \text{ at/cm}^3$ in the heavily doped sample.

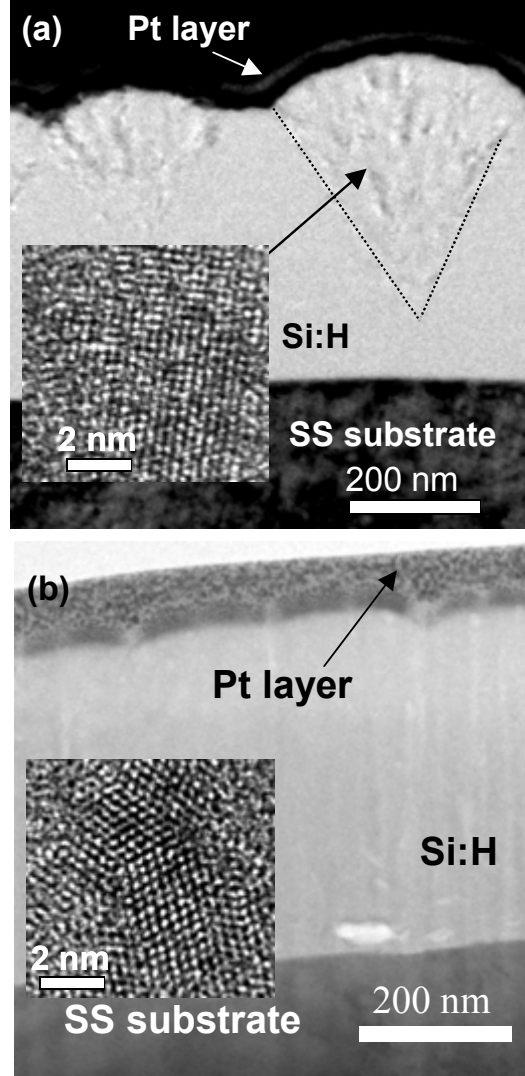


Figure 8. X-TEM images taken on (a) intrinsic and (b) heavily doped mixed-phase samples. High resolution images taken on the nc-Si:H aggregation in (a) and a grain embedded in the a-Si:H matrix in (b) are shown in the inset of the images.

Figure 8 shows X-TEM images of the intrinsic and heavily doped mixed-phase Si:H films, where the cone-shaped structures in Fig. 8(a) are nanocrystalline aggregations containing a large amount of nanometer-sized grains, as shown in the inset of the figure. This observation is consistent with our previously observed nanocrystalline aggregation in mixed-phase solar cells [8,9]. The low-level doping from the residual P in the deposition chamber did not affect the material structure, namely, the aggregation of nanometer-sized grains were still observed. The most important observation was the disappearance of the cone-shaped nanocrystalline aggregations in the heavily doped samples, as shown in Fig. 8(b), even though the Raman spectra obtained from this sample showed similar crystallinity to the other two samples. The high-resolution X-TEM image in the inset of Fig. 8(b) displays isolated nanometer-sized grains embedded in the amorphous matrix. Most likely, the nanocrystallites are randomly distributed in the a-Si:H matrix.

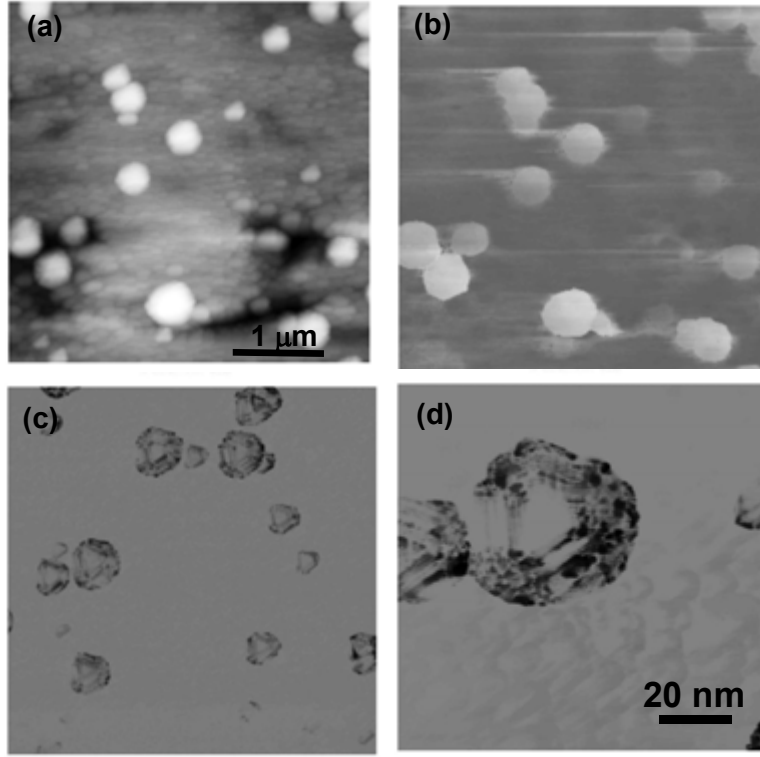


Figure 9. (a) An AFM and (b) corresponding C-AFM images taken under $V_b = +0.75$ V on the intrinsic mixed-phase sample. (c) shows a C-AFM image under $V_b = -0.75$ V on the same sample but different location, and (d) is a high-resolution image of (c).

We next investigate the local conduction path in the mixed-phase films with varying P-doping concentration. Figure 9 displays the following images from the intrinsic sample: (a) AFM topography, (b) C-AFM image with a $V_b = +0.75$ V electrical bias applied to the tip, (c) C-AFM image with a $V_b = -0.75$ V bias, and (d) negatively biased C-AFM image under high resolution. Figures 9 (a) and (b) were taken simultaneously in the exact same area, where the white spots in (a) are the aggregations of nanocrystallites and the corresponding white spots in (b) are the areas with high current through the tip. The clear correspondence between the nanocrystalline aggregations and the high current areas reveals that the transport paths are through the nanocrystalline aggregations [8–10,17]. The current on individual aggregations is relatively uniform, and the value depends on the size of the aggregations, exhibiting larger current values on larger-size aggregations, as shown in Fig. 9 (b). Under negative biases, the current value does not depend on the size of the aggregations and is non-uniform in individual aggregations, as seen in the higher-resolution image of Fig. 9 (d). The current pattern in Fig. 9 (d) resulted from the convolution of pyramidal AFM tip and spherical nc-Si:H aggregation, indicating the tip/film contact is the current-limiting factor when a negative bias voltage is applied to the tip. The averaged current values are $\bar{I} \approx 37$ pA and $\bar{I} \approx 4$ pA in Figs. 9 (b) and (c), showing a significant asymmetry under the positive and negative biases. By analyzing the current images and the asymmetry, we conclude that there is a contact diode between the AFM tip and the sample surface, and that any contact barrier that may exist between the film and the substrate is not a dominant factor for the current flow. For positive biases on the tip, the contact

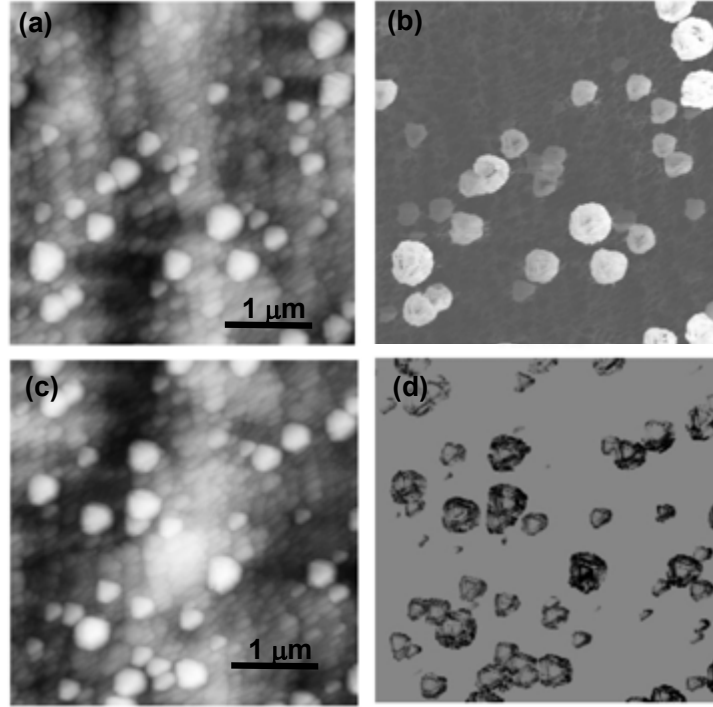


Figure 10. (a) An AFM and (b) corresponding C-AFM images taken on the weakly doped mixed-phase sample under $V_b = +0.75$ V. (c) and (d) show an AFM and the C-AFM images under $V_b = -0.75$ V.

diode of tip/film is forward biased, and hence, the current is limited by the intrinsic resistance of the film; however, for negative biases, it is limited by the tip/film contact barrier.

The AFM and C-AFM images on the mixed-phase region in the weakly P-doped sample are shown in Fig. 10. Similar features to the intrinsic mixed-phased samples are observed, indicating that a slight P-doping of $\sim 3 \times 10^{18} \text{at/cm}^3$ does not affect the structure of the mixed-phase Si:H film. The averaged current values in Figs. 10 (b) and (d) are $\bar{I} \approx 170$ pA and $\bar{I} \approx 90$ pA under $V_b = +0.75$ and $V_b = -0.75$ V, respectively, indicating that the small amount of P doping indeed increased the conductivity of the film.

Figure 11 shows the same measurements on the heavily P-doped mixed-phase Si:H samples, where both the positive and negative current images show no nanocrystalline aggregations formed in this sample. The averaged current values in Figs. 11 (b) and (d) are $\bar{I} \approx 130$ nA and $\bar{I} \approx 110$ nA under $V_b = +0.75$ V and $V_b = -0.75$ V, respectively. We also made the C-AFM measurement in the a-Si:H region of the heavily doped sample. The images exhibit uniform current distribution, and the averaged current values are $\bar{I} \approx 2$ nA and $\bar{I} \approx 70$ pA under $V_b = +0.75$ V and $V_b = -0.75$ V, respectively, showing that the conductivity increased dramatically by almost two orders of magnitude by the small crystal volume fraction of 5%–10%.

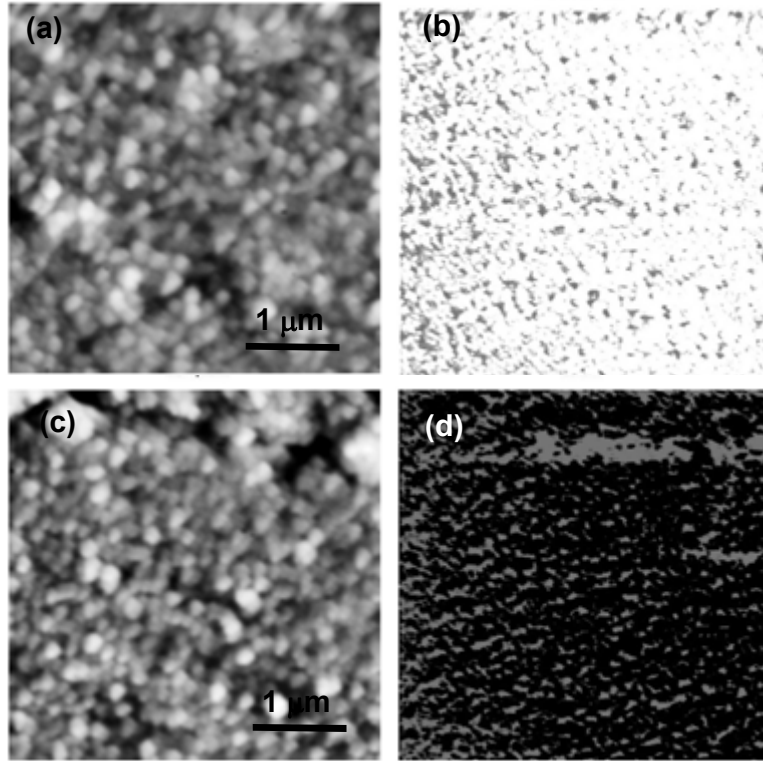


Figure 11. (a) AFM and (b) corresponding C-AFM images taken on the heavily doped mixed-phase sample under $V_b = +0.75$ V. (c) and (d) show the AFM and C-AFM images under $V_b = -0.75$ V.

Based on the atomic hydrogen enhanced surface diffusion model [2], the cone-shaped structure formation can be explained as follows. Once a nanograin is formed, the surface of the grain may have a higher sticking coefficient or a lower surface energy for Si radicals such as SiH_3 . This leads to a continuing growth of the nc-Si:H cone, and the growth rate of the nc-Si:H cone is higher than the surrounding a-Si:H area. Alternatively, the surface mobility on the nanocrystalline surface could be smaller than on the amorphous surface. Unbalanced surface diffusion rates could lead to a net flux of Si radicals laterally diffused into the nc-Si:H cone areas, resulting in an increased growth rate on the cone surfaces. This unbalanced diffusion model may explain X-TEM data of most nanocrystallites observed in the cone-shaped structure.

If the formation of nanocrystalline aggregations is caused by preferential growth on the crystalline surface, the nanocrystallite dispersion in the heavily P-doped mixed-phase Si:H materials could be explained as follows. P atoms or radicals have the tendency to reside on the surface of nanocrystallites. As discussed in the literature [18], phosphine can be adsorbed on the crystalline Si surface without being dissociated to form a stable layer with pentavalent P bridging adjoining Si atoms. The P-radical coverage on the grain surfaces may reduce the possibility of new nucleation because of the five-coordination of P. The P-radical coverage on the grain surfaces may also reduce the diffusion of Si radicals to grain surface areas. In addition, the P-doping levels of $\sim 2 \times 10^{21}$ at/cm³ might exceed the solubility of P in Si; therefore, the extra P tends to segregate on the grain boundaries and the surface of nanocrystallites. These mechanisms could prevent new nucleation on the existing grain surface. Therefore, new nucleation must

occur in the area without existing grains, where the formation energy of nucleation should be higher than the nanocrystallite surface in the intrinsic materials. In this case, a higher hydrogen dilution for nanocrystalline formation is needed and the nanocrystallites should dispersively distribute in the amorphous matrix. In the case of the weakly P-doped mixed-phase sample, the doping level of 3×10^{18} at/cm³ is well below the solubility of P in Si. The small amount of P is probably not sufficient to effectively prevent the nucleation on the existing grain surfaces to form nanocrystalline aggregations. Regarding the dramatic increase in current by the 5%–10% crystal volume fraction measured by Raman spectra, our X-TEM images show randomly distributed nanocrystallites embedded in the a-Si:H matrix; therefore, the possibility can be excluded of well-aligned nanocrystallite arrays along the film's vertical direction to form micro-filaments. The second possibility is the nonuniform distribution of P atoms. However, our high-resolution TEM and energy-dispersion spectra did not find any considerable P clusters, indicating that P does not aggregate within the scale of the measurement resolution. A highly speculative hypothesis is that P atoms may form a percolation of the narrow atomic chains in the regions of grain boundaries, leading to the high conduction paths. The existence of a small amount of nanograins provides the grain boundaries for P segregations to form P atomic chains. The last possibility is that the real crystal volume fraction is higher than detected by the Raman technique, because Raman scattering only detects grains larger than ~3 nm.

In summary, the compositional, structural, and electrical properties of mixed-phase Si:H thin films were investigated using SIMS, Raman spectroscopy, X-TEM, AFM, and C-AFM. We found that Si:H nanocrystallites in intrinsic and weakly P-doped materials aggregate to cone-shaped structures. The current under a positive bias on the tip in the nanocrystalline aggregations is significantly larger than that on the surrounding amorphous areas. A heavy P doping requires an increased hydrogen dilution to reach the amorphous/nanocrystalline transition. No nanocrystalline aggregations were observed in the heavily P-doped mixed-phase Si:H materials, where the nanometer-sized grains are dispersed in the amorphous matrix. With a 5%–10% Raman-detectable crystal volume fraction in the heavily doped film, the conductivity showed a dramatic increase by almost two orders in the current amplitude. The formation of the cone-shaped aggregation is explained by the atomic hydrogen enhanced surface diffusion model. Based on this model, the P-induced dispersion of Si nanocrystallites is explained by the coverage of P-related radicals on the existing nanocrystalline surface during the deposition and the P segregation in grain boundaries, which prevent new nucleation on the surface of existing nanocrystallites.

2. Correlation of hydrogen dilution profiling with material structure and solar cell performance

2. 1. Introduction

Hydrogen dilution is a key parameter for controlling the transition from a-Si:H to nc-Si:H. The structure analyses showed that nc-Si:H films deposited with a constant hydrogen dilution normally exhibit an initial amorphous incubation layer, followed by nucleation and growth of cone-like nanocrystalline clusters. As the growth of the nanocrystalline cone-structures, the crystalline volume fraction and average grain-size increase with the film thickness [6,19-21], a phenomenon called nanocrystalline evolution. It was also found that nc-Si:H solar cells made with a hydrogen dilution close to the amorphous/nanocrystalline transition showed a better performance than those with a higher crystalline volume fraction [13]. The nc-Si:H materials with a high crystalline volume fraction normally have a high density of micro-voids and cracks, which results in ambient degradation caused by impurity diffusion [22]. It is obvious that with a constant hydrogen dilution, it is very difficult to maintain the material structure close to the amorphous/nanocrystalline transition regime throughout the sample thickness. If the hydrogen dilution is low, there will be a thick amorphous incubation layer; on the other hand, if the hydrogen dilution is high, the top layer of the material will have a high crystalline volume fraction with a high porosity. In order to suppress the nanocrystalline evolution phenomenon, we have developed a hydrogen dilution profiling method, where the hydrogen dilution ratio is dynamically reduced during the deposition, to control the material structure along the growth direction [23]. We also showed that this method was an effective way to increase solar cell efficiency. Since then, many groups have used the hydrogen dilution techniques and improved their nc-Si:H solar cell efficiency [24-26]. Recent materials characterizations with Raman spectroscopy indeed showed that the crystalline volume fraction was controlled. In some cases, the crystalline volume fraction was suppressed with increasing film thickness [27]. Drive-level capacitance profile (DLCP) measurements demonstrated that defect density was reduced in the hydrogen dilution profiled samples. In addition, the defect density distribution along film thickness was flatter in the samples made with hydrogen dilution profiling than with constant hydrogen dilution [28]. Therefore, it is conclusive that proper hydrogen dilution is an effective method to increase nc-Si:H solar cell efficiency. However, one can use various hydrogen dilution profiles such as different average dilution ratios, different functional forms of dynamical flow rates of the active gas and hydrogen, and different ranges of the dilution. Furthermore, one optimized hydrogen dilution profile obtained under a given condition does not necessarily apply to other conditions. Therefore, a systematic study of material structure and solar cell performance as a function of hydrogen dilution profile should improve our understanding of the nc-Si:H growth mechanism and materials properties and provide additional information for optimizing nc-Si:H solar cell performance.

Under this program, we have carried out a systematic study of material structures and solar cell performance for nc-Si:H solar cells made with various hydrogen dilution profiles. The material structure characterizations were carried out at NREL.

2. 2. Experimental details

nc-Si:H *n-i-p* solar cells were made on bare stainless steel (SS) and Ag/ZnO back reflector coated SS substrates. The doped layers as well as *n/i* and *i/p* buffer layers were deposited using RF glow discharge under the same conditions for all samples. The nc-Si:H intrinsic layer was made using modified very high frequency (MVHF) glow discharge at high rates with various hydrogen dilution profiles. Before nc-Si:H deposition, an optimized seeding layer was made with a very high hydrogen dilution to reduce the amorphous incubation layer. The solar cell performance was characterized using current density versus voltage (J-V) measurements under an AM1.5 solar simulator at 25°C and quantum efficiency (QE) measurements under the short-circuit condition for short-circuit current density (J_{sc}) calibration. The material structure properties were characterized using Raman spectroscopy, cross-sectional transmission electron microscopy (X-TEM), atomic force microscopy (AFM), and conductive AFM (C-AFM) at NREL.

2. 3. Results and discussion

2.3.1. Material structures

First, we made four nc-Si:H solar cells on bare SS to compare the effect of hydrogen dilution profiling on solar cell performance, electronic structure, and microstructure. During the intrinsic layer growth, the hydrogen flow rate was kept constant and the same value was used for all the samples, whereas the Si_2H_6 flow rate varied as different functions of time as illustrated in Fig. 12. The identification numbers of the four samples are listed in Table I. The total amount of Si_2H_6 flow during the intrinsic layer deposition was the same for all the samples, and therefore the average hydrogen dilution ratio was the same. Because hydrogen dilution is normally defined as the ratio of H_2/SiH_4 or H_2/Si_2H_6 , the hydrogen dilution functions are actually the inverse functions of the curves in Fig. 12. Compared to the constant hydrogen dilution, the three ramping curves result in a high initial hydrogen dilution and it continually decreases with time. Among the three ramping curves, the t^2 flow rate curve has the most rapid change in the dilution ratio, corresponding to the highest hydrogen dilution at the beginning of the deposition (the region close to the substrate) and the lowest hydrogen dilution at the end of the deposition (close to the top surface). The linear curve gives moderate ramping and the $t^{1/2}$ curve produces the slowest ramping.

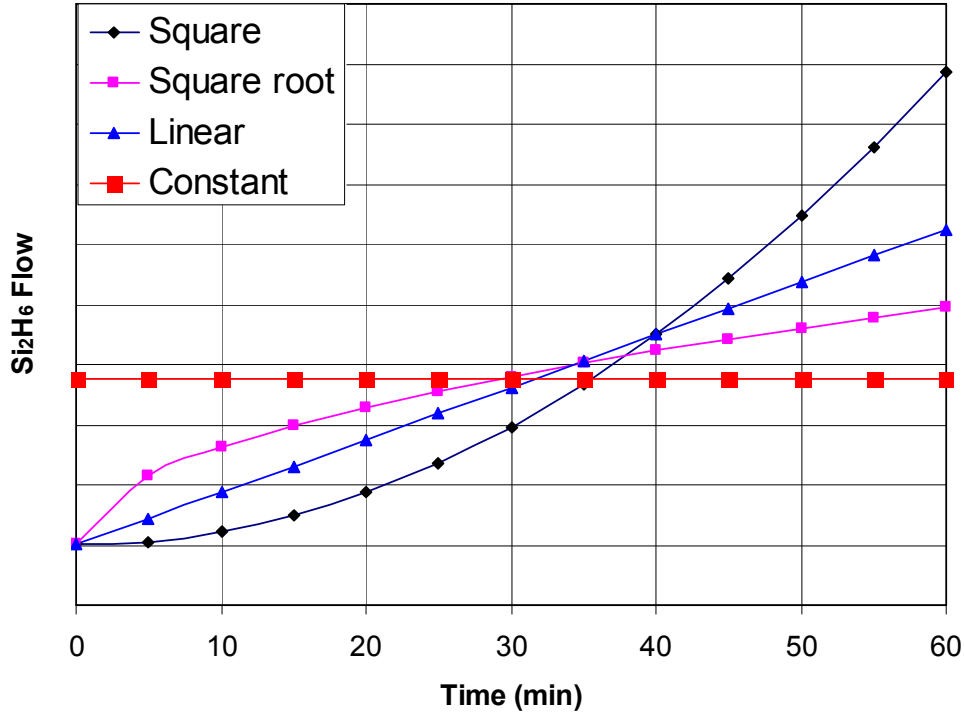


Figure 12. Si_2H_6 flow rate as functions of time during the nc-Si:H intrinsic layer depositions of the four samples on SS substrates.

The main purpose of the hydrogen dilution profiling is to control the nanocrystalline evolution and to obtain uniform crystalline volume fraction along the growth direction. Normally, an increase of crystalline volume fraction with thickness was observed when constant hydrogen dilution was used [6,19-21]. Based on the X-TEM observation, a cone growth model for the nanocrystalline evolution has been proposed [1,4]. In this model, under constant hydrogen dilution, higher than a threshold value, nanocrystallite nucleation appears after an amorphous incubation layer and then nanocrystalline cones grow with the thickness of the film until the neighboring cones meet each other. Therefore, in the initial growth of nc-Si:H, the crystalline volume fraction increases with the film thickness. In addition, new nucleation formations during the deposition could lead to extra contributions for the increase of crystalline volume fraction. The concept of hydrogen dilution profiling is to have a very high hydrogen dilution to produce large amounts of nucleation sites in the beginning of deposition and reduce the hydrogen dilution ratio to control the cone growth and reduce the probability of new nucleation sites. Ideally, an optimized hydrogen dilution profiling would result in uniform crystalline distribution along the film thickness. However, an over-profiled hydrogen dilution might cause an inversed nanocrystalline evolution, which means that the bottom layer of the film has a higher crystalline volume fraction than the top layer of the film.

To check whether hydrogen dilution profiling controls the material structures, Raman measurements were made on four samples. Figure 13 shows the Raman spectra of the four nc-Si:H samples excited by (a) a green laser with a wavelength of 532 nm and by (b) a red laser with a wavelength of 633 nm. Normally, the Si Raman TO mode in nc-Si:H can be deconvoluted into three components: a broad amorphous peak at $\sim 480 \text{ cm}^{-1}$, an intermediate peak

at $\sim 510 \text{ cm}^{-1}$, and a crystalline peak at $\sim 520 \text{ cm}^{-1}$. The intermediate peak could be assigned to the scattering from distorted Si-Si bonds in the grain boundaries or in the grains with a size smaller than 3 nm. The crystalline volume fraction (f_c) is calculated from the ratio of the component areas obtained by de-convolution of Raman spectra,

$$f_c = \frac{I_{520} + I_{510}}{I_{520} + I_{510} + \gamma I_{480}}, \quad (1)$$

Where γ is the ratio of Raman emission cross sections of crystalline and amorphous components [29-31]. Because the estimation of γ is complicated and no agreeable value in the literature is given, we simply use $\gamma=1$ for the calculation of Raman crystallinity. Although this may introduce errors in the absolute crystalline volume fraction values, nevertheless, it can give a reasonable comparison of crystal volume fraction between samples.

Table I lists the results of Raman spectrum de-convolutions and the crystalline volume fraction for the four samples with the excitation lasers used. Normally, one believes that the green laser probes the material structure in the top surface region and the red laser measures the material structure in the bulk of the film. It is surprising that the sample with a constant hydrogen dilution shows very similar crystalline volume fractions measured by the green and the red lasers, indicating uniform crystallinity distribution along the film growth direction. Two possible explanations can be proposed for this observation. First, there is indeed no nanocrystalline evolution because of the well-optimized seeding layer. Second, the measurement with the green laser was influenced by the a-Si:H *i/p* buffer layer. In order to distinguish the two mechanisms, additional measurements using different techniques are needed. The sample made with the $t^{1/2}$ Si₂H₆ ramping also shows a reasonably uniform crystalline volume fraction. The samples made with linear and t^2 Si₂H₆ ramping show inversed nanocrystalline evolution, where the crystalline volume fraction measured with the green laser is much smaller than with the red laser. In particular, the sample with the t^2 ramping shows a very large amorphous peak as shown in the top plot in Fig. 13.

Table I. Raman spectrum de-composition parameters and crystalline volume fractions of nc-Si:H samples made with different hydrogen dilution profiles, where *a*, *i*, and *c* represent the amorphous, intermediate, and crystalline peaks.

Run No.	λ_{ex} (nm)	Area			Peak (cm^{-1})			f_c (%)	Si ₂ H ₆ profiling
		<i>a</i>	<i>i</i>	<i>c</i>	<i>a</i>	<i>i</i>	<i>c</i>		
15117	532	21.8	5.0	7.9	479.9	508.5	519.0	37.2	Linear
	632.8	11.1	4.8	7.1	482.5	513.1	520.5	51.8	
15121	532	43.0	14.4	5.6	470.8	499.5	519.0	31.7	t^2
	632.8	15.1	4.9	6.5	482.5	514.0	521.4	43.0	
15123	532	12.7	5.3	8.3	481.4	510.0	519.0	51.7	$t^{1/2}$
	632.8	8.5	4.8	6.2	483.5	514.9	521.4	56.3	
15125	532	9.1	4.9	7.9	487.4	513.0	520.5	58.4	Constant
	632.8	7.3	5.1	6.5	487.2	514.9	521.4	61.4	

In order to confirm the Raman results, the samples were characterized using X-TEM at NREL. The X-TEM samples were prepared by the focused ion beam (FIB) technique. A 50-nm thick Pt layer was deposited on the sample surface and an 80-nm-thick slice of the sample was cut off using the FIB. Figure 14 shows the medium resolution X-TEM pictures of the four samples. It appears that all of the samples show some elongated structures perpendicular to the substrates. Based on the analyses in the literature [1,11], these structures are assigned to large nanocrystalline clusters called large grains. If this assignment is correct, the following observations are made:

1. There is no incubation layer in the n/i interface region. The 70-nm thick smooth region near the substrate is the n layer and the a-Si:H buffer layer.
2. The samples made with the constant hydrogen dilution and the $t^{1/2}$ Si₂H₆ ramping showed uniform nanocrystalline distributions throughout the film thickness, consistent with the Raman measurement.
3. By carefully evaluating the images, one can see that the sample made with the constant hydrogen dilution (15125) shows a certain degree of extra elongated structures in the top half of the sample than the bottom half of the sample. The sample made with the $t^{1/2}$ Si₂H₆ ramping (15123) shows an opposite trend, which means that the crystalline volume fraction slightly decreases with the film thickness, as we expected.
4. The inversed nanocrystalline evolution becomes clear for the samples with the linear and t^2 ramping (15121, 15123). In particular, the sample made with the t^2 ramping has a 200-300-nm thick layer in the top region with no indication of nanocrystallite inclusions. High resolution images reveal that the top layer is indeed amorphous silicon.

To summarize the Raman and X-TEM measurements, we find that the sample made with constant hydrogen dilution shows no obvious nanocrystalline evolution, which might result from the optimized seeding layer. The hydrogen dilution profiles result in an inversed nanocrystalline evolution, where the crystalline volume fraction decreases with film thickness. The t^2 of Si₂H₆ profile leads to an amorphous layer in the top region of the film.

Figure 15 shows (upper picture) the AFM image on the top surfaces and (lower picture) C-AFM image of the same areas on the nc-Si:H solar cell made with constant hydrogen dilution. The C-AFM image was taken with 1-V positive electrical bias. From the topographic image, one can see that many hill-like structures are distributed on the surface. We believe that they are clusters of nanocrystallites. The C-AFM image shows many high current spikes on the surface, which are normally observed in nc-Si:H solar cells. Figure 16 shows similar images taken on the surface of the sample made with t^2 ramping of Si₂H₆. The AFM topography is similar to the one made with constant hydrogen dilution. The current spikes in the C-AFM image of the sample with t^2 Si₂H₆ profile are much smaller than those on the sample with the constant hydrogen dilution. Our previous results showed that a thick a-Si:H p/i buffer layer effectively reduces the shunt current [8]. The extra amorphous layer caused by the hydrogen dilution profile acts as an a-Si:H buffer layer.

2.3.2. Solar cell performance

We used hydrogen dilution profiles similar to those listed in Table I for nc-Si:H single-junction solar cells on Ag/ZnO coated SS substrates. Table II lists the cell performance data of the cells with different profiles of Si₂H₆ flow rate. The first four cells were made with the same

average hydrogen dilution ratio. It appears that the cell with a constant hydrogen dilution shows the lowest efficiency due to a lower V_{oc} and poorer FF, which could be due to a high crystallinity near the i/p interface. The cell made with a Si_2H_6 flow rate following the t^2 function also shows a poor performance. The FF is lower due to a high series resistance caused by the amorphous component near the i/p interface as shown by the Raman and X-TEM results. The linear and $t^{1/2}$ profiles of Si_2H_6 flow rate improved the cell performance remarkably; in particular the cell with the $t^{1/2}$ Si_2H_6 ramping showed an efficiency of 8.7%. We further optimized the average hydrogen dilution with the $t^{1/2}$ profile and improved the efficiency to 9.1% as listed in the last row of Table II.

2. 4. Summary

We have systematically studied the structural properties of nc-Si:H materials made with various hydrogen dilution profiles using Raman spectroscopy, X-TEM, AFM, and C-AFM. The solar cell performance correlates well with the material structures. Based on the experimental results, we make the following conclusions:

1. The nc-Si:H materials do not have an incubation layer, indicating that the seeding layer is well optimized and works as per design.
2. With the optimized seeding layer, no significant nanocrystalline evolution is observed even though a constant hydrogen dilution was used.
3. Hydrogen dilution profiling can control the microstructure. The best nc-Si:H single-junction solar cell was made using a hydrogen dilution profile, consisting of a constant hydrogen flow rate and an increasing Si_2H_6 flow rate following a $t^{1/2}$ function.

If the hydrogen dilution ratio decreases too steeply, an inversed nanocrystalline evolution can occur. In general, a slightly inversed nanocrystalline evolution should benefit the cell performance. However, too thick of an amorphous component in the i/p interface region causes additional series resistance and results in poorer cell performance.

Table II. J-V characteristics of nc-Si:H single junction solar cells made with different Si_2H_6 flow rate profiles in the intrinsic layers. The first four cells have the same average dilution ratio and the last one has a reduced hydrogen dilution ratio.

Run No.	V_{oc} (V)	FF	Q (>610nm) (mA/cm ²)	P_{max} (mW/cm ²)	Si_2H_6 ramping
15589	0.558	0.505	25.68(14.24)	7.24	Linear
15590	0.539	0.611	26.32(14.60)	8.67	$t^{0.5}$
15592	0.572	0.385	25.33(14.08)	5.56	t^2
15593	0.528	0.388	25.43(13.79)	5.21	Constant
15591	0.567	0.631	25.50(13.87)	9.12	$t^{0.5}$

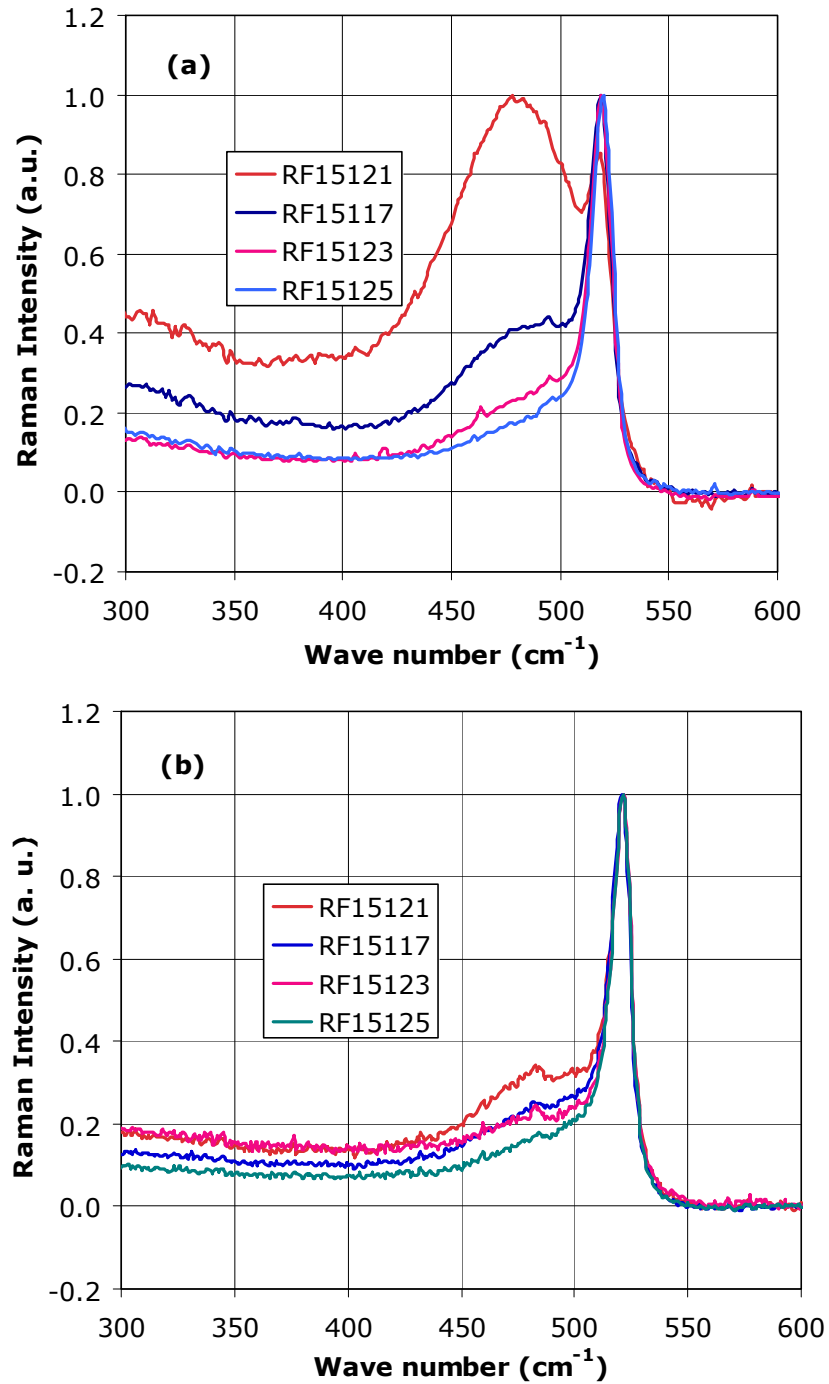


Figure 13. Raman spectra of four nc-Si:H solar cells made with different hydrogen dilution profiles. The measurements were made with (a) a green laser of 532-nm wavelength and (b) a red laser with 632.8-nm wavelength.

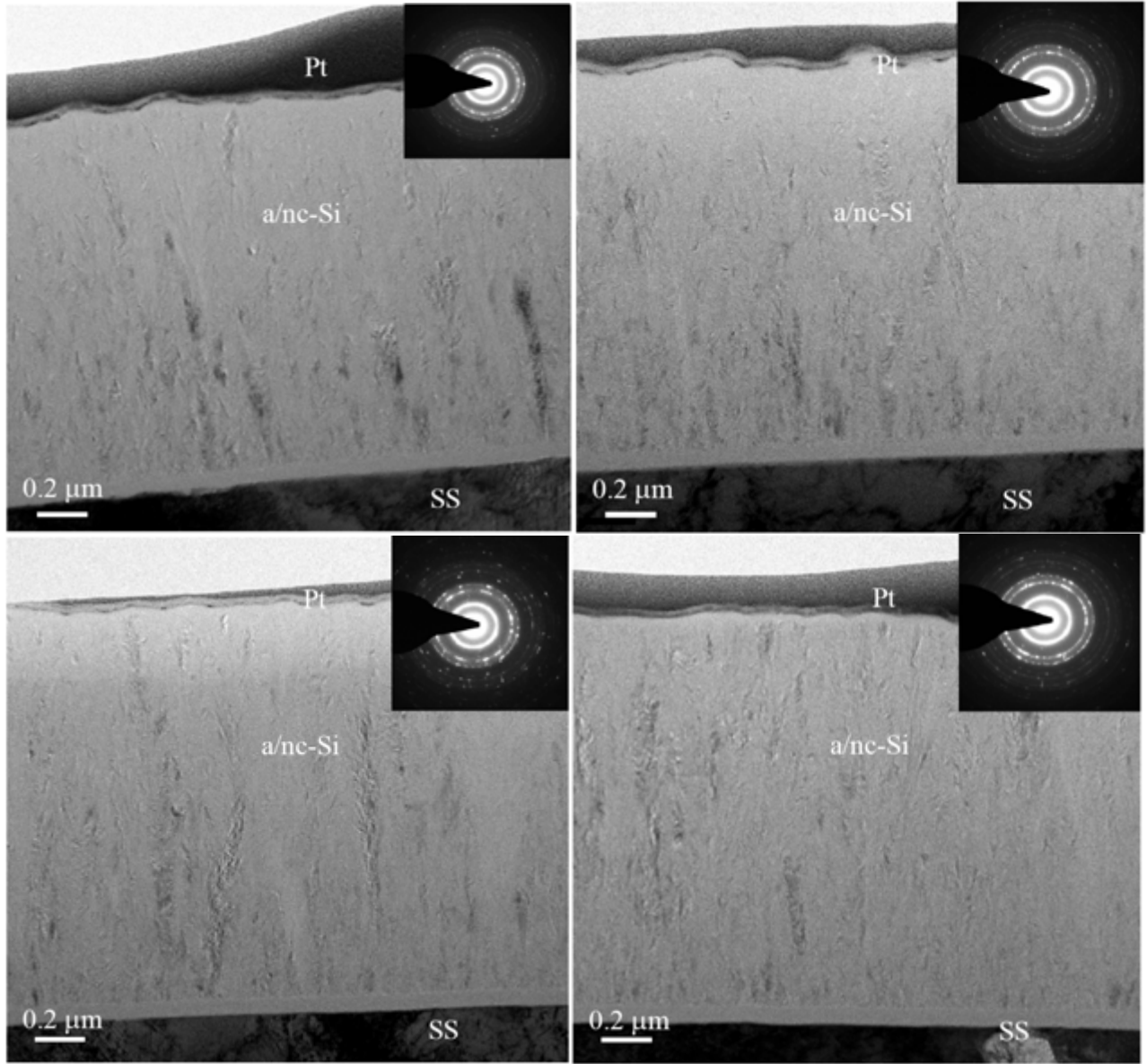


Figure 14. X-TEM images of the four samples made with different Si_2H_6 ramping, where the upper left picture is from the sample made with Si_2H_6 ramped with linear function, the upper right Si_2H_6 ramped with t^2 function, the lower left Si_2H_6 ramped with $t^{1/2}$ function, and the lower right a constant Si_2H_6 flow rate.

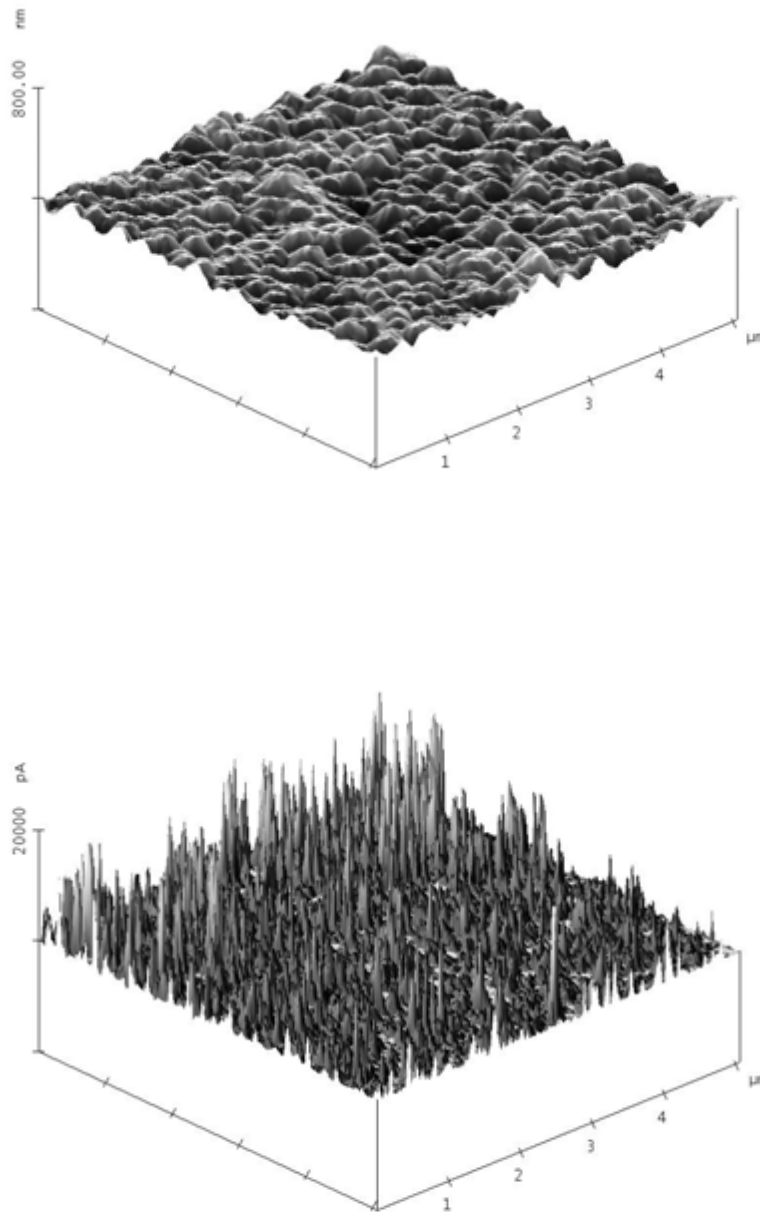


Figure 15. The upper picture shows an AFM morphology image and the lower one is the corresponding C-AFM image on a nc-Si:H solar cell made with a constant hydrogen dilution (sample 15125).

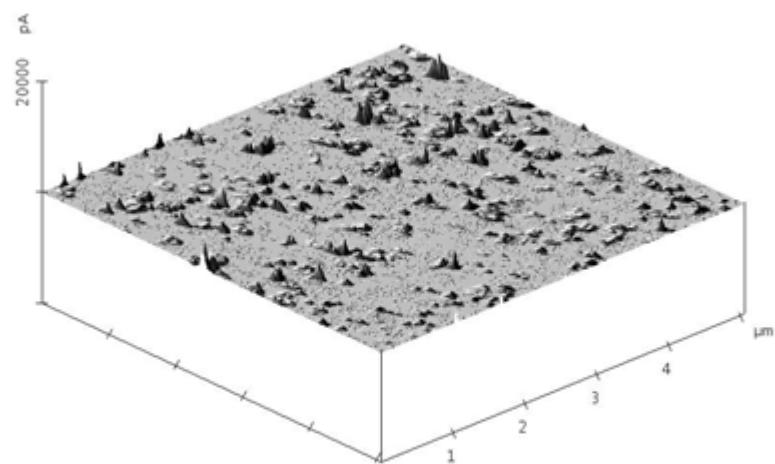
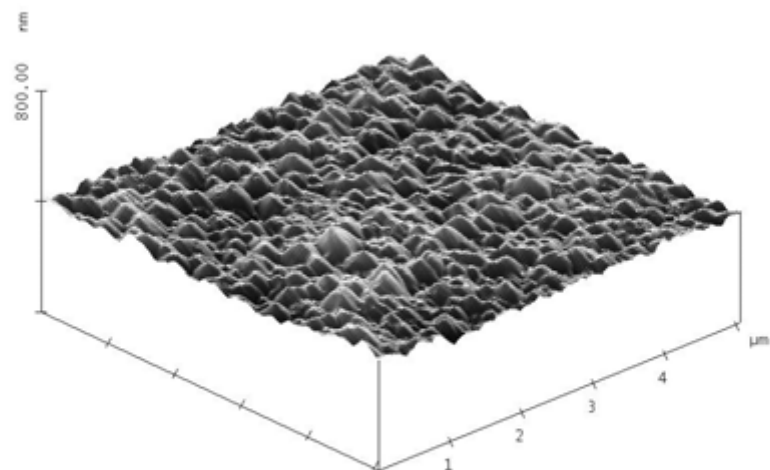


Figure 16. The upper picture shows an AFM morphology image and the lower one is the corresponding C-AFM image on a nc-Si:H solar cell made with a t^2 ramping of Si_2H_6 (sample 15121).

3. Optimization of Ag/ZnO back reflector

3. 1. Introduction

High efficiency thin film solar cells need not only high quality active semiconductor layers, but also inactive contact layers such as top transparent contact and bottom contact. At United Solar, high efficiency a-Si:H and a-SiGe:H alloys, and nc-Si:H solar cells are deposited on Al/ZnO or Ag/ZnO back reflector coated stainless steel substrates. The function of the metal coating is to reflect the light reaching the substrate, and the ZnO enhances the scattering of light through increased surface texture. United Solar's back reflectors have been developed since the early 90s [32]. We have successfully implemented the optimized back reflectors in several roll-to-roll manufacturing lines. In recent years, nc-Si:H based solar cells have gradually dominated the research and development of high efficiency silicon based thin film solar cells because of their higher current density and better stability than the a-Si:H and a-SiGe:H cells. The multi-junction solar cells with a-Si:H in the top cell and nc-Si:H bottom cell promise higher efficiencies than the conventional a-Si:H/a-SiGe:H/a-SiGe:H triple-junction structure. We have achieved an initial and stable active-area efficiency of 15.1% and 13.3%, respectively, using the a-Si:H/a-SiGe:H/nc-Si:H and a-Si:H/nc-Si:H/nc-Si:H triple-junction solar cells [33, 34]. These results have surpassed the records achieved using the conventional a-Si:H/a-SiGe:H/a-SiGe:H triple-junction structure [35]. The high efficiency was partially due to an improved back reflector with more effective light trapping [36].

For thin film solar cells, when light reaches the substrates, it is either reflected back to the cell or absorbed by the substrate. In order to reduce the absorption in the substrate and enhance the reflection, metal layers such as Al and Ag are used as a back reflector, and the metal surface is textured for enhanced light scattering. In addition, a dielectric layer such as ZnO is used for additional texturing and more efficient light scattering. Furthermore, it has been reported that a flat metal layer and a textured ZnO layer are the best combination because the flat metal surface can reduce the plasmon absorption at the metal/dielectric interface [37]. Although a significant amount of work has been done on the optimization of the light trapping effect [32, 36], a reliable calculation method of the optical enhancement, defined as the number of paths that light can travel in the solar cells, has not been established. An early work by Yablonovitch showed that the maximum optical enhancement is $4n^2$ [38], where n is the optical index of the thin film semiconductor layer. The $4n^2$ factor is called Yablonovitch enhancement for stochastic light trapping. In silicon, this number is about 50.

Under this program, we have made a systematic study of the Ag/ZnO back reflector deposition and characterization. We deposited nc-Si:H and a-SiGe:H single-junction solar cells on various back reflectors and correlated the cell performance to the back reflector properties. The QE curves of nc-Si:H and a-SiGe:H single-junction cells on various substrates were compared. We proposed an analysis method for estimating the optical enhancement by Ag/ZnO back reflector substrates.

3. 2. Experimental details

Ag/ZnO back reflectors were deposited in a batch machine with sputtering under different conditions. Two types of Ag layers were used: a textured Ag layer similar to our conventional Ag/ZnO and a flat, specular Ag layer reduce the parasitical loss at the Ag/ZnO interface. Different ZnO thicknesses were used to increase the texture. The material structures were measured at NREL using X-ray diffraction (XRD) and atomic force microscopy (AFM). The optical properties were characterized by total reflection measurements.

We deposited a-SiGe:H and nc-Si:H single-junction solar cells using a multi-chamber glow discharge system on different back reflectors. Current-density versus voltage (J-V) characteristics were measured under an AM1.5 solar simulator and QE curves were measured under the short circuit condition.

3. 3. Results and discussion

3.3.1. Structural analysis

Table III list the Ag/ZnO back reflector samples characterized at NREL using XRD and AFM. Figure 17 shows the XRD spectra of the baseline sample R1938. From the plot in a wide range (Fig. 17 (a)), eight peaks were observed with the identifications marked in the plot.

Table III. Ag/ZnO structural properties.

Sample ID	ZnO thickness (μm)	ZnO Ts	Ag state
5R1938	0.8	High	Textured
5R2040	0.6	High	Textured
5R2141	1.8	High	Textured
R8272	0.5	Low	Textured
R8273	1.1	Low	Textured
R8283	1.5	Low	Textured
R8286	2.0	Low	Textured
R8322	3.0	Low	Textured
R8289	0.5	Low	Flat
R8290	1.0	Low	Flat
R8306	1.5	Low	Flat
R8314	2.0	Low	Flat
R8316	3.0	Low	Flat
R8568	0.5	High	Flat
R8578	2.0	High	Flat
R8567	0.5	High	Textured
R8483	2.0	High	Textured
R8562	2.0	High	Textured
R8342	2.0	High	Textured

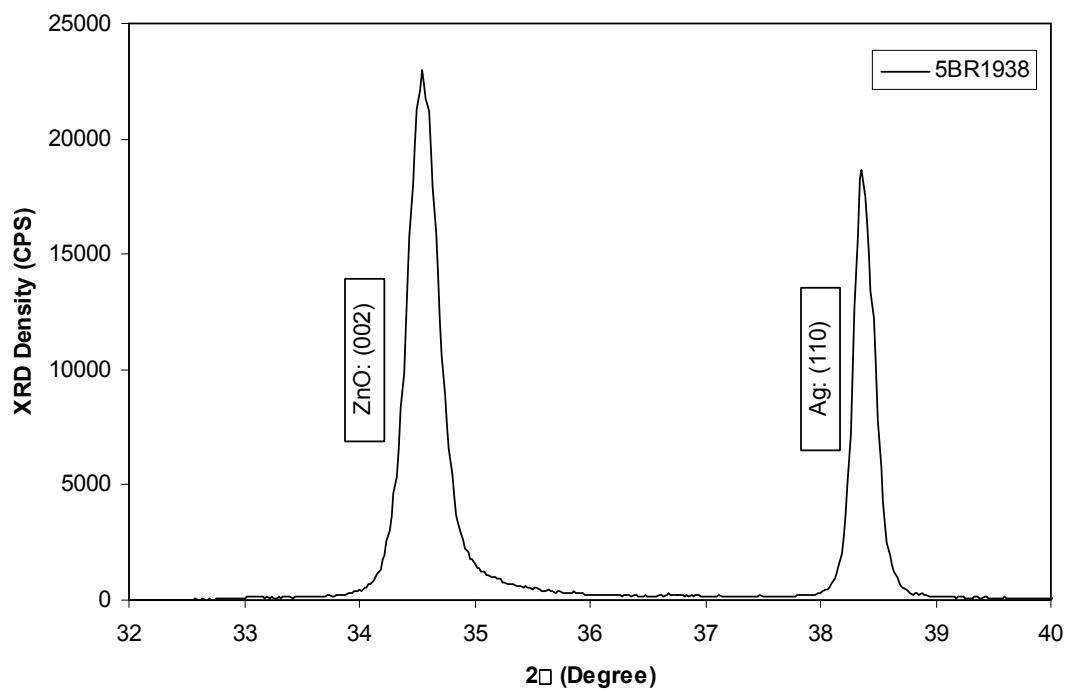
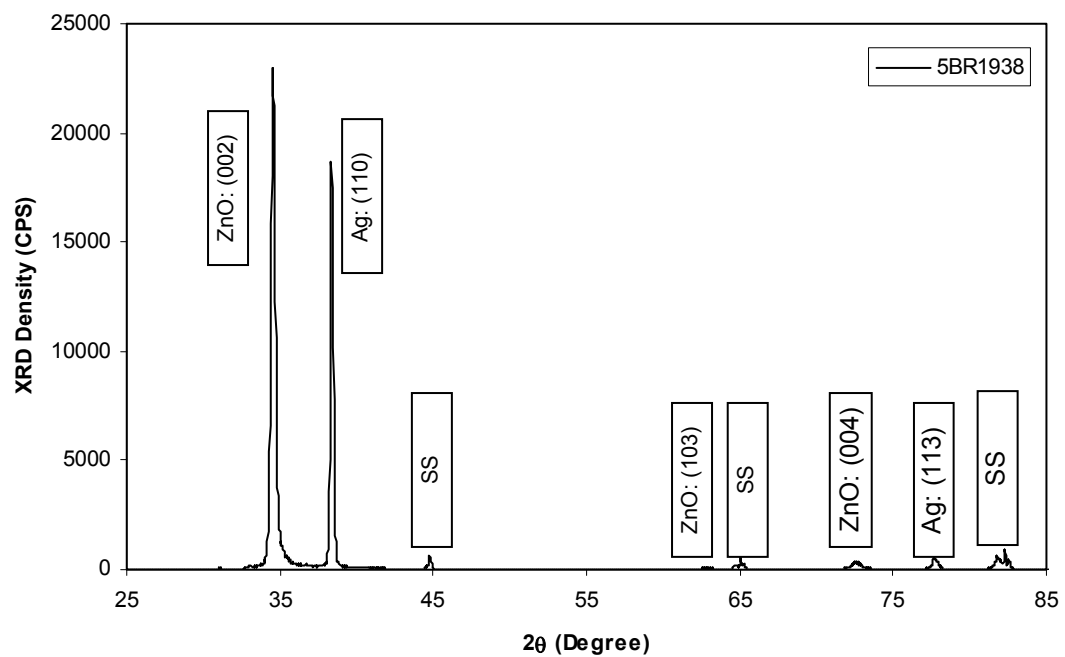


Figure 17. XRD spectra of BR1938 (a) in a wide range and (b) in a narrow range.

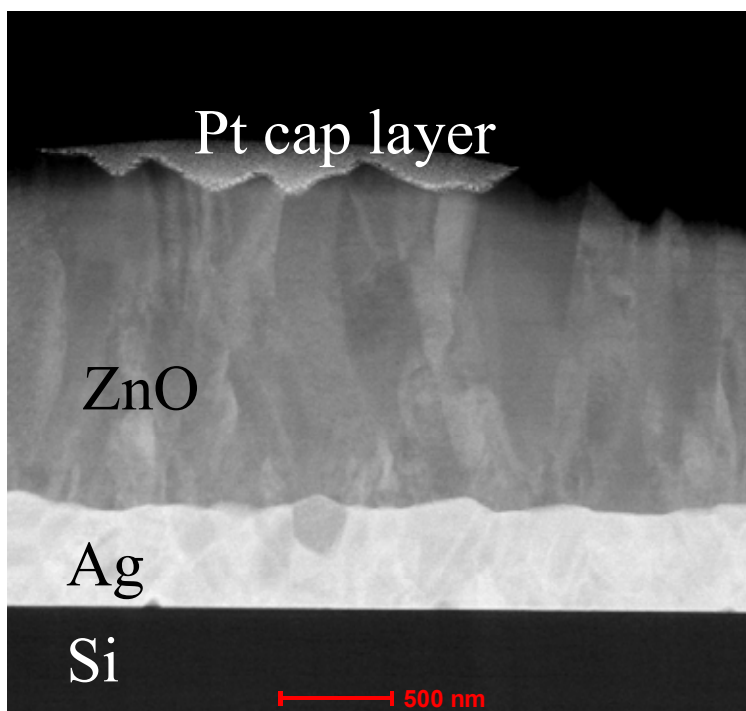


Figure 18. X-TEM image of a Ag/ZnO back reflector deposited on c-Si substrate.

It appears that the ZnO layer has a strong (002) preferential orientation and Ag layer with (111) preferential orientation (Fig.17 (b)). We have estimated the grain size from the full width at the half maximum of the XRD peaks and found that the calculated grain sizes are in the range of 17-25 nm without a clear trend in film thickness. The Ag/ZnO structures were also characterized with X-TEM analysis. Figure 18 shows an X-TEM of Ag/ZnO layers deposited on c-Si. The image shows that the ZnO grain sizes are much larger than estimated from XRD. There are two possible explanations of the different grain sizes measured by XRD and X-TEM. First, it could be that the XRD peak width is not determined by the grain size but something else such as the stress in the films. Second, the large grains appeared in the X-TEM images contain many small grains as measured by XRD. From the X-TEM image, one can see that the ZnO crystals have a columnar structure with the vertical grain size similar to the film thickness and the lateral size ranging up to 0.3 μm . The lateral grain size determines the texture of the ZnO surface as seen by the Pt cap layer.

The Ag/ZnO back reflectors were also measured using AFM for surface roughness analysis. Figure 19 plots the AFM images of two samples. The top and bottom images were taken from R2040 and R2141. The two samples were deposited under the same conditions except the ZnO layer thickness is 0.6 μm in R2040 and 1.8 μm in R2141. From the AFM images, one can see that both the vertical roughness and the lateral sizes of the features are much larger in the thicker sample than the thinner one. Figure 20 plots the RMS roughness versus the ZnO thickness. For the series of samples with flat Ag, the RMS roughness linearly increases with ZnO thickness from 0.5 to 2 μm and then levels off. The RMS roughness of the samples on textured Ag shows an initial roughness from the textured Ag layer, increases in the range up to 2.0 μm , and levels off for samples with even thicker ZnO layer. The samples with ZnO

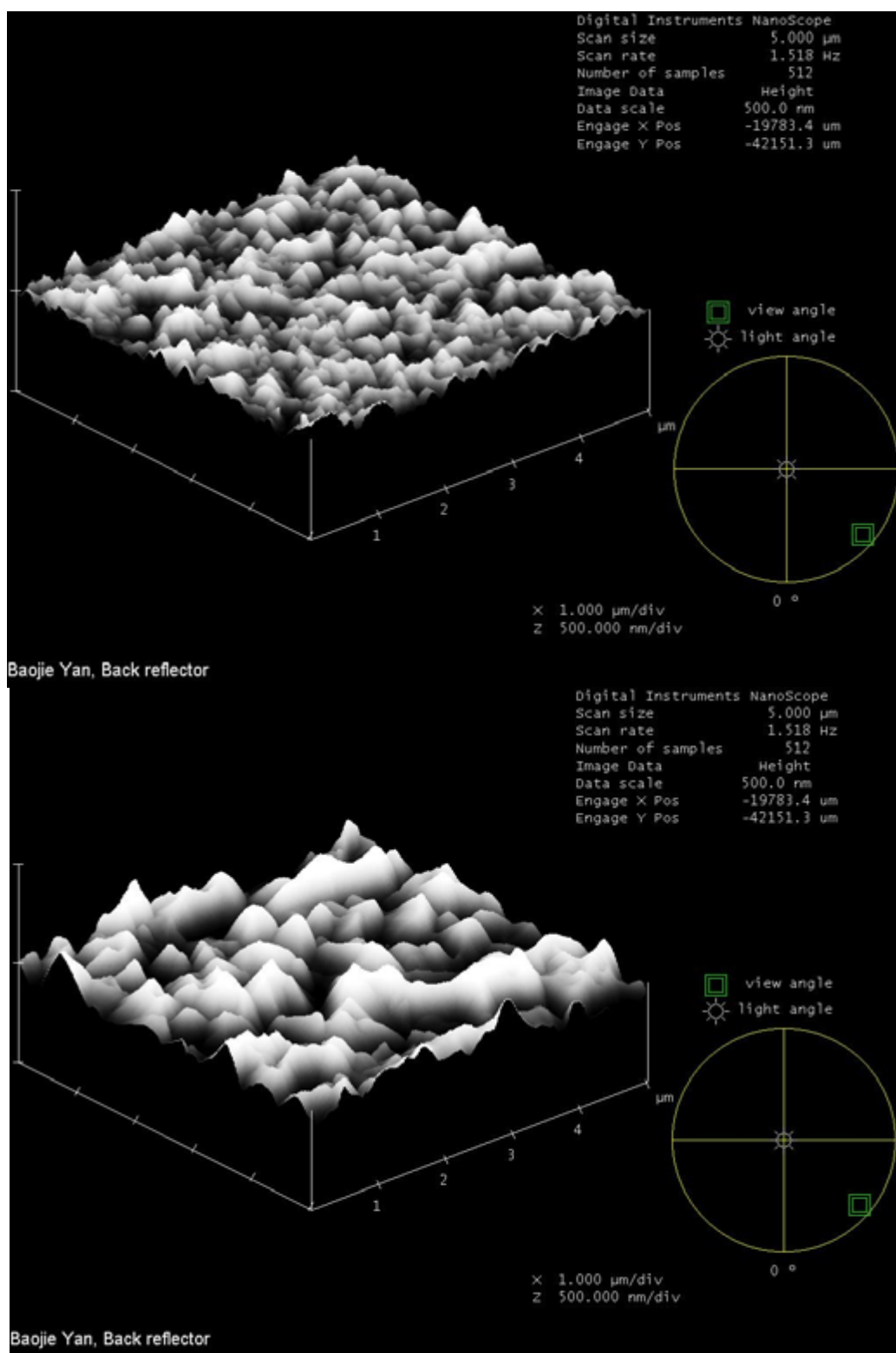


Figure 19. AFM images of Ag/ZnO back reflectors. The top image was taken from R2040 and the bottom one from R2141. The sample properties are listed in Table III.

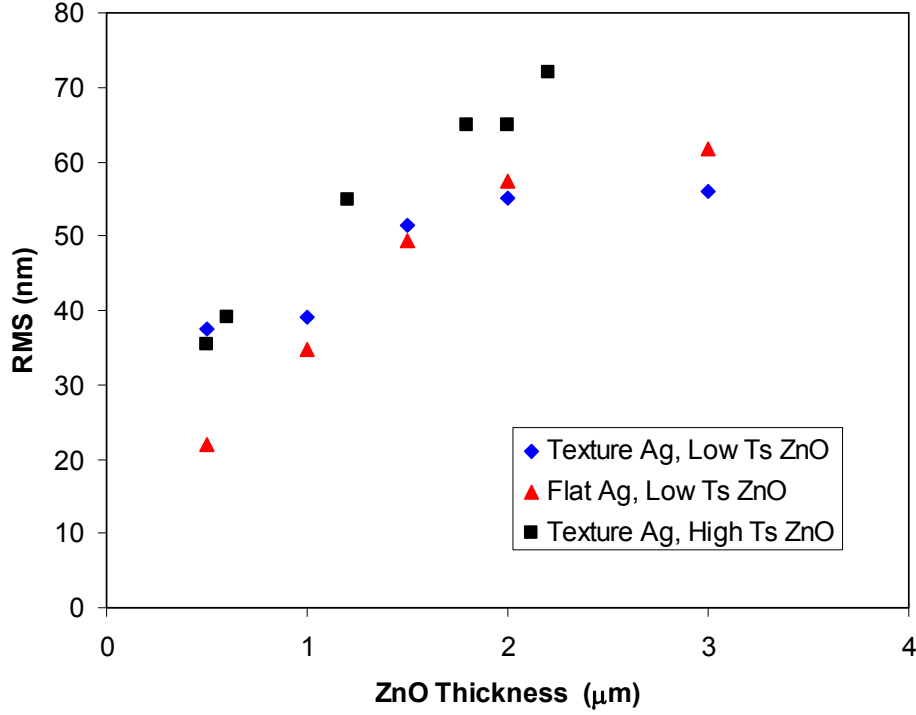


Figure 20. RMS roughness as a function of ZnO layer thickness in Ag/ZnO back reflectors.

deposited at a high temperature show more texture than the low temperature ones. If the RMS roughness is a critical parameter for light trapping in solar cells, a 2-μm-thick ZnO is probably the optimal thickness for the back reflectors.

The RMS roughness only shows the vertical changes of the surface morphology. However, the lateral scale of the textured features is also important for light trapping in solar cells. There are two methods for the lateral size representation. The first is the autocovariance function, which is calculated by the following equation,

$$c(x, y) = \langle [h(x, y)h(x + \Delta x, y + \Delta y)] \rangle, \quad (2)$$

where $h(x, y)$ is the surface height at position (x, y) and $\langle \rangle$ means an average over the entire surface for Δx and Δy . The mathematical definition of the correlation length is the distance over which the correlation function along a given direction decreases by a factor of $1/e=0.37$. The important parameter is the minimum correlation length, which is the minimum value of the correlation length in all the directions. The minimum correlation length represents the lateral feature size on a rough surface. Figure 21 plots the minimum correlation length as a function of ZnO layer thickness. It shows that the lateral size increases with the ZnO thickness. The initial lateral size is smaller on the samples with a flat Ag layer than with a textured Ag layer because the textured Ag also contributes to the feature size. The lateral size continually increases with the ZnO layer thickness without the tendency of saturation as shown in the RMS plots in Fig. 20.

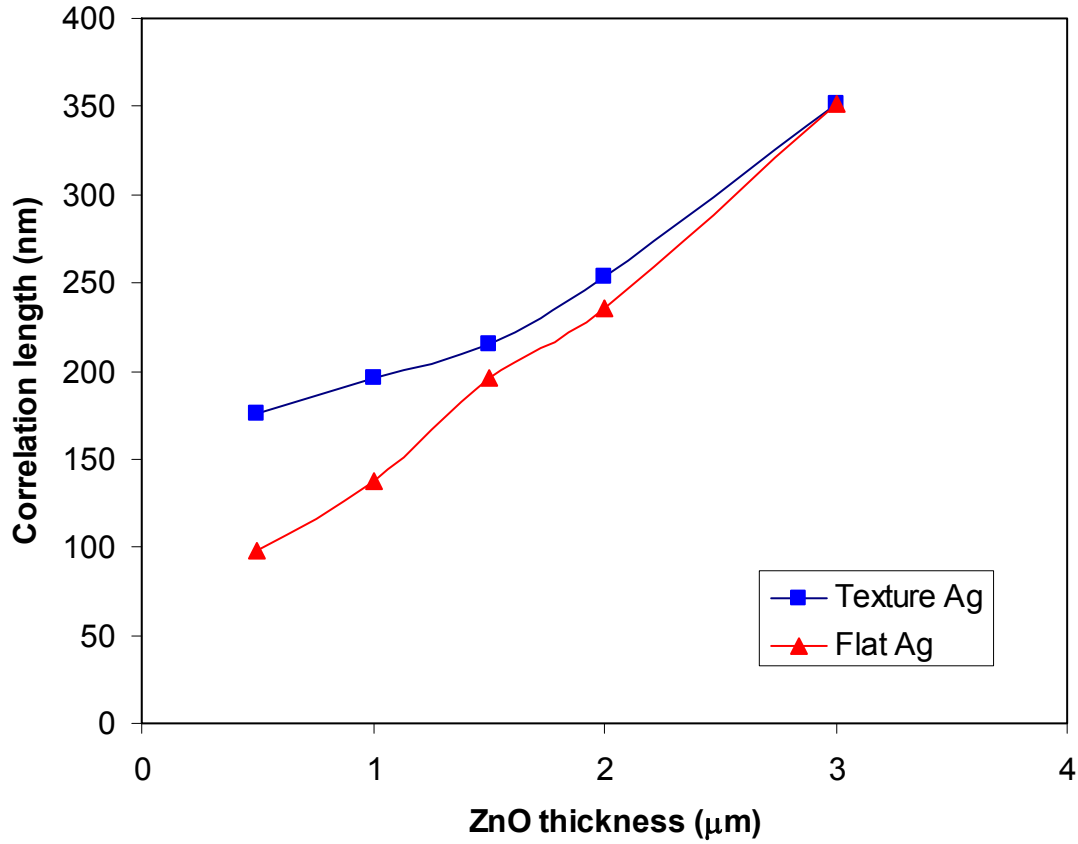


Figure 21. Minimum correlation length of Ag/ZnO back reflector versus the thickness of the ZnO layer.

To summarize the observations, we found that both the vertical and lateral sizes of micro-features on the Ag/ZnO back reflectors increases with the ZnO thickness. The vertical roughness saturates when the ZnO thickness is over 2 μm , but the lateral size does not show the saturation trend. It may imply that the slope of the micro-features decreases with the ZnO thickness. The X-TEM image shows that the ZnO grain size is much larger than estimated from XRD spectrum, indicating the XRD peak is not determined by the grain size, but something else such as the stress in the film; or the large grains contain many nanometer sized grains similar as observed in nc-Si:H films.

3.3.2. a-SiGe:H solar cells on improved Ag/ZnO back reflectors

In this project, we first optimized a-SiGe:H bottom cells on SS substrates. Table IV lists the J-V characteristics of a-SiGe:H bottom cells on SS substrates. Normally we characterize a-SiGe:H bottom cells using both the AM1.5 and red lights. For a-SiGe:H bottom cells on SS, a 530-nm long pass filter is used. A benchmark of P_{max} under the red light illumination is 4 mW/cm^2 . Although the cell performance has not reached the best results achieved previously [39], the cells showed very good performances. We also listed the FF measured under weak blue and red lights from a white light source through narrow band pass filters. The blue light provides information for the region near the *i/p* interface, while the red light measures the quality of the

Table IV. Typical J-V characteristics of a-SiGe:H bottom cells on stainless steel substrates, where the data were measured under AM1.5 illumination and with a 530-nm long-pass filter. The J_{sc} data were calculated from convoluting the QE curves with the AM1.5 spectrum. The FF values under the blue and red lights were measured under narrow band pass filters.

Sample #	Light source	P_{max} (mW/cm ²)	J_{sc} (mA/cm ²)	V_{oc} (V)	FF		
					AM1.5	Blue	Red
16332	>530 nm	4.42	10.81	0.662	0.618		
	AM1.5	7.08	16.71	0.679	0.624	0.694	0.635
16337	>530 nm	4.46	11.11	0.662	0.607		
	AM1.5	6.98	16.88	0.677	0.611	0.699	0.640
16388	>530 nm	4.45	11.06	0.665	0.601		
	AM1.5	6.88	16.75	0.680	0.604	0.682	0.624
16339	>530 nm	4.40	10.48	0.660	0.636		
	AM1.5	6.53	16.12	0.675	0.600	0.701	0.665
16366	>530 nm	4.52	10.90	0.666	0.622		
	AM1.5	7.23	16.90	0.682	0.627	0.692	0.640

intrinsic layer. It appears that the red FF is much lower than the blue FF, indicating that the material quality in the intrinsic layer needs to be improved further. In addition, a proper Ge profiling may also improve the cell performance further.

We used the recipe of a-SiGe:H bottom cells on SS to start optimizing cells on Ag/ZnO back reflectors. Table V lists the J-V characteristics of a-SiGe:H bottom cells made with the same recipe as Sample 16332. The first two samples in Table V serve as baseline samples. The Ag/ZnO back reflector from a roll-to-roll machine was used for Sample 16387. Then, we compared the cell performance for the cells on Ag/ZnO back reflectors with flat and textured Ag layers. First, a pair of cells (16382 and 16380) on the Ag/ZnO back reflectors with a thinner ZnO showed that the textured Ag layer produces a much higher J_{sc} than the flat Ag layer, especially for the long wavelength region. However, when a thick ZnO layer was used, the Ag/ZnO with the flat Ag layer produced a similar or slightly higher J_{sc} than the textured Ag layer.

In order to investigate the optical loss mechanisms of a-SiGe:H bottom cells on various Ag/ZnO back reflectors, we measured the total reflection of the substrates using an integrating sphere. Figure 22 (a) shows the total reflection spectra of various substrates. First, the SS has a relatively flat reflection spectrum with a reflectivity ranging from 0.5-0.6, which slightly increases with the increase of wavelength. The Ag/ZnO back reflectors show a large reflection minimum in the short wavelength region around 350-400 nm, which has been identified as the plasmon absorption at the Ag/ZnO interface. It appears that the flat Ag results in a higher reflection than the textured Ag layer, presumably caused by the reduced plasmon absorption. The enhanced reflection by the flat Ag is observed in both cases with thinner and thicker ZnO layers. In addition to the loss by plasmon absorption, the absorption in the ZnO layer also plays a significant role, especially in the long wavelength region. The lower reflectivity of the Ag/ZnO back reflectors with thicker ZnO could be mainly caused by the extra absorption of ZnO. Figure 22 (b) plots the average reflections in the short (300-650 nm), long (650-1000 nm)

and entire (300-1000 nm) wavelength regions. On average, the thinner ZnO layer results in higher reflection in the whole wavelength region.

The light trapping effect not only depends on the total reflection from the back reflector, but also on the scattering at the semiconductor/dielectric interface as well as the dielectric/metal interface. From Table V, one can see that the cells on the Ag/ZnO back reflectors with a thinner ZnO layer showed lower J_{sc} , especially for the one with a flat Ag layer. It is clear that for the Ag/ZnO back reflector with a thin ZnO layer, the texture of the Ag layer is very important because it provides the effect of scattering. Figure 23 (a) compares the quantum efficiency and reflection curves of the two cells on Ag/ZnO back reflectors with the thinner ZnO layer. The long wavelength reflection is much higher from the cell with a flat Ag layer than from the one with a textured Ag layer. Correspondingly, the long wavelength quantum efficiency is lower in the cell with a flat Ag layer than that with a textured Ag layer.

Table V. J-V data of a-SiGe:H bottom cells made with the same recipe as in Sample 16332 but on flat stainless steel and different Ag/ZnO back reflectors. The long wavelength performance was measured with a 530-nm long pass filter for the cells on stainless steel substrates and with a 630-nm long pass filter for the cells on Ag/ZnO back reflectors.

Run #	Light	J_{sc} (mA/cm ²)	V_{oc} (V)	FF	P_{max} (mW/cm ²)	Substrate	Comment
16332	AM1.5	16.71	0.679	0.624	7.08	SS	Flat
	>530 nm	10.81	0.662	0.618	4.42		
16366	AM1.5	16.91	0.682	0.627	7.23	SS	Flat
	>530 nm	10.90	0.666	0.627	4.52		
16387	AM1.5	22.81	0.680	0.599	9.29	Ag/ZnO 5BR2040	Textured Ag 0.6 μ m ZnO
	>630 nm	10.58	0.646	0.601	4.11		
16382	AM1.5	21.01	0.662	0.585	8.14	Ag/ZnO R8568	Flat Ag 0.5 μ m ZnO
	>630 nm	9.01	0.624	0.585	3.29		
16380	AM1.5	22.61	0.672	0.562	8.54	Ag/ZnO R8567	Textured Ag 0.5 μ m ZnO
	>630 nm	10.35	0.638	0.569	3.76		
16402	AM1.5	23.78	0.689	0.610	9.99	Ag/ZnO R8578	Flat Ag 2.0 μ m ZnO
	>630 nm	11.24	0.661	0.619	4.60		
16413	AM1.5	23.53	0.686	0.617	9.96	Ag/ZnO R8578	Flat Ag 2.0 μ m ZnO
	>630 nm	10.94	0.655	0.613	4.39		
16357	AM1.5	23.33	0.699	0.619	10.09	Ag/ZnO R8483	Textured Ag 2.0 μ m ZnO
	>630 nm	10.89	0.667	0.619	4.50		
16364	AM1.5	23.55	0.696	0.597	9.79	Ag/ZnO R8562	Textured Ag 2.0 μ m ZnO
	>630 nm	11.01	0.665	0.602	4.41		

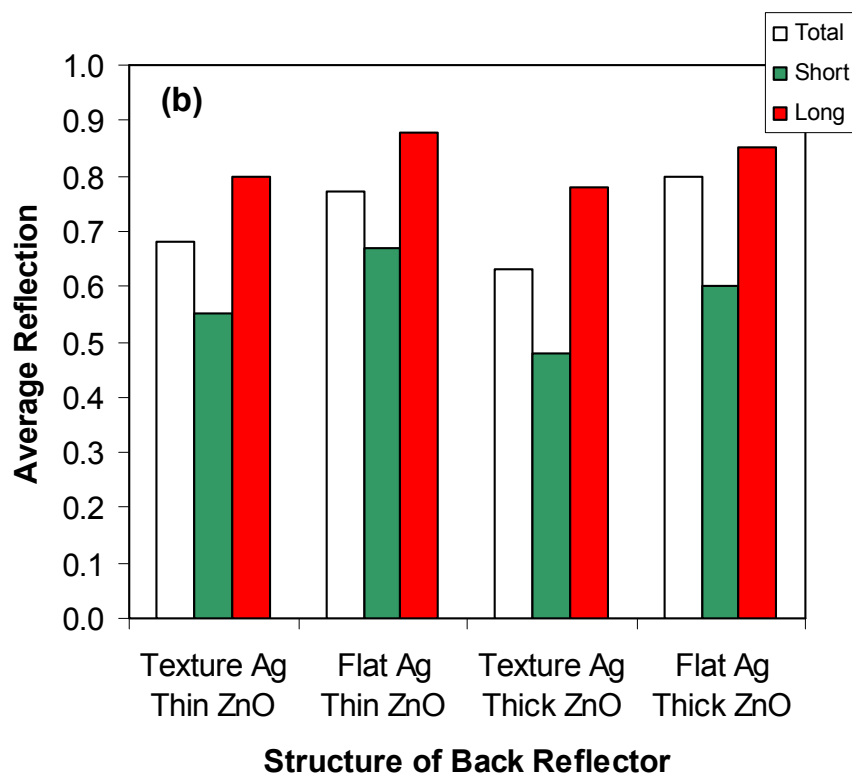
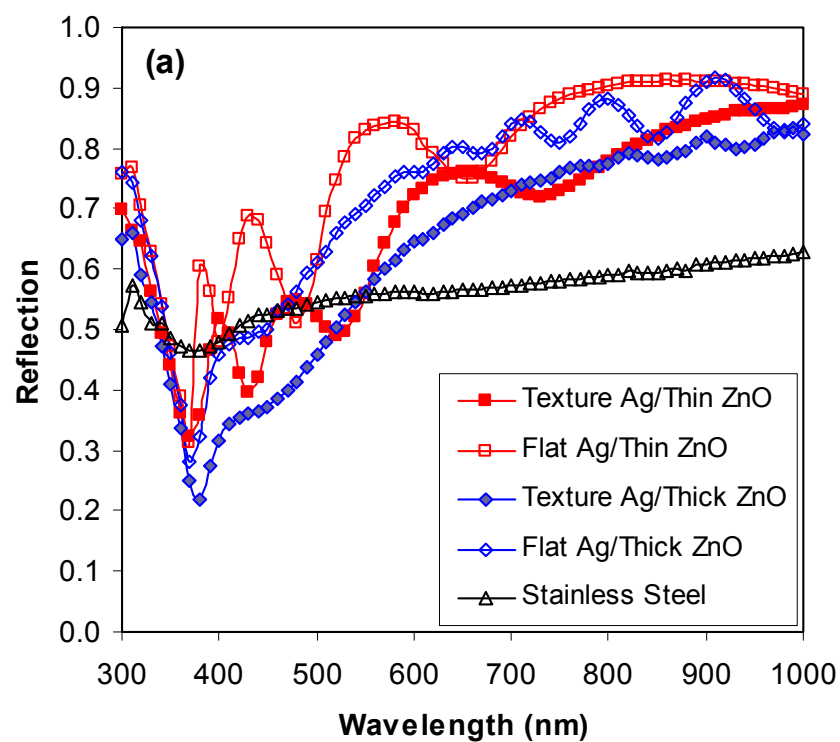


Figure 22. (a) Total reflection spectra of stainless steel and various Ag/ZnO back reflectors; (b) the average reflection for various spectrum regions.

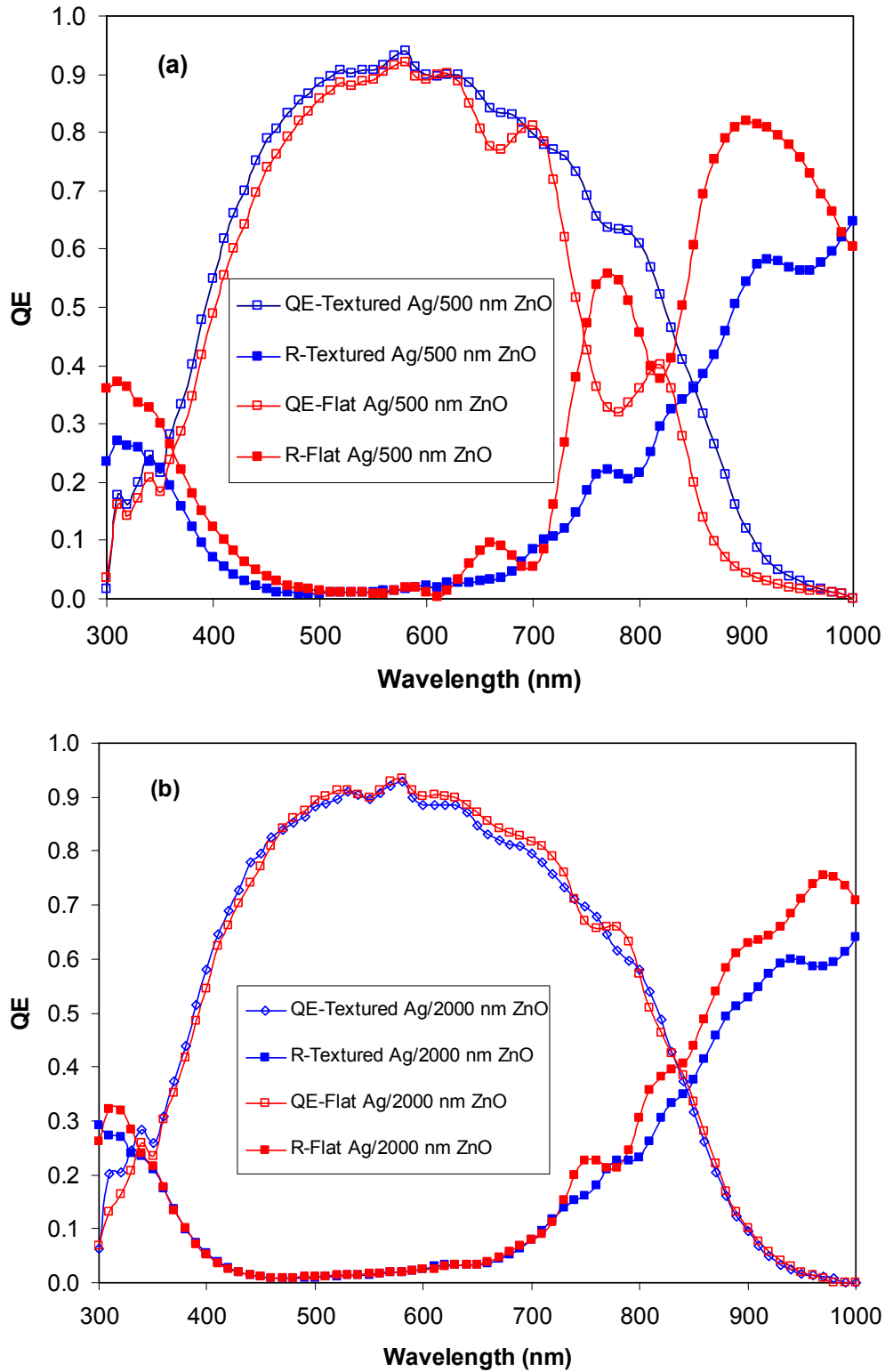


Figure 23. (a) A comparison of QE and R curves of a-SiGe:H solar cells on Ag/ZnO with textured Ag and flat Ag layers and with a 500-nm thick ZnO; (b) the same comparison except the ZnO layer is 2000-nm thick.

The comparison of the cells on Ag/ZnO with thicker ZnO layers reveals a different picture. From Table V, one can see that the flat Ag layer produces a J_{sc} similar to (or slightly higher than) the cells on Ag/ZnO back reflector with the textured Ag layer; even though the scattering from the back reflector with the textured Ag layer is as high as indicated by the suppressed interference fringes in Fig. 22 (a). Figure 23 (b) shows the comparisons of the quantum efficiency and reflection curves of a-SiGe:H cells on Ag/ZnO back reflectors with either flat Ag or textured Ag layer, where the ZnO thickness is 2.0 μm . The QE curves are very similar except for clear interference fringes in the sample with flat Ag, indicating lower scattering with the flat Ag layer. The reflection curves still show that the cell with the flat Ag layer has high reflection in the long wavelength region. For the samples with the thick ZnO, the flat Ag has a lower absorption loss in the metal/dielectric interface, but the scattering is also lower. On the other hand, the textured Ag layer provides higher scattering, but the absorption is higher than the samples with a flat Ag layer.

To summarize the quantum efficiency and reflection results, we make the following observations. First, for Ag/ZnO back reflectors with a thinner ZnO, the textured Ag is definitely a necessary component for providing sufficient light scattering. Second, for the Ag/ZnO back reflectors with a thicker ZnO layer, the quantum efficiency is similar for the samples with flat Ag and textured Ag layers. The flat Ag layer reduces the plasmon absorption in the metal/dielectric interface, but does not provide as high light scattering as obtained from the textured Ag layer. Third, a thicker ZnO also improves the V_{oc} slightly, which could be due to the reduction of the density of sharp features on the ZnO surface as measured by AFM microscopic images [36]. Overall, the long wavelength (>630 nm) P_{max} has been improved from 3.8 mW/cm^2 to 4.6 mW/cm^2 when the Ag/ZnO is changed from flat Ag and thin ZnO to flat Ag and thick ZnO layers. The trend is clear that a flat Ag layer with a thicker ZnO having sufficient texture is the most desirable structure for high efficiency solar cells.

3.3.3. Calculation of optical enhancement in a-SiGe:H cells on Ag/ZnO back reflector

In order to obtain the optical enhancement factor, we have to establish a baseline for reference. Thin film solar cells on flat stainless steel substrates should be good baselines. Therefore, the optical enhancement obtained in this way is the effective increase of the absorption length for reaching the quantum efficiency ratio of solar cells deposited on back reflectors over stainless steel substrates at different wavelengths. The procedure includes a comparison of the quantum efficiency curves of a-SiGe:H single-junction solar cells made with the same recipe on bare stainless steel substrates and Ag/ZnO back reflectors. A mathematical calculation procedure is proposed with certain assumptions.

First, we calculate the quantum efficiency as a function of the absorption coefficient and cell thickness. Assume $N_0(\lambda)$ of photons with wavelength λ get into the solar cell. The absorption coefficient for this wavelength is α . When we assume the generation rate is 100%, the density of electron/hole pairs generated at the position of x is,

$$N(x, \lambda) = N_0(\lambda) \exp(-\alpha x). \quad (3)$$

The amount of electron/hole pairs (photons absorbed) generated between x and $x+dx$ is,

$$dN(x, \lambda) = \alpha N_0 \exp(-\alpha x) dx. \quad (4)$$

For the cells on stainless steel substrates, we assume that the light reaches the substrates and reflects back with a reflection coefficient R . We also assume that the reflected light will come out of the cell when it reaches the top surface, which means there are only two paths (one can consider more paths with a high order polynomial approach). In this case, we integrate eq.(4) over the intrinsic layer thickness L for the direct incident beam and the reflection beam and obtain,

$$N(\lambda) = N_0 \int_0^L \alpha \exp(-\alpha x) dx + R N_0 \exp(-\alpha L) \int_L^0 \alpha \exp(-\alpha(L-x)) dx. \quad (5)$$

$$N(\lambda) = N_0 [(1 - \exp(-\alpha L))(1 + R(\exp(-\alpha L)))]. \quad (6)$$

We assume that there is no recombination loss, which means every photon-generated electron/hole pair is collected and contributes to the quantum efficiency (Q_{ss}) measurements. In this case, the Q_{ss} is the ratio of absorbed photons to total incident photons. Then, we obtain,

$$R[\exp(-\alpha L)]^2 + (1 - R)\exp(-\alpha L) + (Q_{ss} - 1) = 0, \quad (7)$$

From the positive solution of this quadratic equation, we obtain,

$$\alpha L = -\ln \left\{ \frac{\sqrt{(1-R)^2 + 4R(1-Q_{ss})} + (R-1)}{2R} \right\}. \quad (8)$$

In the case of solar cells on a textured back reflector, we assume the reflection coefficient at the surface of BR is one hundred percent, and the reflection at the top surface is also one hundred percent (total reflection). Although these assumptions are not realistic, the losses at the interface (by absorption in the interface or escaping out at the top surface) are considered as the reduction of the effective paths of the trapped light. Therefore, the estimated optical enhancement is the lowest limitation. With these assumptions, we define an effective enhanced absorption length kL , where k is the optical enhancement factor. Based on this definition, we have,

$$N(\lambda) = N_0 \int_0^{kL} \alpha \exp(-\alpha x) dx = N_0 [1 - \exp(-\alpha kL)]. \quad (9)$$

Defining the quantum efficiency Q_{BR} of the cell on BR as $N(\lambda)/N_0$, then we have,

$$Q_{BR} = 1 - \exp(-\alpha kL), \quad (10)$$

and,

$$k = -\frac{\ln(1 - Q_{BR})}{\alpha L}, \quad (11)$$

where αL is obtained from eq.(6) with the Q_{SS} data. As pointed out, the problem is oversimplified by the assumptions. In reality, there are always some optical losses at the metal/dielectric interface and top surface as well as in the doped layers. In addition, electrical loss by recombination in the intrinsic layers is also a factor for the accuracy of the estimation. Therefore, the estimation by this method gives the lowest limit of the optical enhancement as pointed above. In order to reduce the recombination losses, Q_{SS} and Q_{BR} data under a reverse bias should be used. The comparison to the calculation based on the Q_{SS} and Q_{BR} data under the short-circuit condition will provide the errors caused by the recombination process in the intrinsic layer.

We have done some calculations of the optical enhancement factor k for a-SiGe:H single-junction solar cells. Figure 24 (a) shows a comparison of QE curves of a-SiGe:H single-junction solar cells made with the same recipe on a flat stainless steel substrate and a Ag/ZnO back reflector. The ratio of the two quantum efficiency curves is also plotted on the same figure. It is clear that the optical enhancement is mainly in the long wavelength region, because in the short wavelength region, the absorption coefficients are large enough to absorb the light within one path through the thickness of the intrinsic layer. Figure 24 (b) shows the calculated optical enhancement factor k using the procedure presented above, where two reflectivity R values at the semiconductor/stainless-steel were used. Normally, we use $R=0.2$ for the SS/a-Si:H interface. With this value, one can see that the maximum optical enhancement factor is about 25. The estimated optical enhancement factor strongly depends on the R value. If $R=0.5$ is used, the maximum optical enhancement factor can be as high as 30. In addition, the wavelength dependence of R is also a consideration for further improvement in the calculation accuracy. Figure 25 shows a similar calculation for a nc-Si:H single-junction solar cells. The optical enhancement was calculated using $R=0.2$. The result shows that the optical enhance for this nc-Si:H is not as high as that shown in Fig. 24, which is partially due to the flatter back reflector as indicated by the interference fringes.

3. 4. Summary

We have systematically studied the material structures of Ag/ZnO using XRD, AFM, and X-TEM at NREL. The microscopic characterizations provided an important guideline for the optimization of back reflectors. We correlated the material structure of back reflector to the optical properties. Then, we optimized the Ag/ZnO back reflectors to have a high light trapping effect. We found that for Ag/ZnO back reflectors with a thinner ZnO layer, a textured Ag layer results in a higher short-circuit current density even if the plasmon absorption at the metal/dielectric interface is high for the textured Ag layer. The textured Ag provides high light scattering, which is the dominant factor for the back reflector with a thinner ZnO layer. For thick ZnO, the flat and textured Ag layers showed a similar short circuit current density because with the increase of the ZnO thickness, the scattering by the textured ZnO is increased. At the same time, the absorption at the metal/dielectric interface is lower. In order to increase the short circuit current density further, we shall increase the texture at the ZnO/semiconductor interface.

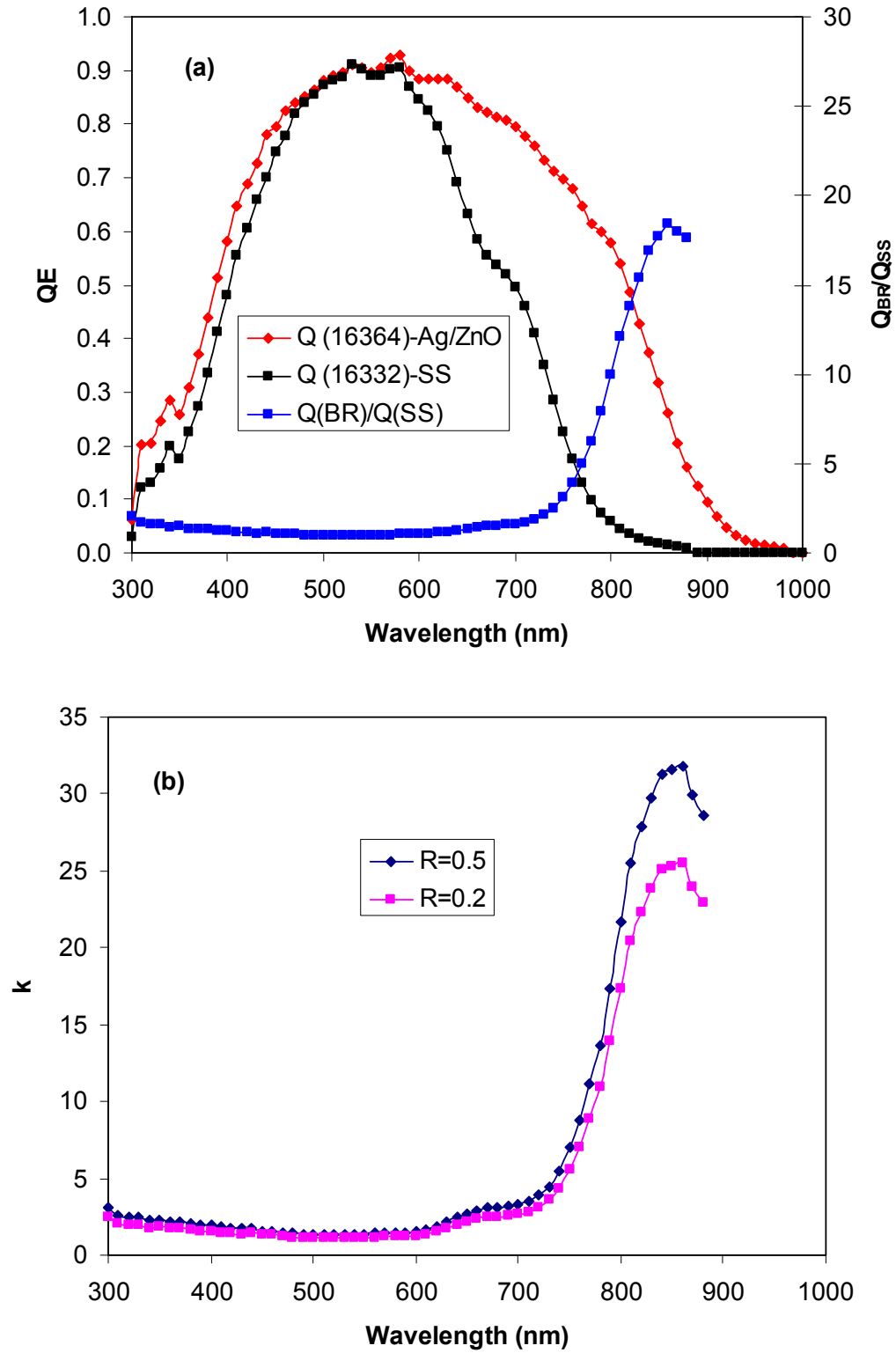


Figure 24. (a) Comparison of QE curves of a-SiGe:H single-junction cells deposited with the same recipe on a flat stainless steel substrate and a Ag/ZnO back reflector substrate; (b) the optical enhancement calculated using the procedure described in the text.

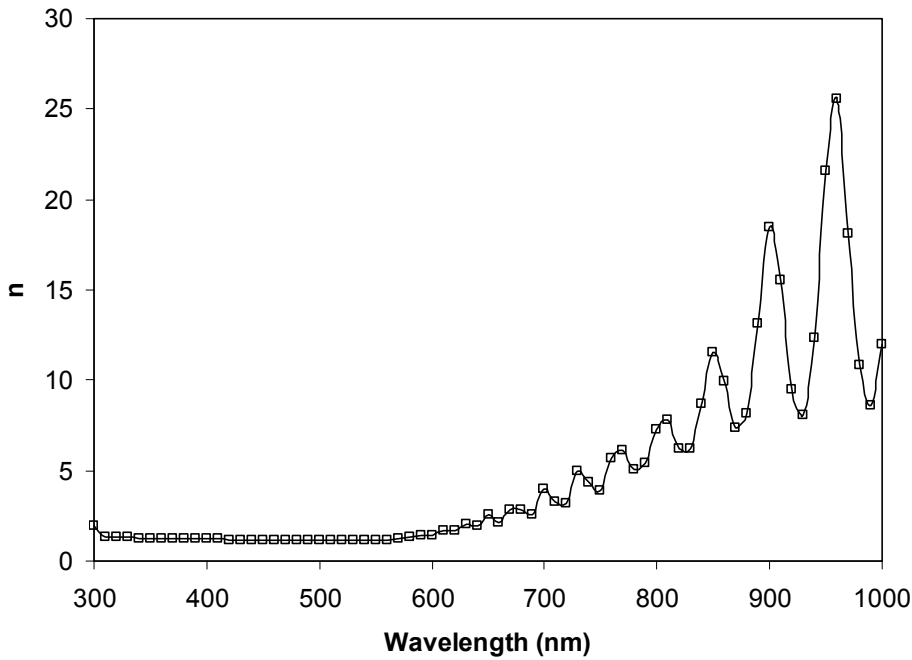
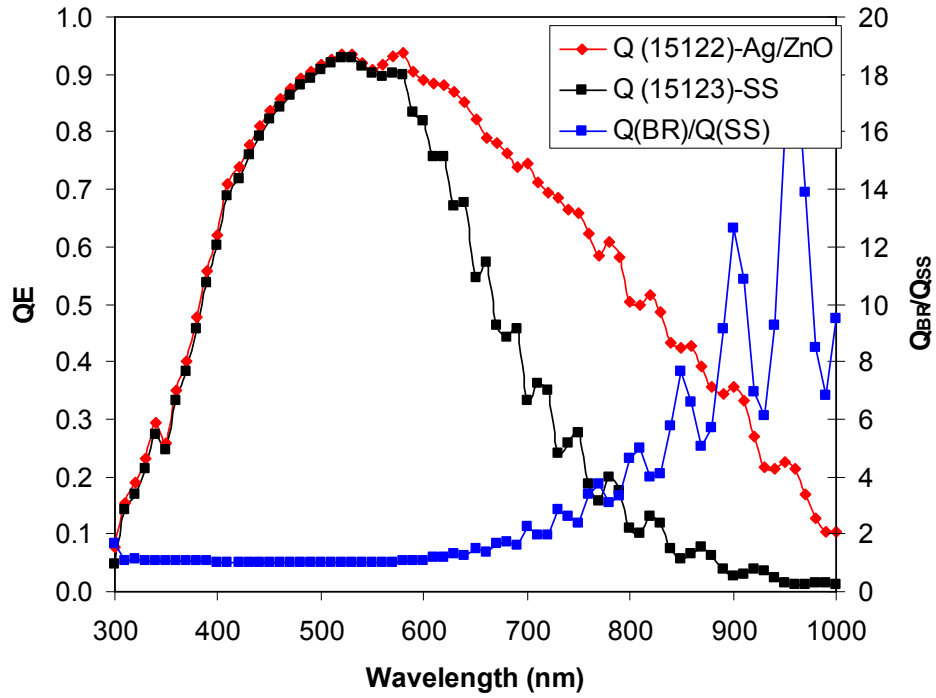


Figure 25. The upper plot shows the comparison of QE curves of nc-Si:H single-junction cells deposited with the same recipe but on a flat stainless steel substrate and a textured Ag/ZnO back reflector substrate. The lower plot shows the optical enhancement calculated using the procedure described in the previous section, where the reflection coefficient of $R=0.2$ was used in the calculation.

4. High efficiency a-Si:H/a-SiGe:H/nc-Si:H and a-Si:H/nc-Si:H/nc-Si:H triple-junction solar cells

4. 1. Introduction

We have achieved 15.1% [40] initial active-area efficiency and a stable active-area efficiency of 13.0% [35] using a-Si:H/a-SiGe:H/nc-Si:H triple-junction solar cells. In order to show that using nc-Si:H as the intrinsic layer in the bottom cell of multi-junction solar cells will improve the solar module efficiency, one has to demonstrate that the small area solar cells with nc-Si:H bottom cell have a high stable cell efficiency than the conventional a-Si:H/a-SiGe:H/a-SiGe:H triple-junction structure. We have reported an initial active-area efficiency of 15.1% using an a-Si:H/a-SiGe:H/nc-Si:H triple-junction structure [41], where the nc-Si:H bottom cell was made using MVHF at a high rate and the a-Si:H top and a-SiGe:H middle cells were made using RF glow discharge at low rates. In this project, we continued to optimize all the elements for the triple-junction structure for the highest achievable efficiency. The work covers the optimization of the component cells and Ag/ZnO back reflectors. Combining the optimized components, we have attained a new record initial active-area efficiency of 15.4%.

4. 2. Experimental details

We first optimized the component cells. The a-Si:H top cells were deposited with RF glow discharge at a low rate of $\sim 1 \text{ \AA/s}$ on bare stainless steel substrates. The intrinsic layer and the doped layers were optimized under the guideline of producing a J_{sc} around 9 to 9.5 mA/cm² for current matching in a-Si:H/a-SiGe:H/nc-Si:H triple-junction structures. The a-SiGe:H middle cells were deposited in the same RF system on Ag/ZnO back reflectors. Optimizations were carried out mainly for the intrinsic layer. Various parameters were optimized such as bandgap profiles, pressure, and hydrogen dilution. The nc-Si:H bottom cells were deposited using MVHF at a high rate of $\sim 5 \text{ \AA/s}$ on Ag/ZnO back reflector coated stainless steel substrates. Major optimization efforts were focused on the hydrogen dilution profiling as discussed in the previous section. High efficiency a-Si:H/a-SiGe:H/nc-Si:H triple-junction solar cells were made by combining the optimized component cells and taking care of the tunnel junctions. The solar cells were measured under an AM1.5 solar simulator with quantum efficiency (QE) calibration for the J_{sc} . The a-SiGe:H middle cells were also measured under the AM1.5 solar simulator with a 610-nm long-pass filter for simulating the situation in the triple-junction structure.

4. 3. Results and discussion

4.3.1. a-Si:H top cell

We first increased the hydrogen dilution to reach the amorphous to nanocrystalline transition regime. As previously reported, the geometry of the cathode design causes a non-uniform distribution of crystallinity over the substrate area [14, 15]. It was observed that in the amorphous to nanocrystalline transition regime, the nanocrystalline formation appears at the corners or edge first, while the center area exhibits more amorphous component. We used this phenomenon to monitor the phase transition. Table VI lists two sets of a-Si:H top cells made in the transition region. The first three samples were made with a constant hydrogen dilution ratio.

Table VI. J-V characteristics of a-Si:H top cells made with flat hydrogen dilution and profiled hydrogen dilution.

Sample No	Position	Eff (%)	J_{sc} (mA/cm ²)	V_{oc} (V)	FF	Comments
16341	Center	6.75	9.34	1.036	0.697	Constant H dilution Baseline
	Middle	6.57	9.55	1.030	0.667	
	Edge	4.12	9.04	0.786	0.580	
16345	Center	6.28	7.97	1.043	0.757	Constant H dilution with thin i-layer
	Middle	6.19	7.98	1.042	0.745	
	Edge	5.61	8.14	0.995	0.693	
16346	Center	5.94	7.77	1.049	0.729	Constant H dilution with thin i-layer and low T_s
	Middle	5.94	7.79	1.047	0.729	
	Edge	5.40	7.46	1.036	0.698	
16140	Center	7.30	9.92	1.034	0.712	Profiled H dilution Baseline
	Middle	7.12	9.92	1.031	0.692	
	Edge	5.48	9.68	0.880	0.644	
16343	Center	6.25	8.34	1.027	0.730	Profiled H dilution with thin i-layer
	Middle	6.31	8.48	1.030	0.723	
	Edge	5.53	8.36	0.964	0.686	
16344	Center	6.26	7.92	1.055	0.748	Profiled H dilution with thin i-layer and low T_s
	Middle	5.90	7.60	1.048	0.740	
	Edge	4.2	7.32	0.916	0.626	

Sample 16341 is a baseline cell, which showed a V_{oc} of 1.036 V in the center, indicating good a-Si:H properties. However, at the edge, the V_{oc} drops to 0.786 V, resulting from the mixed-phase formation. Sample 16345 was made under the same condition as Sample 16341 except for a thinner intrinsic layer. The reduced intrinsic layer thicknesses resulted in an V_{oc} increase to 1.043 V at the center and 0.995 at the edge, as expected from typical observations. This also confirms the nanocrystalline evolution with the thickness, especially at the edge. At the same time, the FF is also improved. Sample 16346 was made under the same condition as Sample 16345 except the substrate temperature (T_s) was reduced by 25 °C. As expected, the lower substrate temperature results in an even higher V_{oc} but smaller J_{sc} .

The lower three samples in Table VI were made with a hydrogen dilution profiling, where the hydrogen flow rate was linearly decreased with time. The average hydrogen dilution of this set was about 10% lower than the first set. When the same average dilution ratio was used, the cells made with hydrogen dilution profiling became mixed-phased solar cells, indicating that a very high hydrogen dilution at the initial stage of deposition could produce a nc-Si:H seed layer for subsequent deposition. Therefore, the average hydrogen dilution has to be reduced when a hydrogen dilution profiling is used for a-Si:H deposition. Sample 16140 was a baseline cell made with hydrogen dilution profiling, which performs better than Sample 16341 made with constant hydrogen dilution. Reducing the thickness of the intrinsic layer by simply reducing the deposition time with the same ratio of hydrogen profiling did not increase the V_{oc} as observed in the samples with the constant hydrogen dilution ratio. An explanation could be that

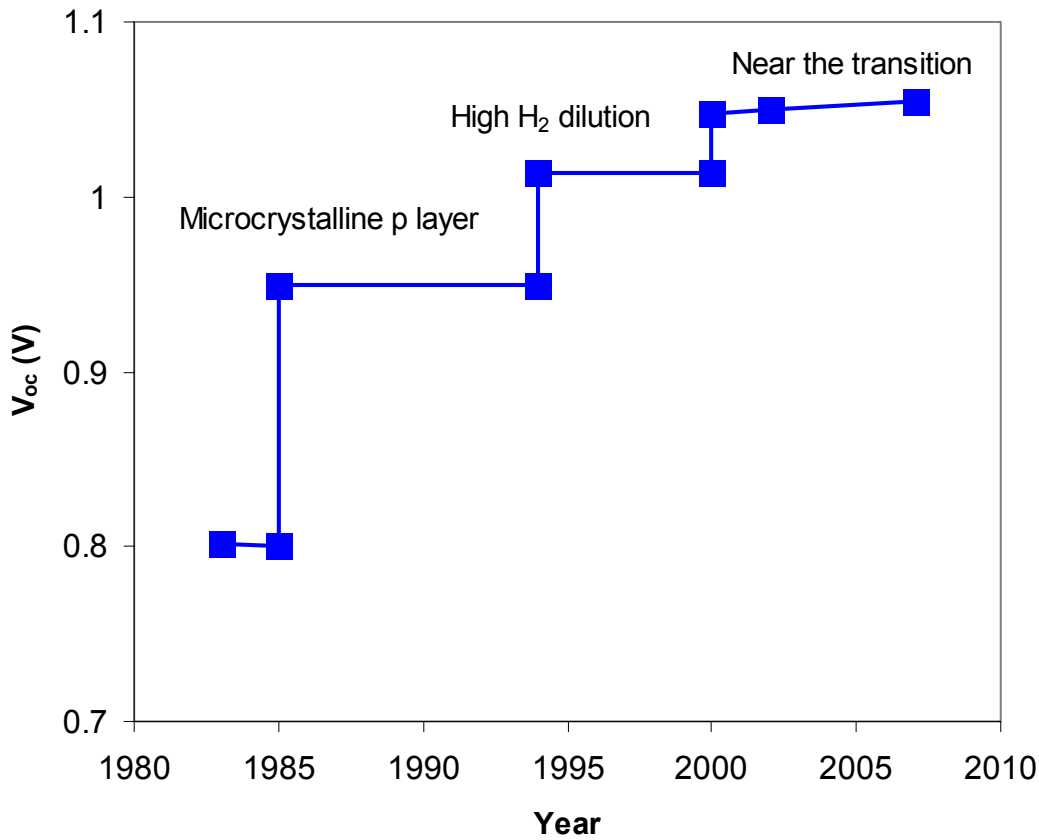


Figure 26. United Solar’s historical improvements in open-circuit voltage in a-Si:H solar cells when different technologies were invented and used.

the initial hydrogen dilution was too high in the profiled sample and the initial growth has more effect for the thinner samples than for the thicker samples. By reducing the substrate temperature, the V_{oc} is improved dramatically, and an initial V_{oc} of 1.055 V was achieved, which is the highest value achieved in our laboratory. Figure 26 shows the historical evolution of V_{oc} when different processing techniques were used. Normally, it is believed that the V_{oc} is limited by the properties of the intrinsic layer and the quality of interfaces, especially the *i/p* interface. The upper limit of V_{oc} is the built-in potential, which is around 1.1-1.2 V. Although we may still have room for further improvement, the new record has approached the built-in potential.

4.3.2. a-SiGe:H middle cell

United Solar has extensive experience in the optimization of a-Si:H and a-SiGe:H component cells for a-Si:H/a-SiGe:H/a-SiGe:H triple-junction structures [36,40]. Compared to the component cells used in the conventional a-Si:H/a-SiGe:H/a-SiGe:H triple-junction structure, the a-Si:H top and a-SiGe:H middle cells used in the a-Si:H/a-SiGe:H/nc-Si:H structure should have higher current to match the nc-Si:H bottom cell. Currently, our nc-Si:H single-junction cells on Ag/ZnO show J_{sc} around 27-28 mA/cm². Optimizing a-SiGe:H middle cells to have a high current is more difficult than a-Si:H top cells. In general, the defect density is higher in a-SiGe:H than in a-Si:H. In the specific design of an a-SiGe:H middle cell in the a-Si:H/a-

SiGe:H/nc-Si:H triple-junction, the relatively higher J_{sc} makes the cell design more difficult because we have to increase the J_{sc} with minimum loss in the V_{oc} and FF. Table VII lists the J-V characteristics of a few a-SiGe:H middle cells during different stages of the optimization. We started from a baseline cell (16109) with $P_{max} \sim 4 \text{ mW/cm}^2$ and $J_{sc} \sim 8.9 \text{ mA/cm}^2$ under an AM1.5 solar simulator with a 610-nm long-pass filter. We have optimized the GeH_4 and Si_2H_6 flow rates (cell 16112) and profiles and improved the long wavelength J_{sc} to $\sim 9.5 \text{ mA/cm}^2$, but lost 10 mV in V_{oc} . We further changed the deposition pressure. Although we gained long wavelength current, we lost another $\sim 10 \text{ mV}$ in V_{oc} . By optimizing the hydrogen dilution (16130), we increased the J_{sc} , V_{oc} , and FF at the same time. Furthermore, in using the optimized Ag/ZnO back reflector as described in the last quarterly report, we increased the long wavelength J_{sc} to $\sim 10.9 \text{ mA/cm}^2$ and the long wavelength P_{max} to $\sim 5 \text{ mW/cm}^2$, which are good numbers for a-SiGe:H middle cells.

4.3.3. nc-Si:H bottom cell

The key contribution for high efficiency a-Si:H/a-SiGe:H/nc-Si:H triple-junction solar cells is a high performance nc-Si:H bottom cell. We have put significant effort into the optimization of nc-Si:H single-junction solar cells. The major improvement is the quality of the nc-Si:H material. The defect density has been reduced remarkably as measured by David Cohen's group [28]. In addition, careful control of the microstructure along the growth direction [23] is important as discussed in the previous section. We also used the optimized Ag/ZnO back reflectors developed in the last quarter.

The most important technique of improving nc-Si:H solar cell efficiency is to control the nanocrystalline evolution along the growth direction [23]. In section 2, we showed the material structure as a function of hydrogen dilution profiling. In order to achieve high efficiency, we need not only the optimized nc-Si:H material, but also an optimized the device structure in nc-Si:H solar cells, mainly the interface control.

We previously reported [42] that as the intrinsic layer thickness increases, V_{oc} drops more significantly in nc-Si:H cells than in a-Si:H cells. We attributed this to the fact that the crystalline volume fraction increases with increasing thickness. We also found that the nc-Si:H cell performance strongly depends on the *i/p* buffer layer [42]. Without a proper buffer layer, the nc-Si:H cell shows a poorer FF and a smaller V_{oc} , which, in turn, leads to low conversion efficiency. Recently, we found that the metastable behavior after prolonged light soaking in nc-Si:H solar cells is different from a-Si:H cells in many cases. Although this is mainly caused by the difference in the intrinsic material properties, the interface also has certain potential influence on the metastability. In this project, we carried out a systematic study of the effects of the intrinsic and *i/p* buffer layer thicknesses on nc-Si:H cell performance and stability. To avoid the microstructure evolution with thickness as mentioned before, the hydrogen dilution profiling technique [23] has been used so that the intrinsic layers in all the cells maintain similar crystalline volume fraction along the growth direction. The results show that both the cell performance and the stability are related to the intrinsic and *i/p* buffer layer thicknesses.

nc-Si:H *n-i-p* single-junction solar cells were deposited using a multi-chamber glow discharge system with RF chambers for the doped layers and a MVHF chamber for the intrinsic layers at a deposition rate of $\sim 3\text{-}5 \text{ \AA/s}$. The same hydrogen dilution profile was used for all the

Table VII. Typical J-V characteristics of a-SiGe:H middle cells on Ag/ZnO back reflector for a-Si:H/a-SiGe:H/nc-Si:H triple-junction structures.

Sample No.	Light	J_{sc} (mA/cm ²)	V_{oc} (V)	FF	P_{max} (mW/cm ²)	Comment
16109	AM1.5	19.94	0.775	0.597	9.23	Previous baseline
	>610 nm	8.85	0.743	0.613	4.03	
16112	AM1.5	20.52	0.761	0.608	9.45	Optimization of GeH ₄ flow rate
	>610 nm	9.46	0.731	0.598	4.14	
16116	AM1.5	20.84	0.753	0.606	9.51	Optimization of pressure
	>610 nm	9.92	0.724	0.605	4.35	
16130	AM1.5	21.21	0.760	0.632	10.19	Optimization of H ₂ dilution
	>610 nm	10.18	0.730	0.637	4.73	
16138	AM1.5	21.82	0.766	0.635	10.61	Optimization of Ag/ZnO BR
	>610 nm	10.61	0.731	0.650	5.04	
16141	AM1.5	22.22	0.769	0.610	10.53	Optimization of Ag/ZnO BR
	>610	10.88	0.741	0.624	5.03	
16148	AM1.5	22.07	0.763	0.627	10.56	Optimization of Ag/ZnO BR
	>610 nm	10.92	0.735	0.629	5.05	

intrinsic layer depositions. The same *n/i* buffer and seeding layers were used for all the samples. The samples with different intrinsic layer thicknesses were made by controlling the intrinsic layer deposition time. The a-Si:H *i/p* buffers were made with RF glow discharge at a deposition rate of ~ 1 Å/s. For comparison, high rate a-Si:H cells with different intrinsic layer thicknesses were also made with MVHF at a deposition rate of ~ 6 Å/s. Both nc-Si:H and a-Si:H cells were deposited on Ag/ZnO coated stainless steel substrates. The material structure of the intrinsic layer was directly measured on the cells with no *i/p* buffer layer using Raman spectroscopy with a green light (532 nm) excitation. Light soaking was carried out under 100 mW/cm² of white light at 50 °C under the open circuit condition for 1000 hours. Dark J-V characteristics of the cells were measured in a vacuum chamber using a programmable multi-meter at a controlled temperature.

Table VIII lists the J-V characteristics of nine nc-Si:H single-junction solar cells with different intrinsic and *i/p* buffer layer thicknesses. The same hydrogen dilution profile was used for all the nc-Si:H intrinsic layer depositions. The different intrinsic layer thicknesses were obtained by controlling deposition time as listed in column two. For each intrinsic layer thickness, three different thicknesses of a-Si:H *i/p* buffers with the deposition times of 0, 3, and 7 minutes (corresponding to thicknesses of 0, 180, and 420 Å) were added to study the effect of buffer layer thickness. From Table VIII, the following observations are made. For the effect of the intrinsic layer thickness, we found that the FF decreases and the J_{sc} increases with increasing intrinsic layer thickness. The V_{oc} does not change much with intrinsic layer thickness for the cells with zero and 3-minute *i/p* buffer layers. However, for the cells with a 7-minute *i/p* buffer layer, the V_{oc} decreases noticeably with an increase in the intrinsic layer thickness. Also, the conversion efficiency increases with the intrinsic layer thickness. For the effect of the *i/p* buffer layer thickness, three points can be made. First, the V_{oc} increases with increasing *i/p* buffer layer thickness. Second, the FF does not improve by adding the *i/p* buffer layer. For the thin cells, the FF is even reduced. Third, the *i/p* buffer layer has a greater effect on the thin cells than the thick

ones. For example, when the *i/p* buffer layer thickness was increased from 0 to 7 minutes, the V_{oc} increased from 0.463 to 0.532 V for the cells with a 7-minute intrinsic layer, which is significantly larger than the increase from 0.455 to 0.483 V for the cells with a 30-minute intrinsic layer. This phenomenon is even more pronounced in the FF. For the cells with a 7-minute intrinsic layer, the FF is reduced from 0.714 to 0.677 when the *i/p* buffer layer is increased from 0 to 7 minutes. However, for the cells with a 30-minute intrinsic layer, the FF is not sensitive to the *i/p* buffer layer thickness.

As mentioned previously, to control the effect of microstructure evolution on the cell performance, we have used the hydrogen dilution profiling technique in the intrinsic layer deposition to keep the crystalline volume fraction constant in the material along the growth direction. To confirm this, Raman spectroscopy measurements were made on the cells with different intrinsic layer thicknesses by using the green laser (532 nm). In order to avoid the potential influence of the a-Si:H *i/p* buffer on measurement results, the cells with no *i/p* buffer layer (samples 14098, 14099, 14100) were selected for the Raman measurements. Figure 27 (a) shows the Raman spectra for the three samples. One can clearly see that the three cells have very similar crystalline volume fractions. For a detailed analysis, we deconvoluted the Raman spectra into three components of amorphous TO ($\sim 480 \text{ cm}^{-1}$), intermediate ($\sim 500 \text{ cm}^{-1}$), and crystalline ($\sim 520 \text{ cm}^{-1}$) modes using three Gaussian functions as shown in Fig. 10 (b). The results are summarized in Table IX. The crystalline volume fraction listed in the table is simply defined as the ratio of the areas of the crystalline and the intermediate modes to the total. The crystalline volume fractions for the cells with 7, 15, and 30 minutes of intrinsic layers are 46.6%, 56.8%, and 60.9%, respectively. We noted that the volume fraction in the thicker cell is still slightly higher than in the thinner one.

Dark J-V measurement is a useful tool in studying the recombination mechanism in a-Si:H based solar cells. An ideal solar cell follows the typical diode characteristics of $J=J_0[\exp(qV/nkT)-1]$, where J_0 is the reverse saturated current density, q the unit charge, T the measurement temperature, k the Boltzmann constant, and n the diode quality factor. By studying the dark J-V characteristics and examining the deviation of experimental results from the diode

Table VIII: J-V characteristics of nine nc-Si:H single-junction solar cells on Ag/ZnO substrate with different thicknesses of the intrinsic and *i/p* buffer layers.

Sample No.	Time (i) (min)	Time (i/p) (min)	V_{oc} (V)	FF	J_{sc} (mA/cm ²)	P_{max} (mW/cm ²)
14098	7	0	0.463	0.714	14.54	4.81
14099	15	0	0.455	0.641	18.71	5.46
14100	30	0	0.455	0.586	22.49	6.00
14101	7	3	0.481	0.700	14.18	4.77
14111	15	3	0.473	0.642	18.78	5.70
14112	30	3	0.473	0.590	22.87	6.38
14113	7	7	0.532	0.677	16.00	5.76
14114	15	7	0.491	0.622	19.73	6.03
14106	30	7	0.483	0.590	22.82	6.50

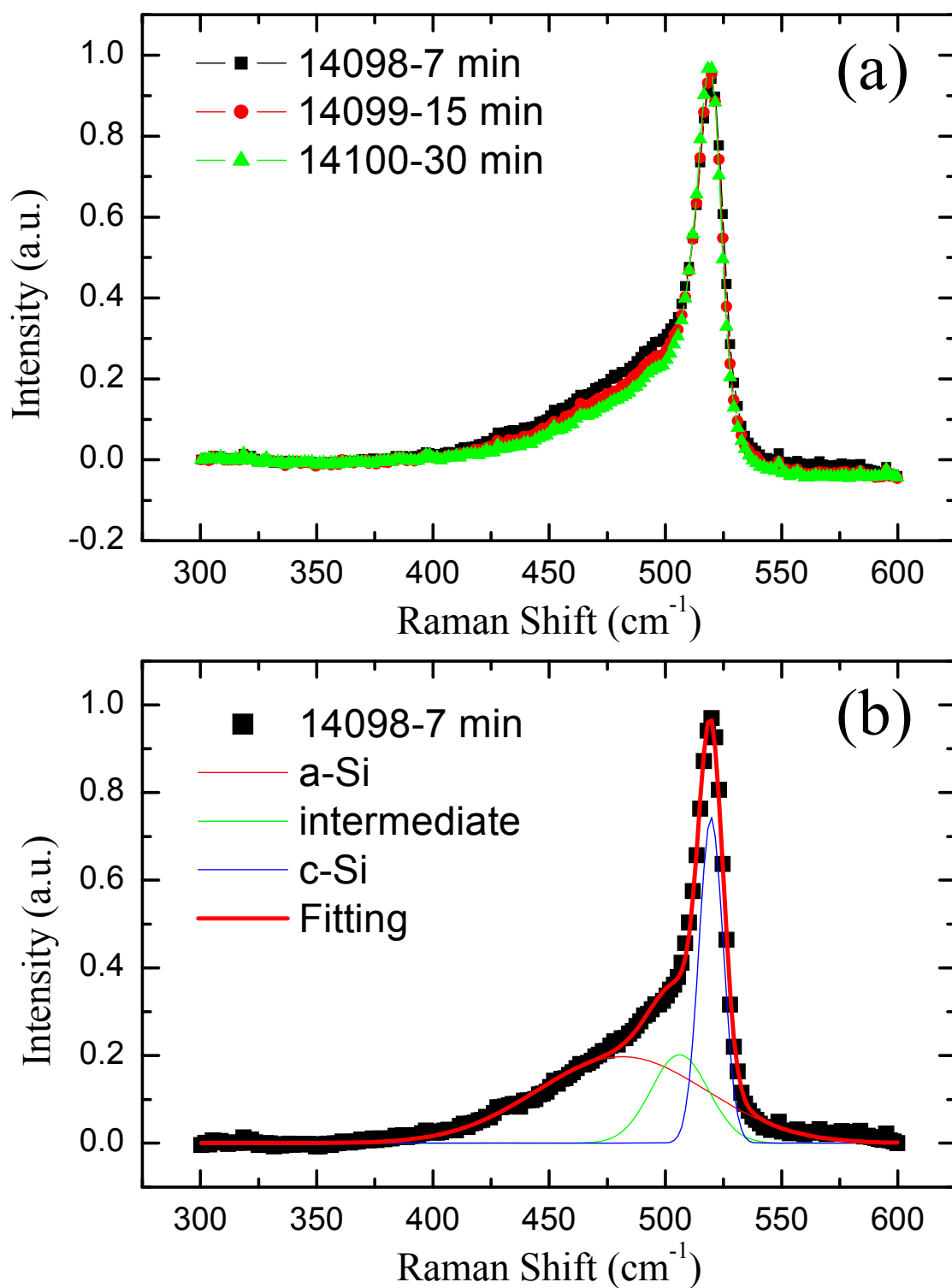


Figure 27. (a) Comparison of Raman spectra for the samples with different intrinsic thicknesses and with no *i/p* buffer, and (b) an example of a Raman spectrum deconvolution.

Table IX. Deconvolution results of the Raman spectra, where s, p, w, and f denote the area, peak position, width, and percentage of each component, respectively. R represents the ratio of the areas of the c-Si and intermediate peaks to the total areas of the three peaks.

Sample No.	amorphous				intermediate				crystalline				R (%)
	s _a	p _a	w _a	f _a (%)	s _i	p _i	w _i	f _i (%)	s _c	p _c	w _c	f _c (%)	
14098	18.1	481	86	53.4	6.2	505	29	18.3	9.6	520	11	28.3	46.6
14099	12.7	479	70	43.2	6.9	507	29	23.5	9.8	520	13	33.3	56.8
14100	10.8	478	69	39.1	6.8	507	29	24.6	10.0	520	13	36.3	60.9

characteristics, one can examine the shunt current and the recombination mechanism of the carriers in solar cells. In this study, we used the dark J-V measurement to study the nine nc-Si:H solar cells. The results are plotted in Fig. 28. One can see that the dark current density reduces with increased *i/p* buffer layer thickness. The cells with a thinner intrinsic layer show a larger reduction in the dark current density. Moreover, we found that the cells with no *i/p* buffer layer have a high shunt current density. When the *i/p* buffer layer thickness is increased, the shunt current density is continually reduced.

For the cells with a 7-minute *i/p* buffer, the shunt current density becomes minimized and the dark J-V curves basically follow the diode characteristics as shown in Fig. 28 (d). By fitting the data of these three samples with the diode characteristics, we obtained J_0 and n , as listed in Table X. One can see that the diode quality factors are very similar, which means that the carrier recombination mechanism is the same for the samples. The saturated current is increased by increasing the thickness of the intrinsic layer, indicating a greater recombination rate in the thicker samples. Previously, we found that the dark J-V characteristics of a-Si:H solar cells are largely independent of the intrinsic layer thickness. This phenomenon could be explained with a weak dependence of thickness on the recombination width, which is smaller than the intrinsic layer thickness. However, in the nc-Si:H solar cells, the dark J-V characteristics, especially the J_0 , strongly depend on the intrinsic layer thickness. A thicker intrinsic layer results in a larger J_0 , which could indicate that the recombination width is the same as the intrinsic layer thickness. A time-of-flight measurement found that the hole mobility in nc-Si:H is over one hundred times larger than in a-Si:H [43]. Correspondingly, the hole diffusion length in nc-Si:H solar cells is much larger than in a-Si:H solar cells and the improved hole diffusion length leads to a recombination width similar to the intrinsic layer thickness.

Table X. The dark J-V fitting results of three nc-Si:H cells with different intrinsic layer thicknesses. The *i/p* buffer layer is the same for the samples (7 minutes). J_0 denotes the reverse saturated current, and n the diode quality factor.

Sample No.	<i>i</i> layer deposition time	J_0 (A/cm ²)	n
14113	7 min	3×10^{-8}	1.75
14114	15 min	6×10^{-8}	1.67
14106	30 min	2×10^{-7}	1.70

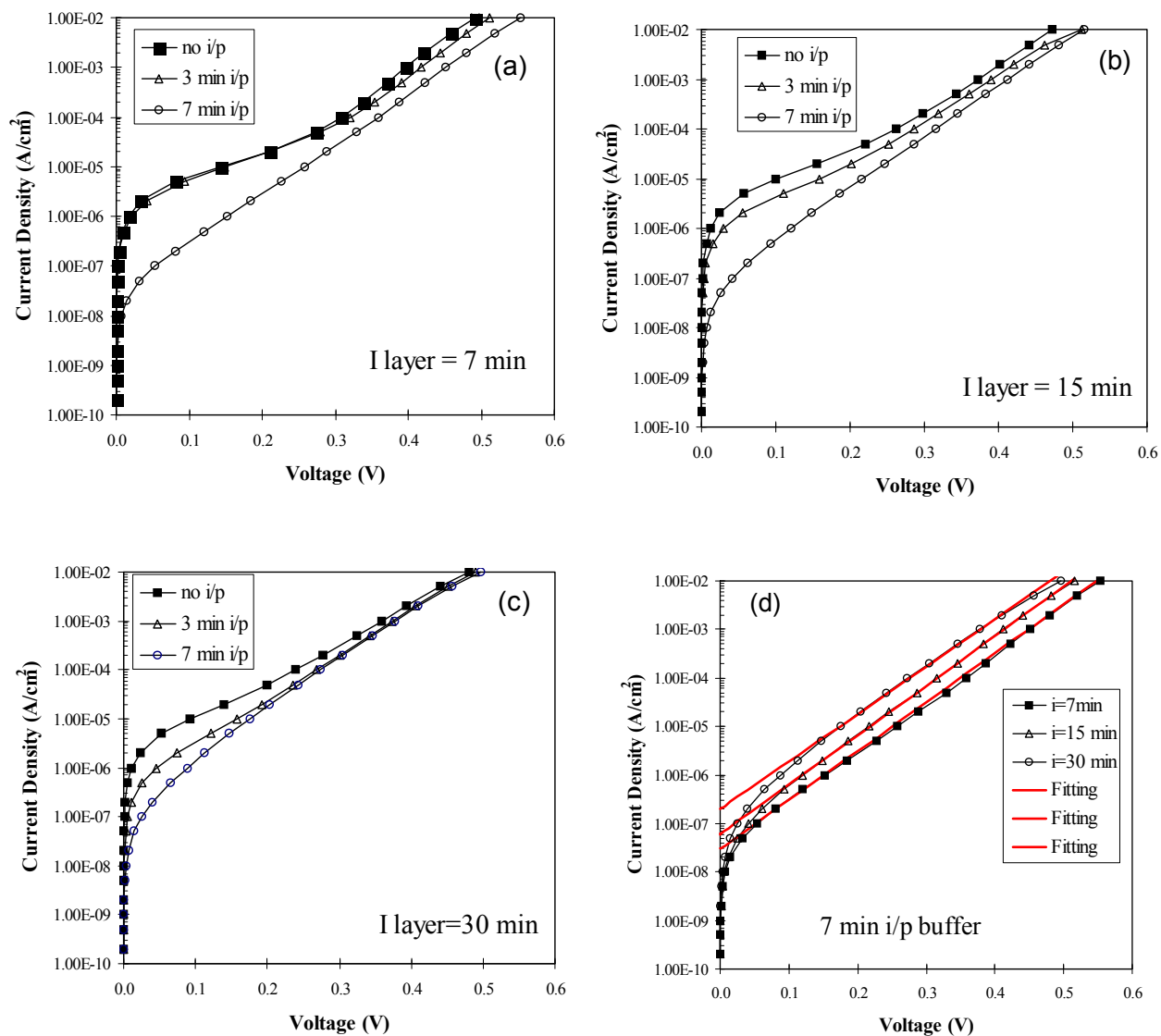


Figure 28. Dark J - V characteristics of the cells with (a) a 7-minute intrinsic layer but with different i/p buffer thicknesses; (b) a 15-minute intrinsic layer but with different i/p buffer layer thicknesses; (c) 30-minute intrinsic layer but with different i/p buffer thicknesses; (d) different intrinsic layer thicknesses but with the same i/p buffer layer thickness of 7 minutes.

We now discuss the main points obtained from the experimental results. First, we know that the FF usually decreases with an increase in the intrinsic layer thickness because of the reduction of built-in electric field and increased recombination rate. The intrinsic layer thickness dependence of FF in the nine samples follows this common trend. It is also understandable that the J_{sc} increases with increased intrinsic layer thickness since the light absorption is increased. Here, we need to point out that this is true for the cells with a certain thickness range. Beyond this range, other factors such as microstructure evolution, carrier collection length, or collapse of the built-in electric field, might play dominant roles. Compared to the FF and J_{sc} , the effect of intrinsic layer thickness on the V_{oc} is more complicated. Previously, we found that the V_{oc} decreases with increasing thickness more dramatically in nc-Si:H than in a-Si:H solar cells [43]. One explanation was the evolution of crystalline volume fraction with the intrinsic layer thickness. A similar trend is also observed in these nine samples as listed in Table XII. The reason for a small V_{oc} change with the intrinsic layer thickness for the cells with no or thin *i/p* buffer is probably due to the large shunt current density or a large recombination current density in the *i/p* interface. This is consistent with the results from the dark J-V measurements. With the increase of the *i/p* buffer layer thickness to 7 minutes, the shunt-current or interface recombination current was reduced, and the V_{oc} monotonically decreased with the intrinsic layer thickness. Moreover, from the Raman measurements, we noticed that the increase of crystalline volume fraction with the intrinsic layer thickness is small, which could not be the dominant factor for the reduced V_{oc} in the thicker cells made with hydrogen dilution profiling. Instead, the significantly increased dark current density could be the main reason for the reduced V_{oc} in the thicker cells. Second, we found that the V_{oc} increases with an increase in the *i/p* buffer layer thickness. This is because the a-Si:H *i/p* buffer layer reduces the shunt current density. This was confirmed by the dark J-V measurements as shown in Figure 28 (a), (b), and (c). We know that in the light J-V measurement, the V_{oc} is obtained when the dark current equals photo current. The larger the dark current is, the smaller the V_{oc} . We also found that the FF is not improved for these cells when the buffer layer was added. This is probably because the a-Si:H *i/p* buffer is too thick and introduces an extra series resistance. Another interesting observation is that the *i/p* buffer has a larger effect on the thin cells than thick ones. It may indicate that the cell performance of the thin samples was dominated by the *i/p* interface, while the performance of the thick samples was dominated by the bulk properties.

A stability study has been carried out on the nine nc-Si:H solar cells, and the results are listed in Table XI. As a comparison, four high rate a-Si:H solar cells with different intrinsic layer thicknesses were also studied, and the results are listed in Table XII. Three points have been observed from the tables. First, the light-induced degradation rate in nc-Si:H decreases with increasing intrinsic layer thickness. This is different from the case in a-Si:H based solar cells, where we usually found that the degradation rate increases with the intrinsic layer thickness. Second, adding an *i/p* buffer layer reduces the degradation rate, especially for the thin solar cells. For example, sample 14098 with no *i/p* buffer degrades ~14% in efficiency, whereas sample 14113 with a 7-minute *i/p* buffer layer degrades only ~2%. However, for the thick samples, the degradation rate does not change much when the *i/p* buffer layer is changed, which can be seen by comparing sample 14100 with no *i/p* buffer and sample 14106 with a 7-minute *i/p* buffer layer. To clearly see this trend, we plotted the degradation rate versus the intrinsic layer thickness in Fig. 12. Third, the degradation (if any) happens mostly in V_{oc} and FF. J_{sc} shows almost no degradation for all the samples.

As discussed above, the cell performance in thin cells is mainly dominated by the *i/p* interface. Since light soaking causes more damage in the *i/p* interface than in the bulk due to more exposure, the thin cells will be subjected to more degradation than the thick cells. Moreover, according to our experience, the V_{oc} and FF are more sensitive to the *i/p* interface than J_{sc} . Any change in the *i/p* interface will affect the V_{oc} and FF. This is in agreement with the observation in the third point. Improving the interface by adding high quality amorphous *i/p* buffer should also reduce the light-induced degradation in the *i/p* interface region. This explains the reduced light-induced degradation rate by adding an *i/p* buffer layer. Previously, it has been reported that the bulk properties are improved by using a hydrogen dilution profiling technique [23], but actually the main improvement occurs close to the *i/p* interface region due to decreased hydrogen dilution. Based on the same argument, it is not surprising that the thick cells with an optimized *i/p* buffer have a more stable performance.

Table XI. Stability results of nc-Si:H solar cells with different intrinsic and *i/p* buffer layer thicknesses.

Sample No.	Time (i) (min)	Time(i/p) (min)	Status	V_{oc} (V)	FF	Q (mA/cm ²)	P_{max} (mW/cm ²)
14098	7	0	Initial	0.463	0.714	14.54	4.81
			Stable	0.422	0.672	14.60	4.14
			Deg.(%)	-8.9%	-5.9%	0	-13.9%
14099	15	0	Initial	0.455	0.641	18.71	5.46
			Stable	0.433	0.641	18.90	5.25
			Deg.(%)	-4.8%	0	+1.0%	-4.0%
14100	30	0	Initial	0.455	0.586	22.49	6.00
			Stable	0.443	0.586	22.83	5.93
			Deg.(%)	-2.6%	0	+1.5%	-1.2%
14101	7	3	Initial	0.481	0.700	14.18	4.77
			Stable	0.462	0.673	14.57	4.53
			Deg.(%)	-4.0%	-3.9%	+2.8%	-5.0%
14111	15	3	Initial	0.473	0.642	18.78	5.70
			Stable	0.448	0.646	18.92	5.48
			Deg.(%)	-5.3%	+0.6%	+0.7%	-3.9%
14112	30	3	Initial	0.473	0.590	22.87	6.38
			Stable	0.459	0.597	22.91	6.28
			Deg.(%)	-3.0%	+1.2%	+0.2%	-1.6%
14113	7	7	Initial	0.532	0.677	16.00	5.76
			Stable	0.516	0.679	16.04	5.62
			Deg.(%)	-3.0%	0	0	-2.4%
14114	15	7	Initial	0.491	0.622	19.73	6.03
			Stable	0.492	0.646	19.51	6.20
			Deg.(%)	0	+3.9%	-1.1%	+2.8%
14106	30	7	Initial	0.483	0.590	22.82	6.50
			Stable	0.481	0.597	22.62	6.50
			Deg.(%)	0	+1.2%	-0.9%	0

Table XII. Stability results of high rate a-Si:H solar cells with different intrinsic layer thicknesses. The cells were deposited using MVHF on Ag/ZnO coated stainless steel substrates.

Sample No.	Status	Q (mA/cm ²)	V _{oc} (V)	FF	P _{max} (mW/cm ²)	Thickness (nm)
14672	Initial	9.12	1.021	0.755	7.03	104
	Stable	8.93	0.977	0.711	6.20	
	Deg.	2.1%	4.3%	5.8%	11.8%	
14671	Initial	11.11	0.987	0.744	8.16	156
	Stable	10.77	0.970	0.690	7.21	
	Deg.	3.1%	1.7%	7.3%	11.6%	
14673	Initial	12.87	0.999	0.716	9.21	235
	Stable	12.32	0.973	0.666	7.98	
	Deg.	4.3%	2.6%	7.0%	13.4%	
14674	Initial	13.77	1.001	0.690	9.51	307
	Stable	12.97	0.973	0.632	7.98	
	Deg.	5.8%	2.8%	8.4%	16.1%	

As previously discussed, high efficiency nc-Si:H solar cells also need optimized back reflectors. In Table VIII, we present a comparison of J-V characteristics of nc-Si:H single-junction cells deposited on regular Ag/ZnO back reflectors made from one of our roll-to-roll production machines and on the newly optimized Ag/ZnO back reflectors. The results show that the improved back reflectors consistently improve the J_{sc} by 0.5-1.0 mA/cm², mainly in the long wavelength response as shown in Fig. 29. By combining the optimized nc-Si:H recipe and the optimized Ag/ZnO back reflector, we have attained a new high efficiency for a nc-Si:H single-junction solar cell. Figure 30 shows the J-V characteristics and quantum efficiency of the best nc-Si:H single-junction solar cell, which has an initial active-area efficiency of 9.23%. We have used this optimized nc-Si:H single-junction solar cell in triple-junction structures to achieve the highest efficiency.

Table VIII. Comparison of J-V characteristics of nc-Si:H solar cells deposited on regular Ag/ZnO back reflectors obtained from our manufacturing machine and on newly optimized Ag/ZnO back reflectors.

Run No.	BR	J _{sc} (mA/cm ²)	V _{oc} (V)	FF	Eff (%)
15397	Improved	26.21	0.524	0.620	8.52
15392	Regular	25.24	0.526	0.630	8.36
15425	Improved	26.11	0.516	0.629	8.47
15426	Regular	25.13	0.513	0.614	7.92
15437	Improved	27.17	0.507	0.598	8.21
15438	Regular	26.34	0.517	0.617	8.32

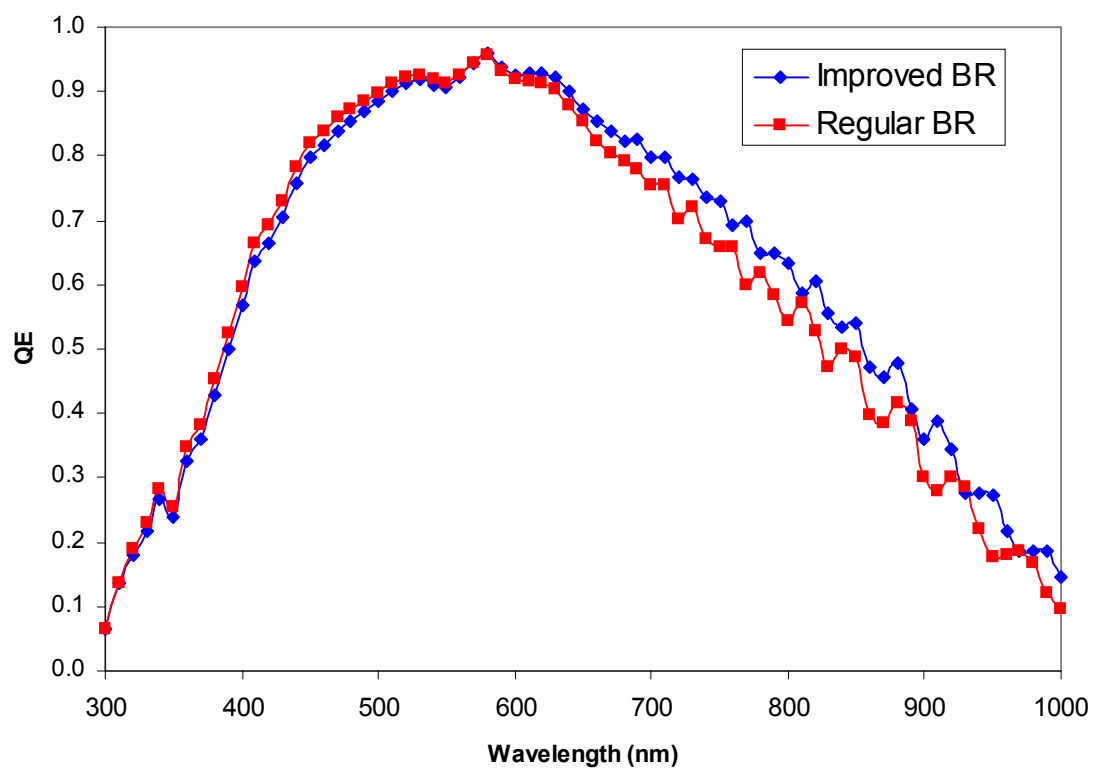


Figure 29. Comparison of quantum efficiency curves of two nc-Si:H single-junction cells deposited using the same recipe but on different Ag/ZnO back reflectors.

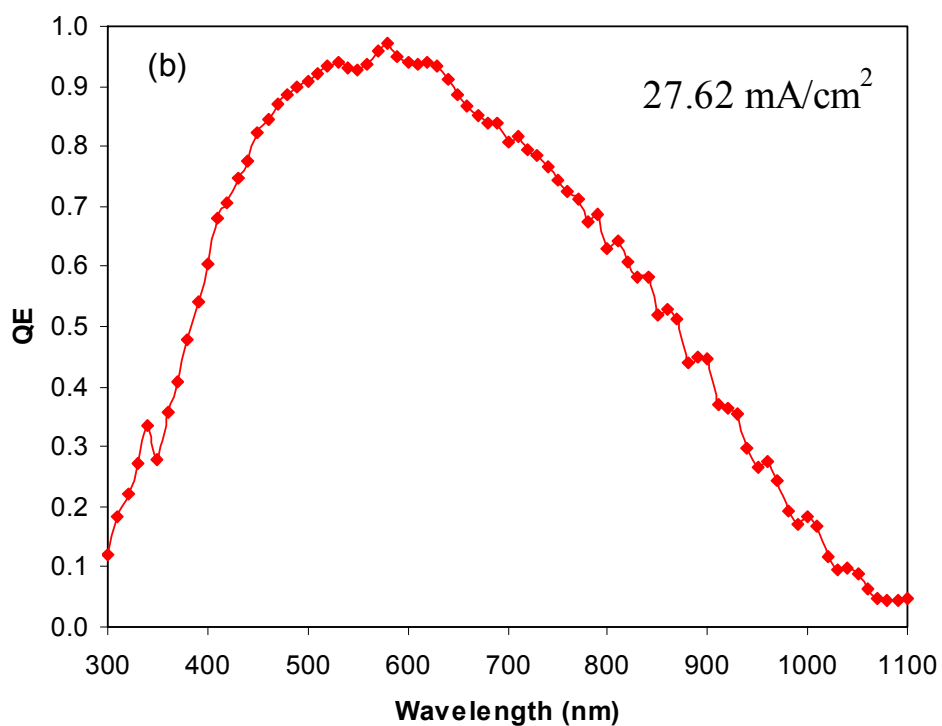
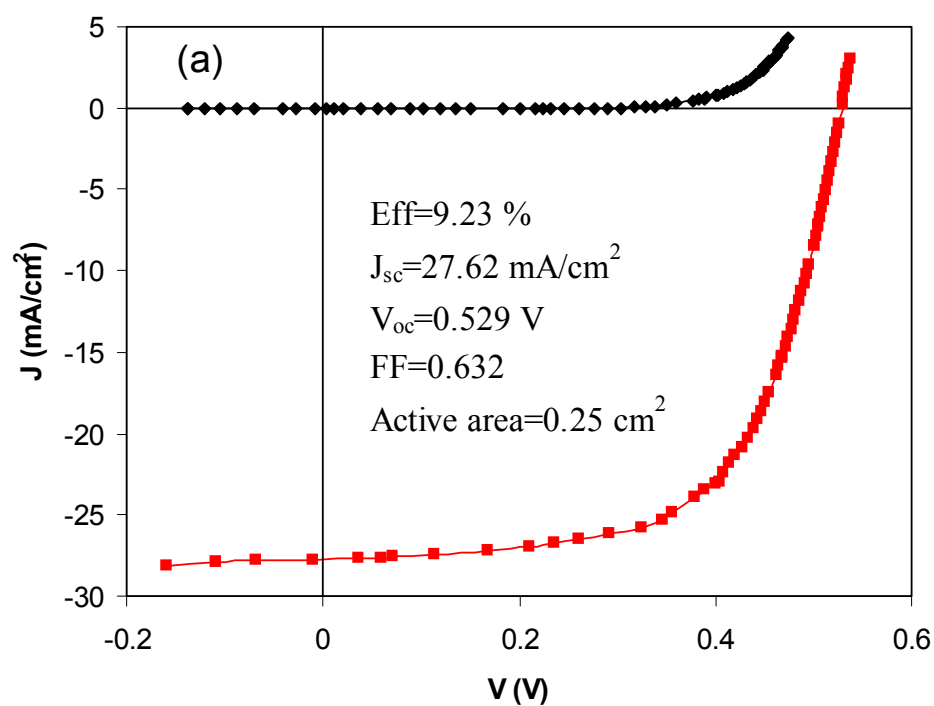


Figure 30. (a) J-V characteristics and (b) quantum efficiency curve of a nc-Si:H single-junction cell with an initial active-area efficiency of 9.23%.

4.3.4. Optimization of a-Si:H/a-SiGe:H/nc-Si:H Triple-junction design

It is well known that the good quality of materials is a necessary but not sufficient condition for achieving high efficiency solar cells. An optimized device design is also very important for achieving high solar cell efficiency, especially for multi-junction solar cells. First, multi-junction solar cells need optimized tunnel junctions between the component cells. Second, the current mismatch between the component cells is also an important factor for high efficiency, especially for stable efficiency. In this project, we systematically studied the correlation between the current mismatch and solar cell efficiency of a-Si:H/a-SiGe:H/nc-Si:H triple-junction solar cells.

We combine the J-V characteristics of component cells to obtain the J-V characteristics of multi-junction solar cells. The procedure includes measuring the component cell under a reduced light intensity to produce a current similar to the current when it is used in a multi-junction solar cell, generating a new set of J-V data with fixed current values for all the component cells, and adding the voltages of the component cells at each given current value. For each current mismatch, the current values of component cells are multiplied by corresponding factors. Figure 31 (top plot) shows an example of an a-Si:H/a-SiGe:H/nc-Si:H triple-junction solar cell with a matched current of $J_{sc}=9.25 \text{ mA/cm}^2$. The component cell J-V characteristics are listed in Table XIV. We have kept the total current the same and numerically created current mismatch defined by $(J_T-J_B)/J_{av}$, where J_T is the top cell current, J_B the bottom current, and J_{av} the average current (9.25 mA/cm^2). During the calculation, the middle cell current density was set to equal the highest current density. For example, when the cell was bottom cell limited, the top and middle cell were set to the same current. From Fig. 31 (bottom plot), one can see that both the a-Si:H top and nc-Si:H bottom cell limited current mismatches result in high FFs, and the increase of FF has a clear correlation to the magnitude of the current mismatch. One notices that even through the nc-Si:H bottom cell has the smallest FF among the three component cells, the nc-Si:H bottom cell limited current mismatch still results in high FFs. The cell with a small bottom cell limited current mismatch shows the highest efficiency. As we previously reported, the nc-Si:H bottom cell limited current mismatch improved the stability of the cell after prolonged light soaking. Therefore, we can conclude that in general, a multi-junction solar cell with a nc-Si:H bottom cell should be designed to have a bottom cell limited current mismatch.

Table XIV. J-V characteristics of a-Si:H/a-SiGe:H/nc-Si:H triple-junction cells and its component cells

Cell Type	J_{sc} (mA/cm^2)	V_{oc} (V)	FF	P_{max} (mW/cm^2)
a-Si:H top	9.25	1.032	0.767	7.32
a-SiGe:H middle	9.25	0.754	0.712	5.00
nc-Si:H bottom	9.25	0.469	0.685	2.97
Triple-Junction	9.25	2.260	0.723	15.11

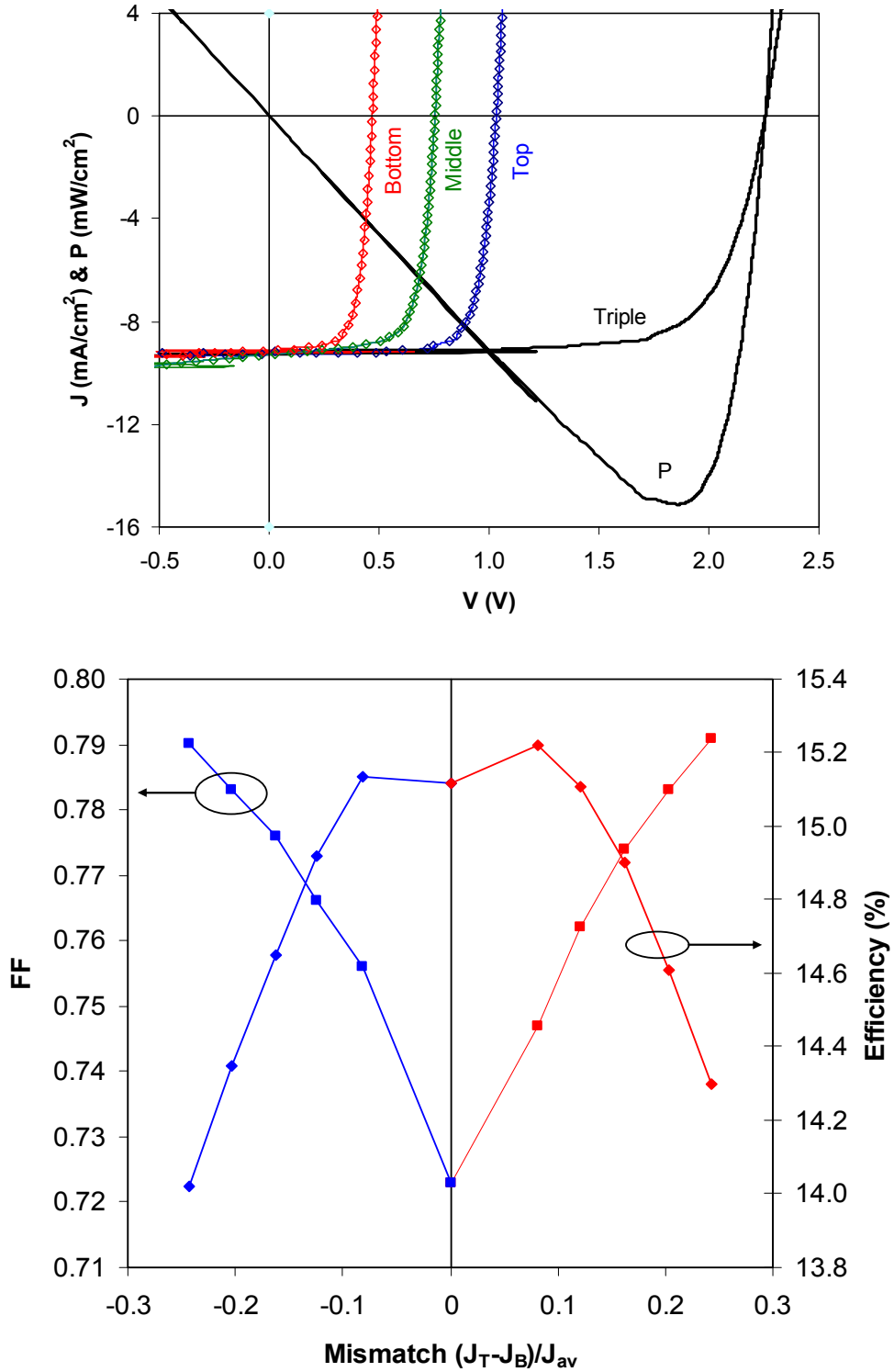


Figure 31. (upper): J-V characteristics of an a-Si:H/a-Si:H/nc-Si:H triple-junction cell and its component cells. The power versus voltage (P-V) characteristics of the triple-junction cell is also plotted; (lower): FF and efficiency of triple-junction cells as a function of current mismatch.

4.3.5. High efficiency triple-junction cells

We have used the optimized component cells to make high efficiency a-Si:H/a-SiGe:H/nc-Si:H and a-Si:H/nc-Si:H/nc-Si:H triple-junction cells. Last year, we reported an initial active-area efficiency of 15.1% using the same cell structure. In this quarter, we continued the optimization effort. We have made several a-Si:H/a-SiGe:H/nc-SiGe:H triple-junction cells with an initial active-area efficiency over 15%. Table XV lists the J-V characteristics of the high efficiency triple-junction cells. The highest record efficiency is 15.4% with J-V characteristics and QE curves shown in Fig. 32.

Table XVI summarizes the J-V characteristics of several a-Si:H/nc-Si:H/nc-Si:H triple-junction solar cells in the initial and light-soaked states, where the light-soaked state was reached by light soaking under $\sim 100 \text{ mW/cm}^2$ white light at 50°C for over 1000 hours. The highest initial active-area efficiency of 14.1% was achieved with the initial J-V characteristics and QE shown in Fig. 33. Although the a-Si:H/nc-Si:H/nc-Si:H triple-junction structure does not yield the highest initial efficiency, it shows a very small light-induced degradation of 4.3%, resulting from a better stability of the nc-Si:H middle cell compared to the a-SiGe:H middle cell. A stable active-area efficiency of 13.3% is also achieved with this cell structure.

Table XV. List of J-V characteristics of a-Si:H/a-SiGe:H/nc-Si:H triple junction solar cells with an initial active-area efficiency over 15%.

Run No.	V_{oc} (V)	FF	J_{sc} (mA/cm ²)	Q (mA/cm ²)				P_{max} (mW/cm ²)
				Total	Top	Middle	Bottom	
16192	2.191	0.767	9.03	27.50	9.19	9.28	9.03	15.2
16219	2.215	0.754	9.16	27.75	9.25	9.34	9.16	15.3
16235	2.233	0.740	9.06	27.46	9.06	9.27	9.13	15.0
16243	2.240	0.738	9.07	27.75	9.07	9.61	9.07	15.0
16247	2.239	0.753	9.13	27.85	9.13	9.45	9.27	15.4

Table XVI. J-V characteristics of high efficiency a-Si:H/nc-Si:H/nc-Si:H triple-junction solar cells. Deg. denotes the percentage of light-induced degradation. The bold numbers are the highest efficiencies and italic numbers are the limited current densities for J_{sc} .

Sample	State	Eff (%)	J_{sc} (mA/cm ²)	QE (mA/cm ²)			V_{oc} (V)	FF
				top	middle	bottom		
13955-33	Initial	14.14	9.11	9.11	9.72	<i>9.11</i>	1.965	0.790
	Stable	13.19	8.79	<i>8.79</i>	9.56	9.04	1.947	0.771
	Deg.	6.7%	3.5%	3.5%	1.6%	0.8%	0.9%	2.4%
13955-24	Initial	13.86	8.89	9.02	9.52	<i>8.89</i>	1.981	0.787
	Stable	13.26	8.72	8.75	9.25	<i>8.72</i>	1.973	0.771
	Deg.	4.3%	1.9%	3.0%	2.8%	1.9%	0.4%	2.0%
14005-33	Initial	13.67	8.99	9.44	9.54	<i>8.99</i>	1.944	0.782
	Stable	13.24	8.92	9.04	9.42	<i>8.92</i>	1.933	0.768
	Deg.	3.1%	0.8%	4.2%	1.3%	0.8%	0.6%	1.8%

4. 4. Summary

We have optimized the a-Si:H top cell, a-SiGe:H middle cell, and nc-Si:H bottom cell for high efficiency a-Si:H/a-SiGe:H/nc-Si:H triple-junction solar cells. The hydrogen dilution and hydrogen dilution profiling are the two important techniques for improving both amorphous and nanocrystalline silicon and silicon germanium solar cells. With the improved materials and optimized solar cell structures, we achieved a new record initial active-area efficiency of 15.4% using the a-Si:H/a-SiGe:H/nc-Si:H triple-junction structure. Similarly, we used an a-Si:H/nc-Si:H/nc-Si:H triple-junction structure to achieve a stable active-area efficiency of 13.3%. Both efficiencies exceeded those previously achieved with amorphous silicon and silicon germanium alloys [35,40].

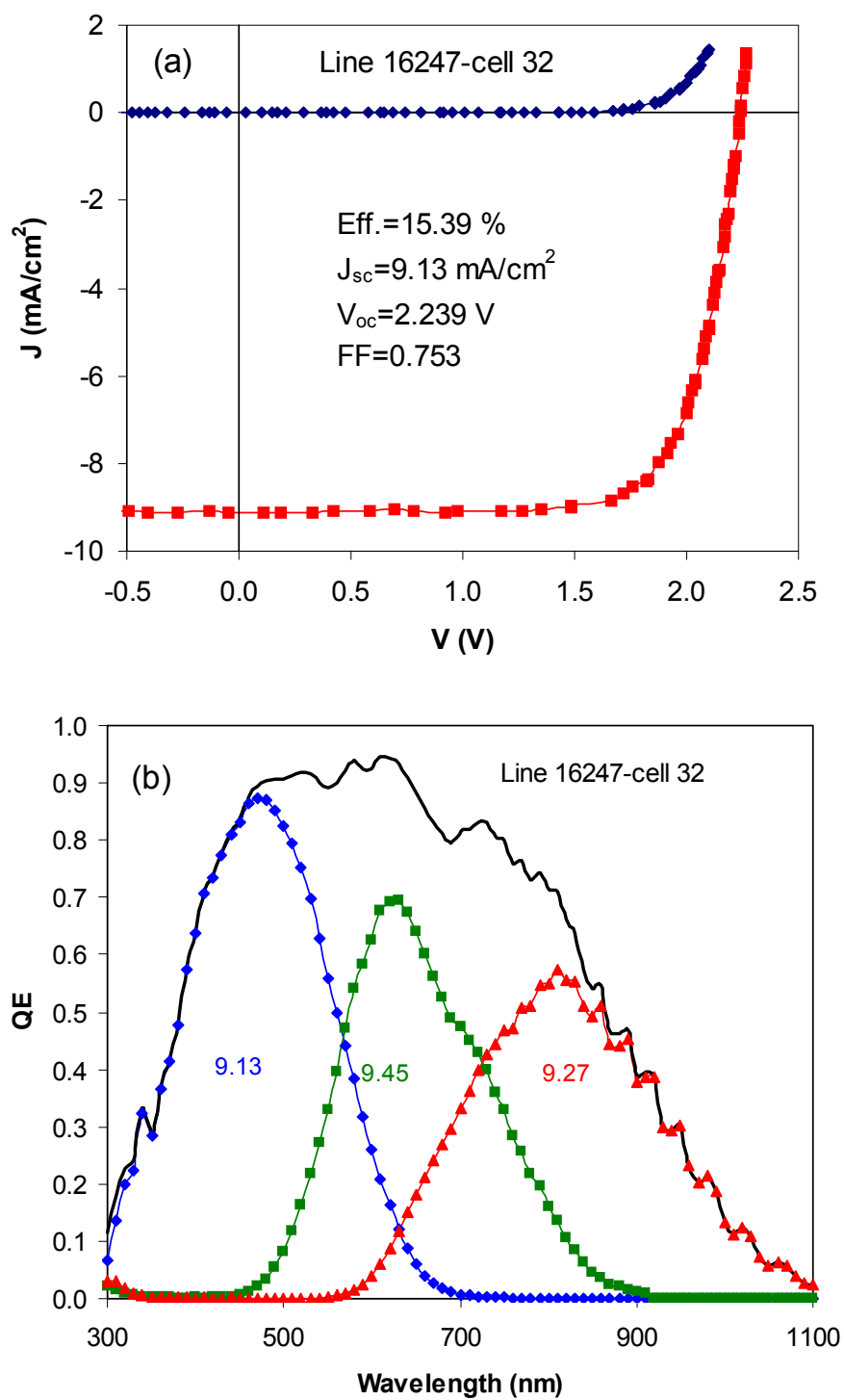


Figure 32. (a) J-V characteristics and (b) quantum efficiency curves of an a-Si:H/a-SiGe:H/nc-Si:H triple-junction cell with an initial active-area efficiency of 15.4%.

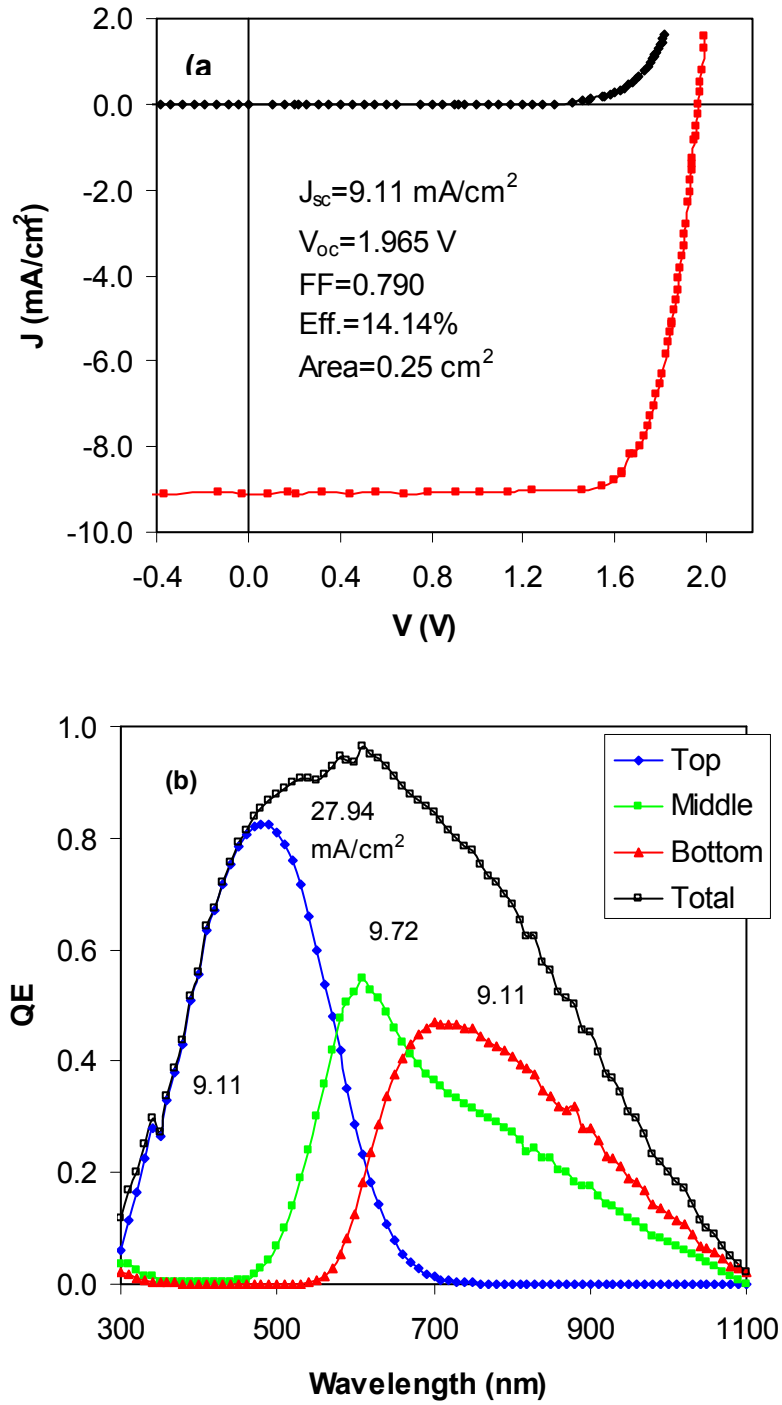


Figure 33. (a) J-V characteristics and (b) quantum efficiency curves of an a-Si:H/nc-Si:H/nc-Si:H triple-junction solar cell with an initial active-area efficiency of 14.1%.

5. High rate deposition of a-Si:H and a-SiGe:H solar cells using modified very high frequency glow discharge

5. 1. Introduction

A high deposition rate for making solar cell intrinsic layers is always desirable to increase throughput and reduce production cost. However, a-Si:H solar cells made with the conventional radio frequency (RF) glow discharge at high rates exhibit poor quality. The materials contain a high defect density, microvoids, and dihydride structures, which lead to a low initial efficiency and poor stability in solar cells. In order to reduce manufacturing costs, new deposition techniques are needed to increase the deposition rate without compromising the material quality. Obviously, increasing the deposition rate will directly increase the annual capacity or reduce the initial capital investment on the machine.

Very high frequency (VHF) glow discharge has been widely used in the deposition of a-Si:H [44] and nc-Si:H [1,41-42,45-47] materials and devices. Compared to the conventional RF technique, VHF plasma has higher electron density and lower ion energy, which is believed to increase the deposition rate and improve the material quality. In our laboratory, we have used a modified VHF (MVHF) system to make a-Si:H, a-SiGe:H [48,49], and nc-Si:H [41,42] solar cells. An initial efficiency of 11.2% was obtained in an a-Si:H/a-SiGe:H double-junction solar cell with the top cell intrinsic layer deposited at 8 Å/s and the bottom cell at 6 Å/s [49]. We have achieved an initial active-area efficiency of 9.0% on a nc-Si:H single-junction solar cell and a stabilized active efficiency of 13.3% on an a-Si:H/nc-Si:H/nc-Si:H triple junction solar cell [34]. In this project, we have optimized the deposition condition of a-Si:H in a wider growth parameter space, mainly in the higher pressure and smaller gap spacing regime. We have systematically studied the initial cell performance and stability as a function of the deposition rate.

5. 2. a-Si:H and a-SiGe:H single-junction solar cells made with MVHF at high deposition rates

A series of a-Si:H *n-i-p* solar cells has been made using an MVHF high rate a-Si:H intrinsic layer and low rate RF doped layers. Under each deposition condition, two runs were made: one on a specular stainless steel (SS) substrate and one on a Ag/ZnO back reflector (BR) coated SS substrate. The deposition rate of the a-Si:H intrinsic layer was changed from 5 to 14 Å/s by varying the VHF power and the pressure. The thickness of the intrinsic layer was controlled in the range of 200-220 nm. ITO dots with an active-area of 0.25 cm² were deposited on the *p* layer for J-V and QE measurements.

The deposition rate of a-Si:H depends on many deposition parameters such as the excitation (VHF or RF) power, gas pressure, and gas dilution ratio. Under a given condition, the most common way to increase the deposition rate is to increase the excitation power. Figure 34 shows the deposition rate of a-Si:H as a function of VHF power. One can see that the deposition rate continues to increase with the VHF power in the range of 9-14 Å/s. The deposition rate is also very sensitive to the gas pressure. In the high pressure regime, increasing the pressure leads to a decrease in the deposition rate. In this study, we focused on deposition rates in the range of 5 to 14 Å/s.

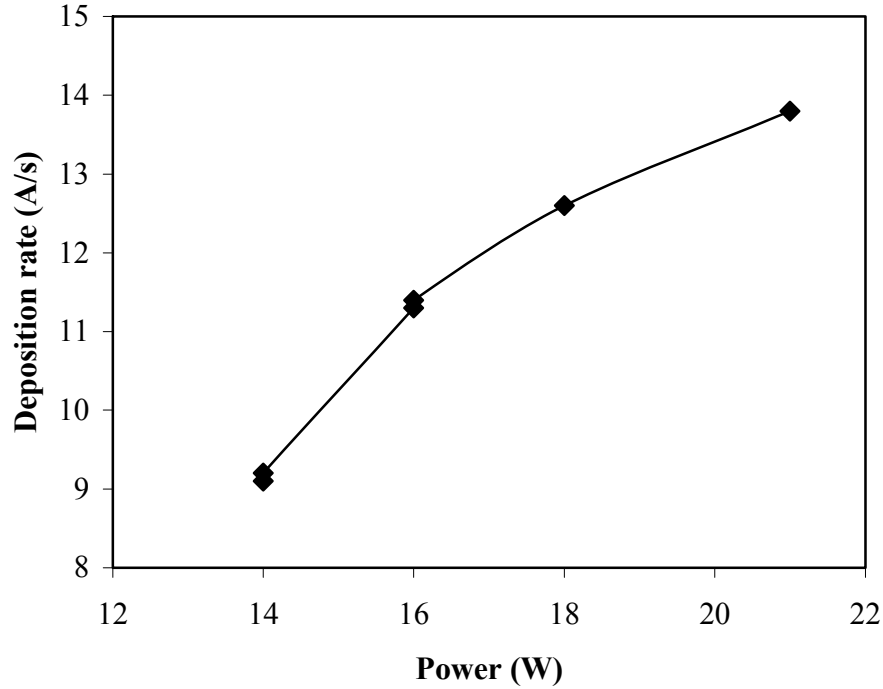


Figure 34. The deposition rate of a-Si:H as a function of VHF power.

Table XVII lists the J-V characteristics of the cells on both SS and BR substrates, where the J_{sc} is obtained from the QE measurements. FF_b and FF_r denote the FF obtained from the measurements with weak blue and red lights, respectively. Normally, we believe that the FF_b probes the interface between the *i* and *p* layers, while the FF_r detects the quality of the *i* layer. One can see that the cell performance does not have a strong dependence on the deposition rate. Most cells show a high FF_r , indicating a high quality of the a-Si:H intrinsic layer. The average efficiency is around 7% for the cells on SS and 10% for the cells on BR. Compared to the cells on SS, the V_{oc} and FF do not change much for the cells on BR, but the J_{sc} is increased by 40% due to light trapping, which directly improves the cell efficiency. The intrinsic layer thickness in all of the cells in the table is in the range of 200-220 nm. By increasing the intrinsic layer thickness to 330 nm, an efficiency of 10.6% ($J_{sc}=15.94 \text{ mA/cm}^2$, $V_{oc}=0.993 \text{ V}$, and $FF=0.674$) has been obtained with an a-Si:H single-junction cell on BR deposited at 10 Å/s .

Stability testing has been done on cells made with different deposition rates on SS and BR. The solar cells were light soaked under 100 mW/cm^2 white light at 50°C for 1000 hours. As a reference, two a-Si:H cells made with RF at a low rate of $\sim 1.0 \text{ Å/s}$ (one on SS and one on Ag/ZnO BR) were light-soaked together with the high rate MVHF cells. The results are listed in Tables XVIII and XIX for the cells on BR and on SS, respectively. Figure 35 shows the initial and stable efficiencies as well as the light-induced degradation as a function of the deposition rate. The light-induced degradation rate of the efficiency varies from 15% to 17% for cells on both BR and SS, but it does not show any dependence on the deposition rate. The highest stabilized efficiency of 8.64% has been achieved with an a-Si:H single-junction cell made at 9.3 Å/s on Ag/ZnO back reflector.

Table XVII. Performance of a-Si:H solar cells made with MVHF on BR and SS substrates. FF_b and FF_r represent the FF measured under weak blue and red lights, respectively. The values of J_{sc} are from QE measurements.

Sample No.	V_{oc} (V)	FF			J_{sc} (mA/cm ²)	Eff (%)	Substrate	Rate (Å/s)	<i>i</i> layer time (seconds)
		FF	FF_b	FF_r					
14325	0.983	0.712	0.759	0.753	14.34	10.04	BR	5.2	420
14166	1.000	0.735	0.767	0.749	9.71	7.14	SS		
14324	1.001	0.723	0.763	0.750	13.68	9.90	BR	6.1	300
14139	0.974	0.727	0.765	0.780	9.62	6.81	SS		
14347	0.987	0.702	0.722	0.744	14.67	10.16	BR	9.2	288
14336	0.988	0.710	0.760	0.770	10.36	7.27	SS		
14323	0.993	0.709	0.741	0.741	14.69	10.34	BR	9.3	240
14318	0.978	0.697	0.754	0.763	10.48	7.14	SS		
14346	0.986	0.696	0.716	0.742	14.46	9.92	BR	11.4	222
14335	0.995	0.698	0.764	0.747	10.43	7.24	SS		
14338	0.997	0.704	0.743	0.751	13.68	9.60	BR	11.9	180
14330	0.985	0.714	0.755	0.768	9.96	7.00	SS		
14345	0.984	0.697	0.717	0.742	14.20	9.74	BR	12.6	175
14342	0.986	0.713	0.760	0.767	9.89	6.95	SS		
14348	0.982	0.710	0.717	0.743	14.11	9.84	BR	13.8	156
14333	0.995	0.713	0.769	0.763	9.64	6.84	SS		

Table XVIII. Stability results of a-Si:H solar cells on Ag/ZnO BR coated SS made by MVHF at high rates. For comparison, a sample (14028) made by RF at a low rate of 1.0 Å/s has been light-soaked with the high rate samples. The thickness for all of the samples is in the range of 200-220 nm.

Sample No.	State	V _{oc} (V)	FF			J _{sc} (mA/cm ²)	Eff (%)	Rate (Å/s)
			AM1.5	FF _b	FF _r			
14028	Initial	1.020	0.695	0.740	0.719	13.78	9.77	1.0
	Stable	0.998	0.640	0.636	0.653	13.12	8.38	
	Deg(%)	2.2%	7.9%			4.8%	14.2%	
14325	Initial	0.983	0.712	0.759	0.753	14.34	10.04	5.2
	Stable	0.951	0.645	0.677	0.665	13.92	8.54	
	Deg(%)	3.3%	9.4%			2.9%	14.9%	
14324	Initial	1.001	0.723	0.763	0.750	13.68	9.90	6.1
	Stable	0.965	0.668	0.697	0.676	13.05	8.41	
	Deg(%)	3.6%	7.6%			4.6%	15.1%	
14347	Initial	0.987	0.702	0.722	0.744	14.67	10.16	9.2
	Stable	0.958	0.645	0.647	0.667	13.67	8.45	
	Deg(%)	2.9%	8.1%			6.8%	16.8%	
14323	Initial	0.993	0.709	0.741	0.741	14.69	10.34	9.3
	Stable	0.956	0.649	0.644	0.639	13.92	8.64	
	Deg(%)	3.7%	8.5%			5.2%	16.4%	
14346	Initial	0.986	0.696	0.716	0.742	14.46	9.92	11.4
	Stable	0.960	0.655	0.663	0.684	13.49	8.48	
	Deg(%)	2.6%	5.9%			7.2%	14.5%	
14338	Initial	0.997	0.704	0.743	0.751	13.68	9.60	11.9
	Stable	0.959	0.645	0.681	0.672	13.20	8.15	
	Deg(%)	3.8%	8.4%			3.5%	15.1%	
14345	Initial	0.984	0.697	0.717	0.742	14.20	9.74	12.6
	Stable	0.960	0.648	0.656	0.675	13.41	8.34	
	Deg(%)	2.4%	7.0%			5.6%	14.4%	
14348	Initial	0.982	0.710	0.717	0.743	14.11	9.84	13.8
	Stable	0.959	0.659	0.662	0.673	13.34	8.43	
	Deg(%)	2.3%	7.2%			5.5%	14.3%	

Table XIX. Stability results of MVHF high rate a-Si:H solar cells on SS. As a reference, a RF low rate a-Si:H cell RF (13899) is also included. The thicknesses for all of the samples are in the range of 200-220 nm.

Sample No.	State	V _{oc} (V)	FF			J _{sc} (mA/cm ²)	Eff (%)	Rate (Å/s)
			AM1.5	Blue	Red			
13899	Initial	1.014	0.748	0.782	0.760	9.82	7.45	1.0
	Stable	0.974	0.676	0.720	0.677	9.37	6.17	
	Deg. (%)	3.94%	9.63%			4.58%	17.2%	
14166	Initial	1.002	0.732	0.775	0.760	9.71	7.14	5.2
	Stable	0.959	0.661	0.697	0.655	9.41	5.96	
	Deg. (%)	4.3%	9.7%			3.1%	16.5%	
14308	Initial	0.997	0.733	0.782	0.751	9.61	7.07	7.5
	Stable	0.958	0.663	0.721	0.669	9.30	5.91	
	Deg. (%)	3.9%	9.5%			3.2%	16.4%	
14309	Initial	0.979	0.699	0.776	0.752	10.09	6.94	9.0
	Stable	0.944	0.636	0.702	0.636	9.71	5.83	
	Deg. (%)	3.6%	9.0%			3.8%	16.0%	
14318	Initial	0.979	0.702	0.757	0.762	10.48	7.14	9.3
	Stable	0.943	0.626	0.688	0.648	10.05	5.93	
	Deg. (%)	3.7%	10.8%			4.1%	16.9%	
14370	Initial	0.984	0.713	0.756	0.769	10.14	7.11	11.3
	Stable	0.950	0.673	0.687	0.666	9.45	6.04	
	Deg. (%)	3.5%	5.6%			6.8%	15.0%	
14342	Initial	0.986	0.713	0.762	0.765	9.89	6.95	12.6
	Stable	0.952	0.647	0.678	0.670	9.33	5.75	
	Deg. (%)	3.2%	9.3%			5.7%	17.3%	
14333	Initial	0.995	0.713	0.760	0.754	9.64	6.84	13.8
	Stable	0.957	0.650	0.694	0.653	9.17	5.70	
	Deg. (%)	3.8%	8.8%			4.9%	16.7%	

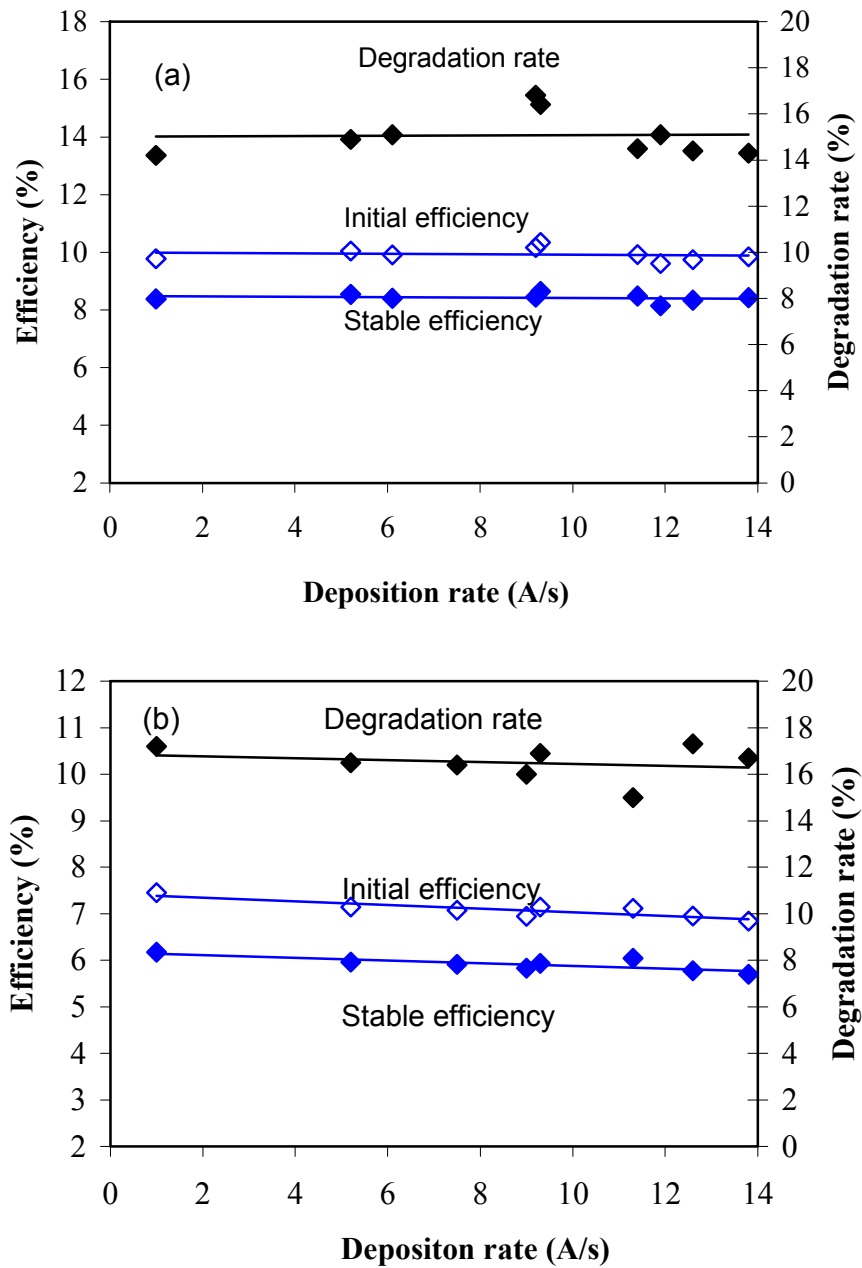


Figure 35. Initial and stable efficiencies of MVHF-deposited a-Si:H, as well as their degradation ratios, as a function of the deposition rate for the cells on (a) BR and (b) SS.

A series of a-SiGe:H *n-i-p* single-junction cells was made using a MVHF high rate a-SiGe:H intrinsic layer and RF doped layers on stainless steel substrates. The *n/i* and *i/p* buffer layers were made using RF at a low rate of ~ 1 Å/s. Specular stainless steel substrates were used. It is known that the a-SiGe:H cell performance strongly depends on the Ge/Si ratio in the intrinsic layer and this ratio depends on the deposition rate even if the same $\text{GeH}_4/\text{SiH}_4$ ratio in the gas flow rate is used. The reason for the Ge/Si ratio dependence on the deposition rate is due to the difference in the power dependence of the decomposition rate of SiH_4 and GeH_4 in the

plasma. In order to simplify the study, the deposition time of the a-SiGe:H intrinsic layer was fixed at 4 minutes, which corresponds to a deposition rate of $\sim 10 \text{ \AA/s}$. The major techniques to optimize the recipe include: (1) a proper GeH_4 ramping to enhance the hole collection, (2) an optimized i/p buffer to reduce the shunt current and interface recombination, and (3) optimized p and n layers to reduce the series resistance.

Table XX lists the J-V characteristics of typical a-SiGe:H component cells made at high rates. In this study, we focused on medium bandgap materials, which give an AM1.5 V_{oc} around 0.75 to 0.80 V for the a-SiGe:H component cell in a high efficiency a-Si:H/a-SiGe:H double-junction structure. In order to investigate the long wavelength response and simulate the performance when the a-SiGe:H cell is placed in an a-Si:H/a-SiGe:H double-junction structure, we measured the cell performance under an AM1.5 solar simulator with a 530-nm cut-on filter. From previous experience, a P_{max} of 4 mW/cm^2 is a benchmark for a good a-SiGe:H component cell on a stainless steel substrate. In this study, we achieved an active-area P_{max} of 4.4 mW/cm^2 under AM1.5 illumination with a 530-nm cut-on filter.

Table XX. J-V characteristics of a typical a-SiGe:H component cells made with MVHF at high rates. The intrinsic layer deposition time for all the cells was 4 minutes. The results in parentheses were measured under AM1.5 with a 530 nm cut-on filter.

Sample No.	V_{oc} (> 530 nm) (V)	FF (> 530 nm)	J_{sc} (> 530 nm) (mA/cm^2)	P_{max} (> 530 nm) (mW/cm^2)
14407	0.795(0.775)	0.667(0.696)	13.49(7.82)	7.15(4.22)
14583	0.768(0.751)	0.648(0.671)	14.41(8.66)	7.17(4.36)
14584	0.768(0.750)	0.664(0.681)	14.23(8.60)	7.26(4.39)

Table XXI. Stability of a-SiGe:H component cells on SS made by MVHF at a deposition rate of $\sim 10 \text{ \AA/s}$. Light soaking was carried out under a 100 mW/cm^2 white light with a 515 nm cut-on filter at 50°C for 1095 hours. The cells were measured under an AM1.5 solar simulator with a 530-nm cut-on filter at 25°C .

Sample No.	Status	V_{oc} (V)	FF	J_{sc} (mA/cm^2)	P_{max} (mW/cm^2)
14382	Initial	0.784	0.693	7.67	4.17
	Stable	0.728	0.553	7.06	2.84
	Degradation (%)	7.1%	20.2%	8.0%	31.9%
14395	Initial	0.780	0.677	7.67	4.05
	Stable	0.722	0.542	7.05	2.76
	Degradation (%)	7.4%	19.9%	8.1%	31.9%
14407	Initial	0.774	0.682	7.82	4.13
	Stable	0.718	0.545	7.36	2.88
	Degradation (%)	7.2%	20.1%	5.9%	30.3%
14397	Initial	0.785	0.675	7.50	3.97
	Stable	0.727	0.538	6.92	2.71
	Degradation (%)	7.4%	20.3%	7.7%	31.7%

We also studied the stability of the a-SiGe:H component solar cells. Light soaking was done under a 100 mW/cm^2 white light with a proper long wavelength pass filter, which results in a J_{sc} in the a-SiGe:H cells similar to the J_{sc} in an a-Si:H/a-SiGe:H double-junction structure. The temperature of the light soaking stage was controlled at 50°C during the light soaking. After over 1000 hours of light soaking the solar cell performance was stabilized. Table XXI lists the initial and stable J-V characteristics measured under an AM1.5 solar simulator with a 530-nm cut-on filter. It appears that the cell performance degrades about 31% on average, which is similar to the light-induced degradation observed in the a-SiGe:H component cells made with RF glow discharge at 3 \AA/s .

5. 3. a-Si:H/a-SiGe:H double-junction solar cells made with MVHF at high rates

Having optimized the a-Si:H top and a-SiGe:H bottom cells, we proceeded to combine them to make a-Si:H/a-SiGe:H double-junction solar cells on Ag/ZnO coated stainless steel substrates. The deposition time for both the a-Si:H intrinsic layer in the top cell and a-SiGe:H intrinsic layer in the bottom cell was fixed at 4 minutes. The J-V characteristics of typical double-junction cells are listed in Table XXII. An initial active-area efficiency of 11.7% has been achieved. The J-V curves and QE spectrum of the best a-Si:H/a-SiGe:H double-junction cell are plotted in Fig. 35.

Table XXII. J-V characteristics of the a-Si:H/a-SiGe:H double-junction cells made at high rates. The deposition time for both top and middle cell intrinsic layers was 4 minutes.

Sample No.	V_{oc} (V)	FF	QE (mA/cm^2)			P_{max} (mW/cm^2)
			Top	Bottom	Total	
14520	1.719	0.717	9.50	10.94	20.44	11.71
14530	1.696	0.664	10.23	10.16	20.39	11.44
14534	1.700	0.679	9.78	10.48	20.26	11.29

5. 4. Summary

In summary, we have found that the MVHF-deposited a-Si:H solar cells showed good initial efficiency and stability. The most important result is that the cell performance and stability do not depend on the deposition rate up to 14 \AA/s . This phenomenon is quite different from the cells made using RF at high rates. The degradation rate of the RF-cells usually increases with the deposition rate. We have also optimized the a-SiGe:H component cells at high deposition rates on SS substrate. An active-area P_{max} of 4.4 mW/cm^2 has been achieved under AM1.5 with a 530 nm cut-on filter. The light-induced degradation of the a-SiGe:H component cells is about 31%, which is similar to the cells made with RF glow discharge at 3 \AA/s . By combining this cell with an optimized high rate a-Si:H top cell, we have made an a-Si:H/a-SiGe:H double-junction cell on Ag/ZnO coated SS with an initial active-area efficiency of 11.7%.

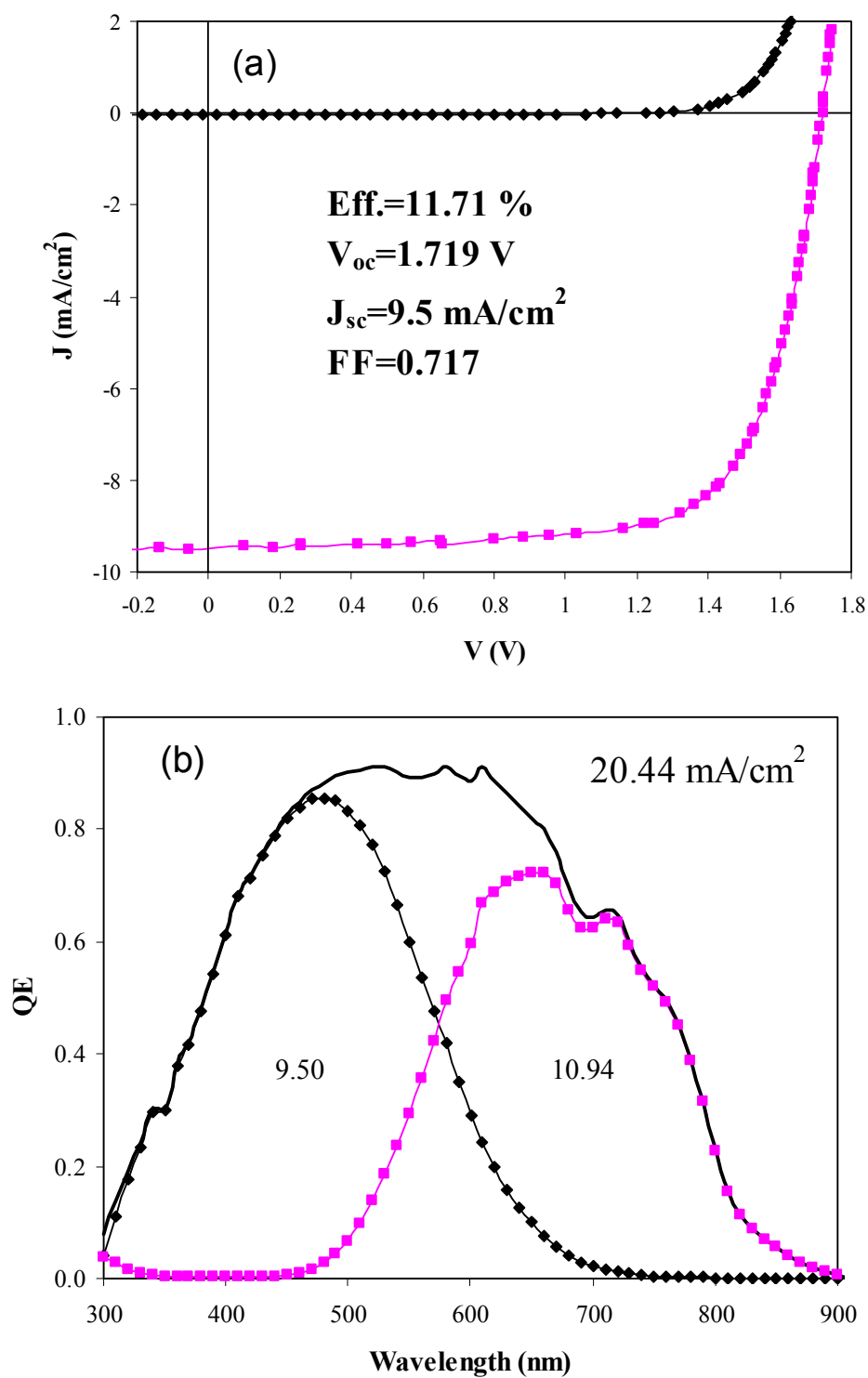


Figure 35. (a) J-V characteristics and (b) QE spectrum of an a-Si:H/a-SiGe:H double-junction cell made at 10 Å/s using MVHF.

6. Large-area a-Si:H/a-SiGe:H/a-SiGe:H triple-junction and a-Si:H/nc-Si:H double-junction solar cells

6. 1. Introduction

One of our major objectives for this project is to develop new deposition parameters for improving solar cell efficiency and throughput, and hence reducing the cost of manufacturing. The spectrum splitting a-Si:H/a-SiGe:H/a-SiGe:H triple-junction structure on Al/ZnO back reflector is used in our current 118 MW manufacturing lines in Auburn Hills and Greenville, Michigan. Therefore, one task of the project is to optimize the deposition parameters of a-Si:H/a-SiGe:H/a-SiGe:H triple-junction solar cells under the manufacturing constraints, mainly the deposition time of each layer. Previously, we have achieved a stable total-area (0.268 cm^2) cell efficiency of 9.1% and stable aperture-area (460 cm^2) module efficiency of 8.9% using our large-area batch machine. Those cells were deposited with Si_2H_6 and GeH_4 mixtures under the manufacturing constraints on Al/ZnO back reflectors. In order to reduce cost, we have switched to SiH_4 and GeH_4 mixtures in the manufacturing process. In the research and development department, we have also studied the optimization of the deposition conditions using the SiH_4 and GeH_4 mixtures. We achieved a stable total-area (0.268 cm^2) triple-junction cell efficiency of 9.1%, which is similar to the result obtained with the Si_2H_6 and GeH_4 mixture. This result showed that, in principle, one can achieve a similar performance using inexpensive SiH_4 instead of Si_2H_6 . In this project, we have carried out optimization of large-area deposition of a-Si:H/a-SiGe:H/a-SiGe:H triple-junction solar cells using SiH_4 and GeH_4 gas mixtures. Al/ZnO back reflectors made in the production machines were used.

For the future a-Si:H based thin film manufacturing technology, improving the module efficiency and reducing the cost are the two major challenges. One of the promising new technologies is using nc-Si:H in the bottom cell of multi-junction structures. As presented above, we have studied the material and device optimization of nc-Si:H solar cells using small area machines. In addition, we also studied large-area a-Si:H/nc-Si:H double-junction solar modules at a low rate [50]. In this project, we have investigated a-Si:H/nc-Si:H double-junction solar cells made with RF glow discharge at high deposition rates.

6. 2. Experimental details

For a-Si:H/a-SiGe:H/a-SiGe:H triple-junction structures, we used one of our large-area ($14 \times 15 \text{ in}^2$) batch machines (2B) for the deposition of a-Si:H and a-SiGe:H intrinsic layers as well as the doped layers. The deposition time of each layer is fixed according to the calculation with the web speed and the chamber lengths of the production line. The triple-junction solar cells and modules were deposited on Al/ZnO back reflector coated stainless steel substrates. For RF deposited a-Si:H/nc-Si:H double-junction solar cells and modules, we used the 2B machine with RF glow discharge at a high rate of $\sim 3 \text{ \AA/s}$.

The optimization of cell performance and uniformity were carried out using small Indium Tin Oxide (ITO) dots with an active-area of 0.25 cm^2 . Large-area ($>400 \text{ cm}^2$) modules were made using the center area of the substrate with wires and bus bars. The large-area modules were encapsulated with a procedure similar to that used in the manufacturing process. The small-area cells were measured using an AM1.5 ORC solar simulator with quantum efficiency

(QE) correction for the short-circuit current density. The large-area modules were measured at various states of light soaking using a Spire solar simulator with an NREL calibrated c-Si solar cell with a proper filter. The light soaking experiments were done under 100 mW/cm² white light at 50 °C for over 1000 hours.

6. 3. a-Si:H/a-SiGe:H/a-SiGe:H triple-junction cells under manufacturing constraints

The uniformities of thickness and cell performance are major concerns for large-area deposition. In order to obtain high module efficiency, the cell performance has to satisfy certain uniformity requirements. We deposited the samples on a large-area (14×15 in²) substrate and then cut them into 1.85×1.85 in² pieces at different locations. Since we normally make 8.5×8.5 in² modules, we cut nine pieces from an area 9.2×9.2 in². One is in the center of the substrate, one at the middle of each of the four edges, and one at each of the four corners of the 9.2×9.2 in² area. Sixteen small ITO dots, with an active area of 0.25 cm², were deposited on the nine pieces for J-V and QE measurements. Table XXIII lists the cell performance from one run (2B 11147). The J-V data for each location are averages of the measurements on four cells. The uniformity of the cell performance in the given area is reasonably good. The highest initial J-V measured active-area efficiency is 11.06% (QE corrected 10.92%), and the average is 10.62% with a non-uniformity of ±5%. This uniformity is acceptable for large-area modules.

Table XXIII. J-V characteristics of a-Si:H/a-SiGe:H/a-SiGe:H triple-junction cells at different locations in a large-area cell, where the J_{sc} was taken directly from the J-V measurements. QE current densities and QE corrected efficiency (Eff^Q) of five cells are listed as a reference.

Location in 2B 11147	J_{sc} (mA/cm ²)	V_{oc} (V)	FF	Eff (%)	Eff^Q (%)	QE (mA/cm ²)		
						Top	Mid.	Bot.
Left North	7.41	2.195	0.656	10.67				
Left Center	7.40	2.220	0.659	10.82				
Left South	7.27	2.238	0.663	10.78	10.62	7.28	7.16	7.36
Central North	7.18	2.238	0.688	11.06	10.92	7.09	7.20	7.22
Central Center	7.24	2.237	0.679	10.98	10.66	7.02	7.31	7.28
Central South	7.22	2.207	0.676	10.77	10.49	7.03	7.49	7.32
Right North	7.47	2.161	0.623	10.05				
Right Center	7.49	2.122	0.634	10.28	9.83	7.31	7.41	7.48
Right South	7.38	2.159	0.636	10.14				
Average	7.34	2.197	0.657	10.62				

Several large-area modules have been made with the same deposition recipe as the cells shown in Table XXIII. The modules were measured at the states before and after lamination, as well as various light soaked states. Table XXIV lists the aperture-area performance of four modules. The data presented here are as-measured data without spectral mismatch corrections. The encapsulation causes a decrease of 1-4% in J_{sc} , 0.4-1.0% in V_{oc} , but an increase of 0-1.5% in FF. The major light-induced degradation appears in the first 500 hours. The change in the last 500 hours is very small. The average light-induced degradation is about 15.7%, which is similar to that observed in our previous experiments of a-Si:H/a-SiGe:H/a-SiGe:H triple-junction solar cells. The major change is in the FF, where an average of 10.6% reduction was observed aft

Table XXIV. Summary of a-Si:H/a-SiGe:H/a-SiGe:H triple-junction module performance in different states. $\text{Eff}^T(\%)$ is temperature corrected efficiency at 25 °C.

Sample 2B#	State	Area (cm ²)	T (°C)	I _{sc} (A)	J _{sc} (mA/cm ²)	V _{oc} (V)	FF	P _{max} (W)	Eff (%)	Eff ^T (%)
10386	Before lamination	420.0	24.2	2.960	7.05	2.190	0.654	4.24	10.09	10.08
	After lamination	413.8	24.2	2.882	6.96	2.180	0.662	4.16	10.05	10.04
	Change due to lamination				-1.3%	-0.5%	1.2%			-0.4%
	585-hour light soaking	413.8	24.2	2.820	6.81	2.100	0.606	3.58	8.65	8.64
	1004-hour light soaking	413.8	25.1	2.813	6.80	2.090	0.599	3.52	8.51	8.51
	Change due to light soaking				-2.3%	-4.1%	-9.5%			-15.2%
10383	Before lamination	420.0	23.9	2.947	7.02	2.210	0.662	4.31	10.25	10.24
	After lamination	416.0	25.1	2.876	6.91	2.180	0.671	4.20	10.10	10.11
	Change due to lamination				-1.6%	-1.4%	1.3%			-1.3%
	585-hour light soaking	416.0	24.4	2.833	6.81	2.100	0.616	3.66	8.80	8.80
	1004-hour light soaking	416.0	24.9	2.811	6.76	2.100	0.609	3.59	8.63	8.63
	Change due to light soaking				-2.2%	-3.7%	-9.2%			-14.6%
11156	Before lamination	462.0	23.7	3.382	7.32	2.230	0.645	4.87	10.54	10.53
	After lamination	458.0	24.2	3.239	7.07	2.220	0.654	4.70	10.26	10.25
	Change due to lamination				-3.4%	-0.4%	1.4%	-3.5%	-2.6%	-2.7%
	585-hour light soaking	458.0	24.7	3.236	7.07	2.13	0.584	4.02	8.78	8.78
	1004-hour light soaking	458.0	24.9	3.231	7.05	2.12	0.569	3.89	8.50	8.50
	Change due to light soaking				-0.3%	-4.5%	-13.1%			-17.0%
11166	Before lamination	462.0	23.7	3.349	7.25	2.230	0.650	4.85	10.50	10.47
	After lamination	458.0	24.4	3.215	7.02	2.210	0.651	4.63	10.11	10.10
	Change due to lamination				-3.2%	-0.9%	0.2%	-4.5%	-3.7%	-3.5%
	585-hour light soaking	458.0	24.4	3.199	6.98	2.110	0.581	3.92	8.56	8.55
	1004-hour light soaking	458.0	25.4	3.176	6.93	2.110	0.578	3.88	8.47	8.47
	Change due to light soaking				-1.3%	-4.5%	-11.2%			-16.1%

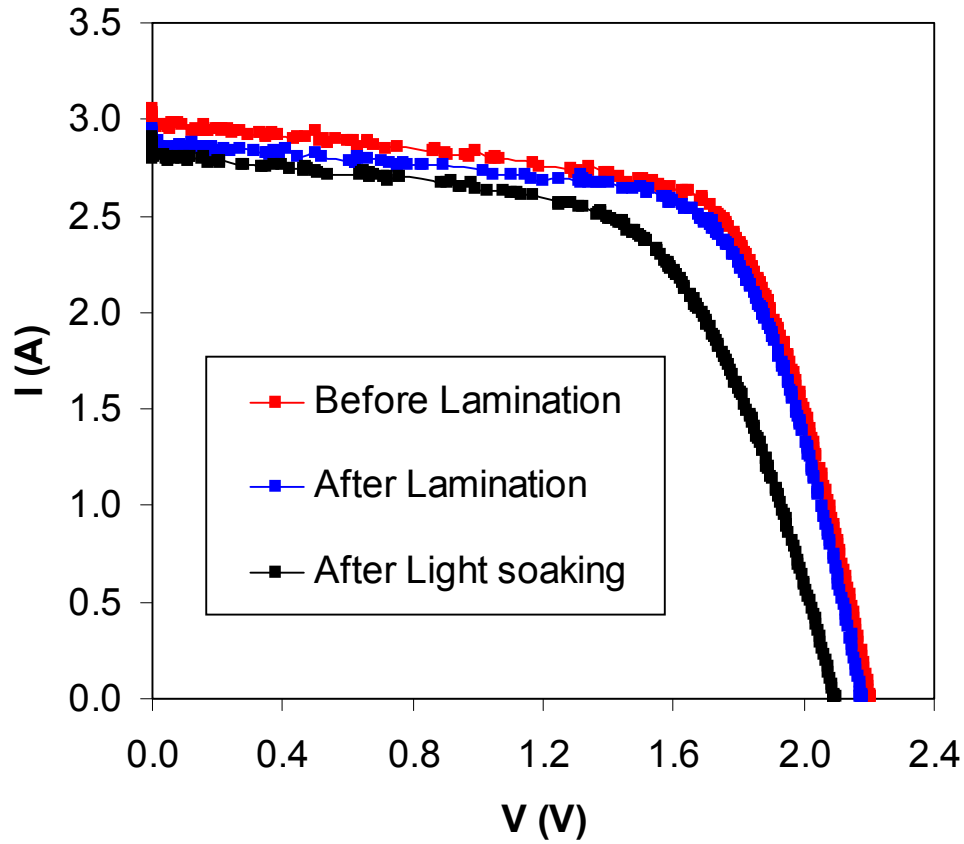


Figure 36. I-V characteristics of an a-Si:H/a-SiGe:H/a-SiGe:H triple-junction solar cell (2B 10383) before and after lamination, as well as after light soaking.

light soaking. The best stable aperture-area efficiency is 8.6%, which is slightly lower than the best module efficiency of 8.9% achieved using a Si_2H_6 and GeH_4 mixture. Figure 36 shows the I-V characteristics of the best module various different states.

It is well known that the efficiency measured under a given solar simulator with a calibrated reference cell is not necessarily the same as under the standard AM1.5 illumination due to the difference in their spectra. Normally two major errors appear in J_{sc} and FF. First is the difference between the spectrum of the light source and the ideal AM1.5 spectrum as well as the difference in the QE spectra of the testing and reference cells, both of which cause an error in J_{sc} . Second, the non-ideal AM1.5 spectrum of the light source causes a difference in the current mismatching of the component cells, which results in an error in FF.

In principle, the error in the J_{sc} of a single-junction solar cell can be corrected by adjusting the light intensity of the solar simulator based on a spectrum mismatching (M) factor [51]. The calculation of the M factor involves the reference light source (AM1.5) spectrum, the test light source (solar simulator) spectrum, the QE curve of reference cell and the QE curve of the test cell. In order to obtain a corrected J_{sc} , one can change the test light intensity by a factor of $1/M$ or use the measured J_{sc} under the standard setting condition and divide it by the M factor. Theoretically, the M-factor correction can provide a more accurate measurement of J_{sc} .

However, in practice, more errors could be introduced by the errors in the QE of the testing cell. The major problem is that it is hard to measure the QE of large-area modules. An alternative way is to use the QE measured from a different cell with a small area but made under the same condition. In most cases, one uses QE data from a small-area cell without encapsulation. It is well known that the encapsulation changes the QE curves and therefore, the M factor. In this study, we tried to make the measurement more accurate by using QE data that are close to the QE of real modules. We used adjacent pieces from the module fabrication and made small-area (1.2 cm^2) cells with the same wires and bus bars as used in the module fabrication. We also encapsulated the small-area cells and light soaked them using the same procedures as the large-area modules. The QE curves were measured at different states for calculating the M factor. It appears that the small-area cells have a slightly smaller V_{oc} and J_{sc} , but a slightly larger FF than the large-area modules at each corresponding state, which could be due to the non-uniformity of the deposition. Figure 37 gives an example of the QE changes from the initial non-encapsulated state to the encapsulated and light-soaked states. Corresponding reflection curves are also presented. The QE curves change dramatically at short wavelengths below 400 nm. We calculated the M-factors of the four cells at the initial non-encapsulated state and the encapsulated and light soaked states using the measured QE data and the QE of our reference cell as well as the spectrum of our Spire solar simulator. On average, the M factor is about 0.965 in the initial non-encapsulated state, and 0.983 in the final encapsulated and light-soaked state. If we take the M factor into account, the highest stable encapsulated module efficiency should be 8.78%.

6. 4. Large-area a-Si:H/nc-Si:H double-junction modules

We have continued to work on large-area a-Si:H/nc-Si:H double-junction cells using one of our large area multi-chamber batch systems (2B) using RF glow discharge decomposition of SiH_4 diluted with H_2 . In this project, the effort has been mainly focused on optimizing processing parameters under a lower pressure and a larger spacing between the cathode and sample substrate, which may ease process control in large volume manufacturing. The results summarized in Table XXV show that the cell performance made with the new processing conditions is comparable to the best cell performance achieved at the higher pressure and narrower spacing.

Table XXV. J-V characteristics of newly made a-Si:H/nc-Si:H double-junction solar cells (first two rows). The cells previously made with higher pressure and narrower spacing are also listed for the comparison (last two rows).

Sample No.	Area (cm^2)	V_{oc} (V)	FF	J_{sc} (mA/cm^2)	Eff. (%)	Comment
2B11770	462	1.48	0.762	10.40	11.73	Wider spacing
2B11774	462	1.49	0.743	10.53	11.66	
2B10582	420	1.44	0.729	11.21	11.77	Narrow spacing
2B10587	420	1.44	0.689	11.68	11.59	

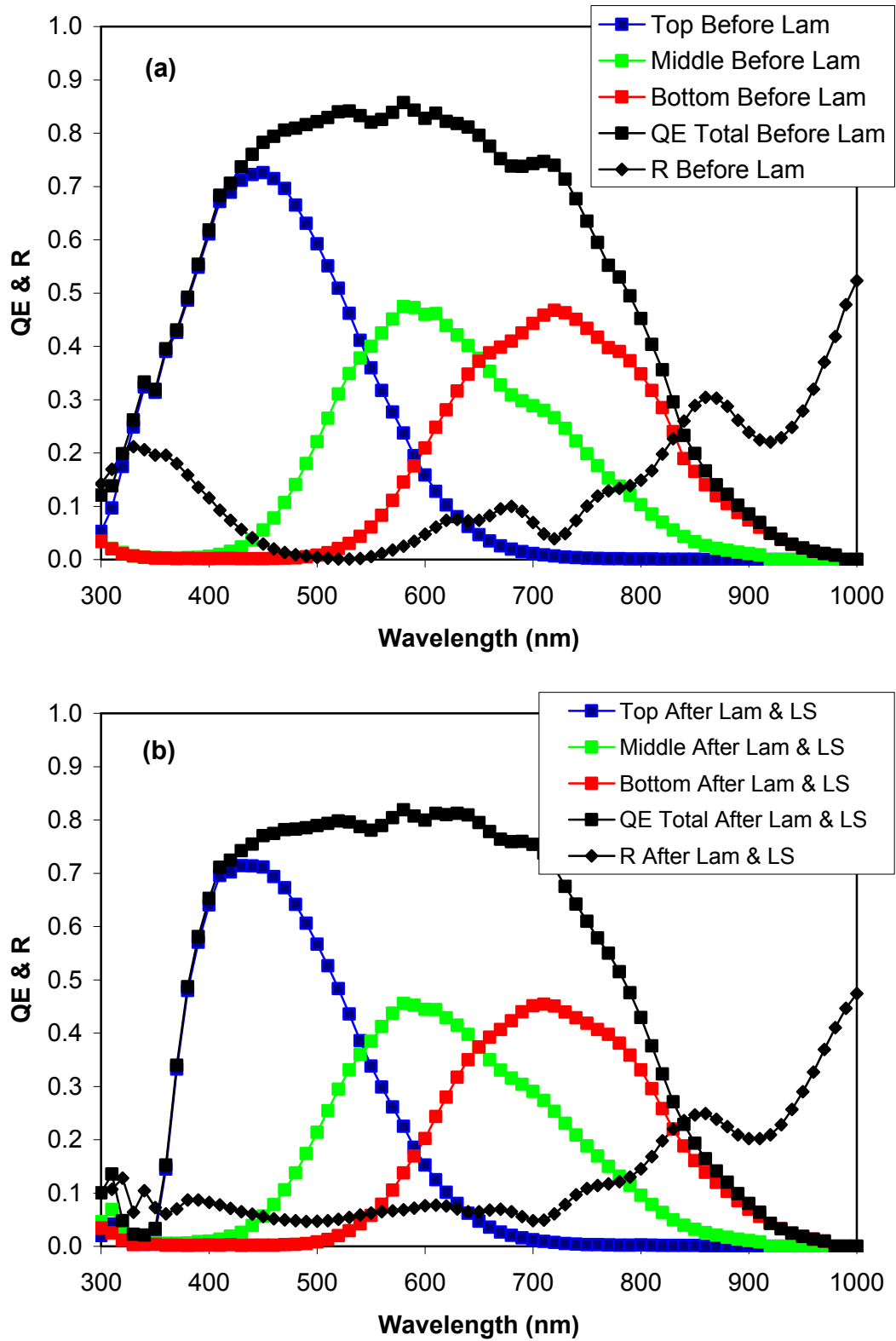


Figure 37. Quantum efficiency (QE) and reflection (R) curves of an a-Si:H/a-SiGe:H/a-SiGe:H triple-junction cell on Al/ZnO (a) before lamination and (b) after lamination and light soaking.

6. 5. Summary

We have optimized large-area deposition of a-Si:H/a-SiGe:H/a-SiGe:H triple-junction solar cells under the manufacturing constraints with a SiH₄ and GeH₄ gas mixture on Al/ZnO back reflectors from the manufacturing line. A stable aperture-area (416 cm²) efficiency of 8.6% has been achieved. With the spectrum mismatching correction, this efficiency could be 8.8%, which is similar to the highest module efficiency previously achieved using a Si₂H₆ and GeH₄ gas mixture.

We also optimized a-Si:H/nc-Si:H double-junction solar cells deposited on Ag/ZnO back reflectors with RF glow discharge at high deposition rates. An initial aperture-area efficiency of 11.7% has been achieved using a nc-Si:H deposition time of 50 minutes.

References:

1. For a review: A. V. Shah, J. Meier, E. Vallat-Sauvain, N. Wyrsch, U. Kroll, C. Droz, and U. Graf, *Sol. Energy Mater. & Sol. Cells* **78**, 469 (2003).
2. A. Matsuda, *Thin Solid Films* **337**, 1 (1999).
3. H. Fujiwara, J. Koh, P. I. Rovira, and R. W. Collins, *Phys. Rev.* **B61**, 10832 (2000)
4. R. W. Collins, A. S. Ferlauto, G. M. Ferreira, C. Chen, J. Koh, R. J. Koval, Y. Lee, J. M. Pearce, and C. R. Wronski, *Sol. Energy Mater. & Sol. Cells* **78**, 143 (2003).
5. H. Fujiwara, Y. Toyoshima, M. Kondo, and A. Matsuda, *Phys. Rev.* **B60**, 13598 (1999).
6. E. Vallat-Sauvain, U. Kroll, J. Meier, A. Shah, and J. Pohl, *J. Appl. Phys.* **87**, 3137 (2000).
7. T. Mates, P.C.P. Bronsveld, A. Fejfar, B. Rezek, J. Kocka, J.K. Rath, and R.E.I. Schropp, *J. Non-Cryst. Solids* **352**, 1011 (2006).
8. B. Yan, C.-S. Jiang, C.W. Teplin, H.R. Moutinho, M.M. Al-Jassim, J. Yang, and S. Guha, *J. Appl. Phys.* **101**, 033711 (2007).
9. C.-S. Jiang, B. Yan, H.R. Moutinho, M.M. Al-Jassim, J. Yang, and S. Guha, *Mater. Res. Soc. Symp. Proc.* **989**, 15 (2007).
10. C.-S. Jiang, H.R. Moutinho, M.M. Al-Jassim, L.L. Kazmerski, B. Yan, J.M. Owens, J. Yang, and S. Guha, *Proc. of 4th World Conf. on Photovoltaic Energy Conversion*, Hawaii, USA, 2006, p. 1552.
11. J. Kočka, A. Fejfar, H. Stuchlíková, J. Stuchlík, P. Fojtík, T. Mates, B. Rezek, K. Luterová, V. Švrček, and I. Pelant, *Sol. Energy Mater. & Sol. Cells* **78**, 493 (2003).
12. J. Yang, A. Banerjee, K. Lord, and S. Guha, *Proc. of 28th IEEE Photovoltaic Specialists Conference*, Anchorage, AK, September 15-22, 2000 (IEEE New York, 2000), p. 742.
13. T. Roschek, T. Repmann, J. Müller, B. Rech, H. Wagner, *Proc. of 28th IEEE Photovoltaic Specialists Conference*, Anchorage, AK, September 15-22, 2000, (IEEE New York, 2000), p. 150.

14. K. Lord, B. Yan, J. Yang, and S. Guha, Appl. Phys. Lett. **79**, 3800 (2001).
15. J. Yang, K. Lord, B. Yan, A. Banerjee, S. Guha, D. Han, and K. Wang, Mat. Res. Soc. Symp. Proc. **715**, 601 (2002).
16. D. L. Staebler and C. R. Wronski, Appl. Phys. Lett. **31**, 292 (1977).
17. B. Yan, J. Yang, and S. Guha, Proc. of 3rd World Conference on Photovoltaic Energy Conversion, Osaka, Japan, 2003, p. 1627.
18. T.I. Kamins, in Polycrystalline Silicon for Integrated Circuit Applications (Kluwer Academic Publishers, Boston USA, 1997), p. 32.
19. J. Bailat, E. Vallat-Sauvain, L. Feitknecht, C. Droz, and A. Shah, J. Non-Cryst. Solids, **299-302**, 1219 (2002).
20. Y. Nasuno, M. Kondo, and A. Matsuda, Proc. of 28th IEEE Photovoltaic Specialists Conference (IEEE, Anchorage, Alaska, 2000), p.142.
21. F. Finger, S. Klein, T. Dylla, A. L. Baia Neto, O. Vetterl, and R. Carius, Mater. Res. Soc. Symp. Proc. **715**, 123 (2002).
22. B. Yan, K. Lord, J. Yang, S. Guha, J. Smeets, and J.-M. Jacquet, Mater. Res. Soc. Symp. Proc. **715**, 629 (2002).
23. B. Yan, G. Yue, J. Yang, S. Guha, D. L. Williamson, D. Han, and C.-S. Jiang, Appl. Phys. Lett. **85**, 1955 (2004).
24. A. Gordijn, J. Francke, L. Hodakova, J. K. Roth, and R. E. I. Schropp, Mat. Res. Soc. Symp. Proc. **862**, 87 (2005).
25. A. Gordijn, J.K. Rath, and R.E.I. Schropp, Prog. Photovoltaics **14**, 305 (2006).
26. C. Das, X. Cao, W. Du, X. Yang, Y. Ishikawa, and X. Deng, Conf. Record of the 2006 IEEE 4th World Conf. on Photovoltaic Energy Conversion, (Hawaii, USA, May, 2006), p.1504.
27. G. Yue, B. Yan, G. Ganguly, J. Yang, S. Guha, and C. Teplin, Appl. Phys. Lett. **88**, 263507 (2006).
28. A. F. Halverson, J. J. Gutierrez, D. Cohen, B. Yan, J. Yang, and S. Guha, Mater. Res. Soc. Symp. Proc. **862**, 481 (2005).
29. M. H. Brodsky, M. Cardona, and J. J. Cuomo, Phys. Rev. B **16** 3556 (1977).
30. E. Bustarret, M. A. Hachicha, and M. Brunel, Appl. Phys. Lett. **52**, 1675 (1988).
31. E. Vallat-Sauvain, C. Droz, F. Meillaud, J. Bailat, A. Shah, and C. Ballif, J. Non-Cryst. Solids **352**, 1200 (2006).
32. A. Banerjee and S. Guha, J. Appl. Phys. **69**, 1030 (1991).
33. B. Yan, G. Yue, J.M. Owens, J. Yang, and S. Guha, Conf. Record of the 2006 IEEE 4th World Conf. on Photovoltaic Energy Conversion, (Hawaii, USA, May 7-12, 2006), p. 1477.

34. G. Yue, B. Yan, G. Ganguly, J. Yang, S. Guha, C. Teplin, and D. L. Williamson, Conf. Record of the 2006 IEEE 4th World Conf. on Photovoltaic Energy Conversion, (Hawaii, USA, May 7-12, 2006), p. 1588.
35. J. Yang, A. Banerjee, and S. Guha, Appl. Phys. Lett. **70**, 2975 (1997).
36. B. Yan, J. M. Owens, C.-S. Jiang, J. Yang, and S. Guha, Mater. Res. Soc. Symp. Proc. **862**, 603 (2005).
37. H.J. Simon, D.E. Mitchell, and J.G. Watson, Am. J. Phys. **43**, 630 (1975).
38. E. Yablonovitch, J. Opt. Soc. Am. **72**, 899 (1982).
39. J. Yang, A. Banerjee, and S. Guha, Sol. Energy Mater. & Sol. Cells **78**, 597 (2003).
40. J. Yang, A. Banerjee, K. Lord, and S. Guha, Proc. of 2nd World Conference and Exhibition on Photovoltaic Solar Energy Conversion, July 6-10, 1998, Vienna, Austria, p. 387.
41. B. Yan, J. M. Owens, J. Yang, and S. Guha, Proc. of 31st IEEE Photovoltaic Specialists Conference, Lake Buena Vista, FL, January 3-7, 2005, p. 1456.
42. B. Yan, G. Yue, J. Yang, A. Banerjee, and S. Guha, Mater. Res. Soc. Symp. Proc. **762**, 309 (2003).
43. T. Dylla, F. Finger, and E. A. Schiff, App. Phys. Lett. **87**, 032103 (2005).
44. A. Shah, J. Dutta, N. Wyrsh, K. Prasad, H. Curtins, F. Finger, A. Howling, and Ch. Hollenstein, Mater. Res. Soc. Symp Proc. **258**, 15 (1992).
45. J. Meier, P. Torres, R. Platz, S. Dubail, U. Kroll, J. A. Anna Selvan, N. Pellaton Vaucher, Ch. Hof, D. Fischer, H. Keppner, A. Shah, K.-D. Ufert, P. Giannoulès, and J. Koehler, Mater. Res. Soc. Symp. Proc. **420**, 3 (1990).
46. Y. Mai, S. Klein, R. Carius, J. Wolff, A. Lambertz, F. Finger, and X. Geng, J. Appl. Phys. **97**, 114913 (2005).
47. T. Matsui, A. Matsuda, and M. Kondo, Mater. Res. Soc. Symp Proc. **808**, 557 (2004).
48. J. Yang, S. Sugiyama, and S. Guha, Mater. Res. Soc. Symp Proc. **507**, 157 (1998).
49. J. Yang, B. Yan, J. Smeets, and S. Guha, Mater. Res. Soc. Symp Proc. **664**, A11.3 (2001).
50. B. Yan, G. Yue, A. Banerjee, J. Yang, and S. Guha, Mater. Res. Soc. Symp Proc. **808**, 581 (2004).
51. K. A. Emery, C. R. Osterwald, T. W. Cannon, D. R. Myers, J. Burdick, T. Glatfelter, W. Czubytyj, and J. Yang, Proceeding of 18th IEEE Photovoltaic Specialist Conference, (IEEE, 1985), p. 623.

REPORT DOCUMENTATION PAGEForm Approved
OMB No. 0704-0188

The public reporting burden for this collection of information is estimated to average 1 hour per response, including the time for reviewing instructions, searching existing data sources, gathering and maintaining the data needed, and completing and reviewing the collection of information. Send comments regarding this burden estimate or any other aspect of this collection of information, including suggestions for reducing the burden, to Department of Defense, Executive Services and Communications Directorate (0704-0188). Respondents should be aware that notwithstanding any other provision of law, no person shall be subject to any penalty for failing to comply with a collection of information if it does not display a currently valid OMB control number.

PLEASE DO NOT RETURN YOUR FORM TO THE ABOVE ORGANIZATION.

1. REPORT DATE (DD-MM-YYYY) May 2008			2. REPORT TYPE Subcontract Report		3. DATES COVERED (From - To) 30 January 2006 - 29 January 2008	
4. TITLE AND SUBTITLE High-Efficiency Amorphous Silicon and Nanocrystalline Silicon-Based Solar Cells and Modules: Final Technical Progress Report, 30 January 2006 - 29 January 2008				5a. CONTRACT NUMBER DE-AC36-99-GO10337		
				5b. GRANT NUMBER		
				5c. PROGRAM ELEMENT NUMBER		
6. AUTHOR(S) S. Guha and J. Yang				5d. PROJECT NUMBER NREL/SR-520-43191		
				5e. TASK NUMBER PVB74101		
				5f. WORK UNIT NUMBER		
7. PERFORMING ORGANIZATION NAME(S) AND ADDRESS(ES) United Solar Ovonic, LLC Troy, Michigan				8. PERFORMING ORGANIZATION REPORT NUMBER ZXL-6-44205-14		
9. SPONSORING/MONITORING AGENCY NAME(S) AND ADDRESS(ES) National Renewable Energy Laboratory 1617 Cole Blvd. Golden, CO 80401-3393				10. SPONSOR/MONITOR'S ACRONYM(S) NREL		
				11. SPONSORING/MONITORING AGENCY REPORT NUMBER NREL/SR-520-43191		
12. DISTRIBUTION AVAILABILITY STATEMENT National Technical Information Service U.S. Department of Commerce 5285 Port Royal Road Springfield, VA 22161						
13. SUPPLEMENTARY NOTES NREL Technical Monitor: Bolko von Roedern						
14. ABSTRACT (Maximum 200 Words) United Solar Ovonic LLC successfully used its spectrum-splitting a-Si:H/a-SiGe:H/a-SiGe:H triple-junction structure in their manufacturing plants, achieving manufacturing capacity of 118 MW in 2007 from its Auburn Hills and Greenville, Michigan plants. United Solar has a very aggressive expansion plan to achieve grid parity by improving its solar panel efficiency, improving manufacturing throughput, and reducing manufacturing cost. In the Thin Film Partnership Program, Uni-Solar identified three areas of research: i) Optimize a-Si:H and a-SiGe:H deposition parameters under the current manufacturing constraints for improving solar module efficiency and manufacturing throughput, and reducing the manufacturing cost; ii) Explore new deposition methods for a-Si:H and a-SiGe:H materials to improve a-Si:H/a-SiGe:H/a-SiGe:H triple-junction cell efficiency at high deposition rates; and iii) Explore new materials and new cell structures for higher efficiency at high deposition rates.						
15. SUBJECT TERMS PV; manufacturer; spectrum splitting; grid parity; module efficiency; triple junction; solar cells; devices; mixed-phase silicon; back reflector; deposition rate; large-area; amorphous silicon						
16. SECURITY CLASSIFICATION OF:			17. LIMITATION OF ABSTRACT UL	18. NUMBER OF PAGES	19a. NAME OF RESPONSIBLE PERSON	
a. REPORT Unclassified	b. ABSTRACT Unclassified	c. THIS PAGE Unclassified			19b. TELEPHONE NUMBER (Include area code)	

Standard Form 298 (Rev. 8/98)
Prescribed by ANSI Std. Z39.18